Imperial College London

Fundamental Study of Central Crack Mechanism and Criterion in Cross Wedge Rolling

By

Xianyan Zhou

Department of Mechanical Engineering

Imperial College London

South Kensington Campus, London SW7 2AZ, United Kingdom

This thesis is submitted for the degree of Doctor of Philosophy of Imperial College London and the Diploma of Imperial College London

2021

ABSTRACT

Cross wedge rolling (CWR), a novel metal forming process for manufacturing axisymmetric stepped shafts, is widely applied in transport industries. Central crack, the cavity formed in the product centre, is a critical problem, preventing its development in safety-critical industries. However, the understanding of the central crack mechanism is insufficient, and there is not yet a robust fracture criterion to predict its occurrence. This study aims to establish a fundamental understanding of the central crack mechanism and build a robust physically-based fracture criterion.

An innovative CWR physical model with plasticine billets was built in house, which allowed the dies to be rapidly 3D printed and the workpiece with specific mechanical properties to be efficiently manufactured. The effects of the stress variables and initial material properties (ductility) on central cracking were investigated by varying the die geometries and billet material compositions, respectively. It is found that the maximum shear stress plays a dominant role in the central crack formation, and with the increase of the material ductility, the central crack transitions from brittle fracture to ductile fracture.

A robust physically-based damage model set was proposed, along with a novel material constant calibration method. The reliability of the proposed model was validated quantitively by 60 groups of CWR tests with different materials and die geometries. The proposed calibration method will significantly benefit the industry due to the extremely simplified die geometries.

To further understand the central crack mechanism in the practical industry, the microstructural characteristics (e.g., inclusion, grain size and phase

composition) of two high-strength steel CWR billets (with/without high possibility to crack) were quantitatively analysed and compared. It is found that central cracking can be effectively avoided by controlling the inclusion content in the CWR billets.

DECLARATION OF ORIGINALITY

The work hereby presented is based on research carried out by the author Xianyan Zhou at the Department of Mechanical Engineering of Imperial College London, and it is all the author's own work except where otherwise acknowledged. No part of the present work has been submitted elsewhere for another degree or qualification.

COPYRIGHT DECLARATION

TABLE OF CONTENTS

VII

List of figures

XIII

XV

XIX

List of Tables

Acknowledgements

I would like to give my sincerest gratitude to my supervisors, Dr Jun Jiang and Prof Jianguo Lin, for their support, guidance and help through my PhD project. The most significant appreciation must be presented to Dr Jun Jiang, an excellent supervisor and a good mentor, motivating me with his agile mind and great patience, recognising my strength, providing opportunities to realise my ideas and learn from my mistakes. A huge thank you goes to Prof Jianguo Lin, who offered me the precious opportunity to study in the world-leading university with the top researchers in the metal forming area, and his continuous help and advice on my research. Both influenced my personal characters significantly, such as being confident but humble. Their profound instillation will be memorised for good.

Another huge thank you goes to my research group, the Intelligent metal forming group. It is a dynamic and energetic group filled with enthusiasm, inspiring ideas, endless support and complete trust. It was my most significant honour to be part of it. The group members are always willing to offer immediate and practical help whenever needed. Great gratitude is given to the research associates - Dr Catalin Pruncu who gave me incredible confidence and encouragement; Dr Zhutao Shao who supported me immeasurably; and Dr Jinghua Zheng who showed me how to be a successful woman scientist. The PhD students Qinmeng Luan, Kai Zhang, Yaping Wang, Ruiqiang Zhang, Zinong Tan, Yuehan Liu, Tabassam Yasmeen, and Dr Christopher Hopper also deserve my sincerest gratitude for their meticulous support, assistance and accompany on a daily basis. Without this wonderful group led by Dr Jun Jiang, my PhD journey could not have been as easy and delightful as it was.

Outside the research group, I would like to thank all the others who offered invaluable help on my research and made my PhD study such a fantastic journey. Special thanks go to Dr Fengzhen Sun and Dr Wenbin Zhou, being a senior researcher and giving me uncountable valuable comments and advice and Famin Tian, Lei Zhu and Xinyang Tan, and Shuai Jiang, being good research peers and loyal friends who are always around offering their extraordinary generosity and kindness. Then, I would like to thank the technicians, Ruth, Suresh and Alex. Without their immediate help and patient encouragement, my experiments could not be as successful as it was. I also would like to thank the graduate Dr Ran Pan, Dr Yong Li, Dr Yiran Hu, Dr Qi Rong, Dr Haoxiang Gao, Dr Xiaochuan Liu, Dr Zhaoheng Cai and Dr Xiaochuan Liu for their excellent suggestions and practical help on my research journey.

Special gratitude should be presented to my office colleagues, Emily, Joel, Macro, Geena, Alex Sancho, Alex Holland, Fabian, Tobias, Richard, James, Sherry, Sammy, Michael, and Joseph, who made my PhD journey splendid and colourful. During lunchtime or over the afternoon tea, we communicated deeply about the cultural difference in people, food, policy, etc. The daily cultural exchange greatly expanded my international horizons. I will memorise the precious shared moments forever.

My flat mates and my colleagues, Xiao and Yaping, deserve my appreciation by offering me a very friendly living environment for the past three years and constructing a real family, especially during the Covid-19 lockdown period. We support and accompany each other in a happy and healthy lifestyle. I could not imagine what would have happened without them. The company and support of my best friends in China, Luyao and Jie, is also of vital importance for the success of my PhD study.

Last but not least, the biggest thank you undoubtedly goes to my family, who always support my decisions unlimitedly and encourage me to chase my dreams. A special thank you is given to my two sisters for accompanying and taking care of my parents and grandma in my absence. It allowed me to concentrate on my study. Thank you for your support, understanding and blessings.

List of Publications

[1] **X. Zhou**, Z. Shao, C. Zhang, F. Sun, W. Zhou, H. Lin, J. Jiang and L. Wang, "The study of central cracking mechanism and criterion in cross wedge rolling," *Int. J. Mach. Tools Manuf.*, 2020.

[2] **X. Zhou**, Z. Shao, C. Pruncu, L. Hua, D. Ballint, J. Lin and J. Jiang, "A study on central crack formation in cross wedge rolling," *J. Mater. Process. Technol.*, 2020.

[3] **X. Zhou**, Z. Shao, F. Tian, C. Hopper, and J. Jiang, "Microstructural effects on central crack formation in hot cross-wedge-rolled high-strength steel parts," *J. Mater. Sci.*, 2020.

[4] **X. Zhou**, J. Jiang, and J. Lin, "A Comparative Study on Damage Models of Central Cracks in Cross Wedge Rolling," in *13th International Conference on Numerical Methods in Industrial Forming Processes*, 2019.

[5] **X. Zhou** and J. Jiang, "Fracture mechanisms and criterion of central cracking in cross wedge rolling for industry application," 2021. (Under review)

Acronyms and Abbreviations

CWR	Cross Wedge Rolling
FE	Finite Element
SEM	Scanning electron microscope
EBSD	Electron backscatter diffraction
EDX	Energy-dispersive X-ray spectroscopy
EDM	Electrical Discharge Machining
C&L	Cockcroft-Latham
R&T	Rice and Tracey
X&W	Xue and Wierzbicki

Notation

Symbols	Meanings
α	Forming angle, °
β	Stretching angle, °
η	Area reduction ratio
Δh	Wedge height, mm
d_0	Initial diameter of the workpiece, mm
d_f	Final diameter of the rolled product, mm
γ	Feed angle, °
D	Damage value
D_c	Critical damage value
$\bar{\varepsilon}_p$	Equivalent plastic strain
σ_1, σ_2 and σ_3	The first, second and third principal stress, MPa
$\bar{\sigma}$	Von Mises stress, MPa
σ_m	Mean stress or hydrostatic stress, MPa
T	Temperature, °C
$\dot{\varepsilon}$	Strain rate,/s
η_t	Stress triaxiality
Φ_P	Damage coefficient
σ_f	Fracture strength, MPa
σ_y	Yield strength, MPa
E	Young's modulus, MPa
μ	Friction coefficient
σ_n	Normal stress, MPa
k	Shear strength, MPa

m	Friction factor
a_1, a_2, a_3, a_4	Material constants
b_1, b_2, b_3, b_4	Material constants
$\bar{\theta}$	Normalised lode angle, °
ξ	Normalised third stress invariant
c_1, c_2, c_3	Material constants
d_1, d_2, d_3, d_1	Material constants
n, M	Working hardening related material constants
$\dot{\bar{\varepsilon}}$	Effective deformation rate, /s
$\dot{\varepsilon}_{ij}$	Strain rate tensor
σ'_{ij}	Stress deviator
A, B, C	Material constants
D_n	Normalised damage value
τ_m, τ_{max}	The maximum shear stress, MPa
$\sigma_{f,t}$	Ultimate strength under uniaxial tensile test, MPa
$\sigma_{f,c}$	Ultimate strength under uniaxial compressive test, MPa
τ_f	Shear strength, MPa
D_{nn}	Normalised damage model, MPa
$D_{c,nn}$	Normalised critical damage model, MPa
L_f	Final length of the workpiece, mm
D_{min}	The minimum diameter of the rolled sample, mm
D_{max}	The maximum diameter of the rolled sample, mm
v_R	Radial velocity, m/s
v_H	Hoop velocity, m/s
σ_R	Radial stress, MPa
σ_H	Hoop stress, MPa
τ_{RH}	Shear stress, MPa

Chapter 1 Introduction

1.1 Research motivation

Cross wedge rolling (CWR) is an innovative metal forming process to manufacture axisymmetric stepped shafts, whereby a cylindrical billet is plastically deformed under two wedged rollers moving tangentially to each other [1–3]. One CWR machine is presented in Figure 1.1, consisting of two rollers with wedges rotating in the same direction. The unique linear incremental deformation characteristics make the CWR advantageous over die forging or machining in many aspects such as high productivity, high material utilisation and low energy consumption [1, 2, 4]. This technique is mostly used in manufacturing steel rotary parts such as the camshafts and connecting rods in the automotive industry [5–7]. It has been promoted to much broader applications such as aerospace, high-speed rail trains and nuclear industries [8–12]. It was reported in 2018 that nearly 300 rolling production lines had been promoted by the University of Science and Technology Beijing in China, and the annual production of various parts reached approximately 2 billion pieces with a gross weight of 400, 000 tons [2]. A wide range of CWR products is shown in Figure 1.2. Meanwhile, the global market for axisymmetric stepped shafts is expanding quickly with rising social demands. For example, the automotive axle market size was estimated to reach USD 64.8 billion by 2027 [13].

Figure 1.1 Cross wedge rolling machine [2]**.**

Figure 1.2 Various cross wedge rolling products [2]**.**

Central cracking, also called the Mannesmann effect, refers to the formation of cavities in the centre of the workpiece along the axle, as shown in Figure 1.3. It is considered the most serious issue in CWR as it considerably deteriorates the product quality and even causes product failures. The limited

understanding of the central–cracking process seriously impedes the rapid development of CWR, especially in safety-critical industries such as the aerospace industry [3, 4]. A sound understanding of the fracture mechanism facilitates to build a robust physically-based fracture criterion, enabling to predict the central cracking occurrence and produce crack-free products without conducting a large number of experimental trials. However, over the last seven decades, the underlying fracture mechanisms are still unclear, and no robust fracture criterion has been adopted in industrial applications. The main difficulties include: (1) the complex mechanistic characteristics involving severe plastic deformation, triaxial stress state, severe shear stress and cyclic loadings, making it challenging to distinguish the critical mechanistic factor; (2) the experimental limitations, *i.e.* a large number of CWR dies are required to clarify the critical mechanistic factor and fracture criterion validation, which is experimentally unrealistic due to limited project duration and budgets; and (3) the complex microstructural evolution during hot CWR, including phase transformation, recrystallisation, grain growth, etc. Therefore, it is crucial to propose novel and practical methods to tackle these difficulties in investigating the fracture mechanism and developing a robust fracture criterion.
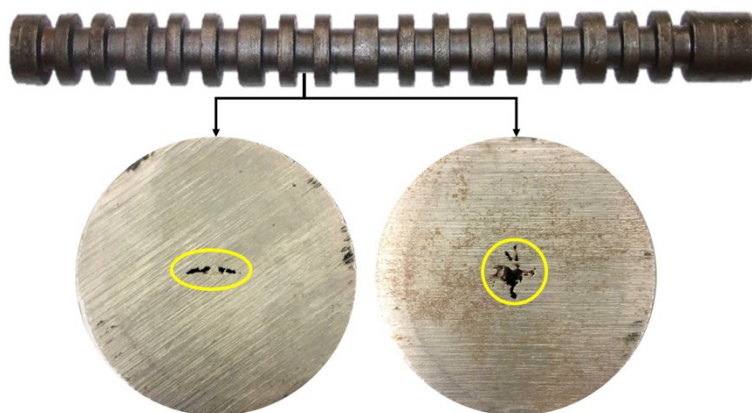
Figure 1.3 Central cracks observed in a cross wedge rolled automotive camshaft.

1.2 Fundamentals of cross wedge rolling

1.2.1 Development of cross wedge rolling

The first patent for the CWR machine was filed by Lebek in Germany in 1879, and it was not until 1949, that its first industrialisation was carried out by forming connecting rods in Russia [1, 3]. Until now, the CWR has been developed for over 12 decades. Great technological and scientific development has been made across the world. For example, hollow parts such as engine valves or railway axles can be manufactured efficiently using CWR [14, 15]. CWR of threaded shafts and shafts with non-circular cross-section is also subject to intensive investigation [16, 17]. Multi-materials such as steel and aluminium are used in producing tailored products [18, 19]. The CWR and hot forging hybrid technique was applied to manufacture aircraft turbine blades [12, 20]. The CWR development before 1993 was reviewed in detail by Fu and Dean [1]. More recent knowledge about the theoretical, experimental and technical development of CWR was reviewed by Pater [21] and Tofil et al. [22].

1.2.2 Operational principles of cross wedge rolling

In the CWR process, a cylindrical billet is plastically deformed into a stepped shaft under the action of tools with wedges. One typical CWR configuration is presented in Figure 1.4. The dies, distributed axisymmetrically around the billet, move tangentially to the billet. The billet, located between the dies, is self-rotated, driven by the dies and deformed to the designed geometry according to the wedge profiles. Two guide plates are used to constrain the horizontal transition of the billets during the rolling.

In industrial practice, the billet is pre-heated to elevated temperatures before the CWR to achieve high workability. For example, the pre-heat treatment

temperature for steel billets ranges from 950 to 1150 °C [23]. The CWR dies are also warmed up to 150 to 250 °C to avoid the sharp decrease of the workpiece during CWR [3].
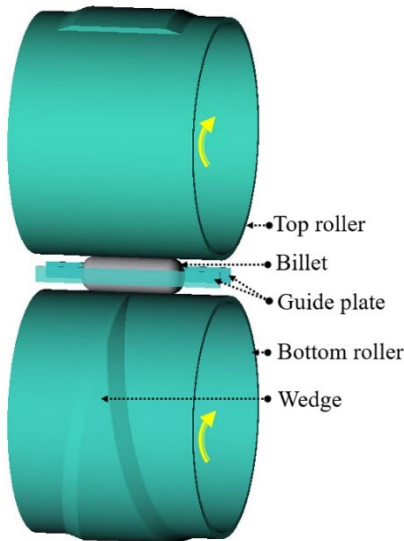
Figure 1.4 Typical cross wedge rolling configuration.

The detailed deformation process is illustrated in Figure 1.5. The wedge on the tool is generally divided into four zones, knifing zone, guiding zone, stretching zone and sizing zone. During the knifing zone, the billet is bitten in between the two dies with slight axial deformation but large radial compression of approximately Δh (wedge height) until the required billet diameter $d_0 - 2\Delta h$ is achieved. The guiding zone is to guarantee radial compression along the whole billet circumference. In the stretching zone, the billet is subject to a strong axial extension. The material contacting with the wedge side is pushed toward the billet ends along the spiral trajectory. The sizing stage is to ensure the geometric accuracy of the final product. In Figure 1.5, three geometrical parameters are defined to describe the die geometry, forming angle α, stretching angle β, and area reduction ratio η. The area reduction ratio represents the relationship between the initial and final diameter of the workpiece d_0 and d_f. Via controlling the die geometry, the

5

material flow and the stress/strain states within the workpiece vary accordingly, enabling the production of high-quality products with high geometric accuracy, high mechanical property and without internal defects.
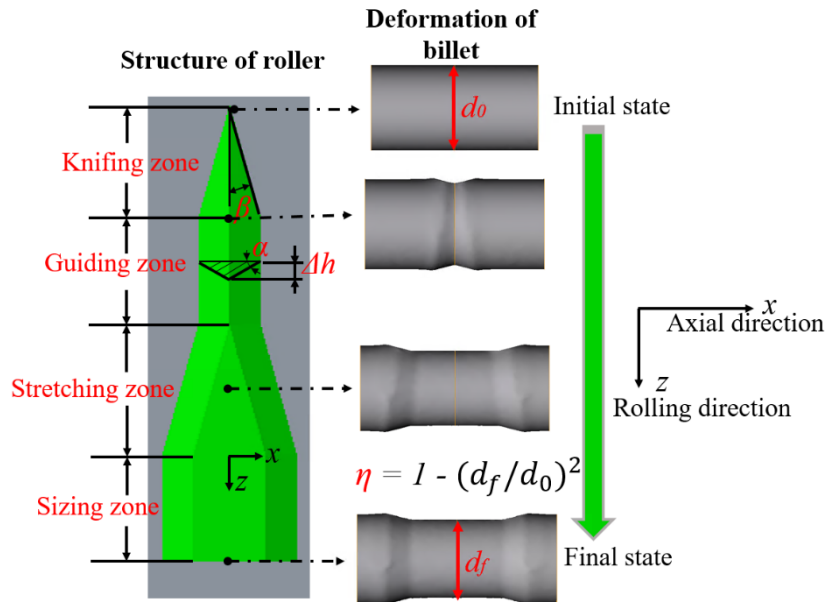
Figure 1.5 Configuration of the cross wedge rolling tool and the corresponding billet deformation in four stages.

1.2.3 Advantages of cross wedge rolling

The CWR is advantageous to other conventional manufacturing methods such as die forging or machining in many aspects. For example, the continuous deformation feature generates high productivity, which can be 5 - 20 times higher than that for machined parts and 3 - 10 times higher than for hot forged parts [1, 2, 4]. The force on the tool is relatively low due to the linear incremental deformation characteristic, resulting in the long die operational life, low energy consumption and low noise pollution. In addition, the detailed design on the wedge profiles guarantees the geometric accuracy [1] as well as the high material utilisation, which can reach as high as 85% [2, 24]. Meanwhile, due to the severe plastic deformation, the grains within

the workpiece are considerably refined, especially on the surface where the grain size could be as small as 43% of the initial grain size [8]. Hence, the advantages of the CWR process are summarised as follow:

- High productivity due to continuous rolling

- High material utilisation compared with the corresponding forging or machining due to the net-shaping forming feature

- High mechanical property, such as high strength and high ductility, caused by the grain refinement

- High geometric accuracy due to the well-designed die and the continuous deformation

- Low energy consumption, long tool life and low environmental impact because of the low forming force

1.2.4 Limitations of cross wedge rolling

There are also some drawbacks limiting the rapid development of CWR, such as the occurrence of defects on the CWR products. These defects are generally categorised into three types: (1) surface defects, (2) irregular workpiece cross-section, and (3) internal defects [1, 4]. The first two types of defects have been well understood through practical trials and fundamental research. For example, the surface defects, spiral grooves, can be prevented by adjusting the contact conditions between the die and the workpiece [4, 25]. However, **central crack**, also called internal defects, as one of the most serious defects in CWR, has been studied for seven decades without drawing an agreement. The formation of central cracks deteriorates product quality and ultimately leads to product failures. Currently, the CWR engineers solve this problem by the trial-and-error approach through adjusting the die geometry or the temperature, which is cost and time-consuming. This greatly limits the CWR capability of producing complex-shaped and high-quality

products. With a sound understanding of the underlying fracture mechanism and a robust damage model, the optimised parameters can be achieved through finite element (FE) modelling without any practical trials.

Therefore, it is vital to identify the underlying fracture mechanism and establish a proper damage prediction model for producing high-quality products.

1.3 Aim and objectives

This work aims to clarify the underlying fracture mechanisms of the central crack formation in CWR on multiple scales and propose a robust fracture criterion to predict the central crack formation. The achieved understandings enable crack-free products to be made by controlling the process parameters (e.g. die geometry, temperature and rolling speed) and initial billet microstructure without conducting a large number of experimental trials. To achieve this, the following objectives have been completed:

- **Review** the development of central crack mechanism and criterion and the related research methodologies. Identify the difficulties and limitations in previous studies.
- Establish reliable **CWR FE models** embedded with damage models via self-defined subroutines. Investigate the stress/strain/damage characteristics of the workpiece during the CWR.
- Propose a new **fracture criterion** based on the understanding of the mechanistic characteristics and validate it by the collected experimental data from the literature.
- Build a **lab-scale CWR physical model** for investigating the fracture mechanisms, enabling the CWR dies with various geometries to be manufactured efficiently and the billets with specific material

properties to be achieved quickly. Investigate the **critical mechanistic factor** by varying the die geometries. Explore the **multiple fracture mechanisms** by varying the material properties of CWR billets.

- Improve the proposed fracture criterion based on multiple fracture mechanisms. **Validate the enhanced fracture criterion** with multiple materials and various die geometries.

- Further explore the **central crack mechanisms on a microscopic scale** with a practical industrial case.

1.4 Thesis outline

The whole thesis contains eight chapters. The research topic, objectives and aims are presented here. A comprehensive literature review is presented in Chapter 2, including the progress of the central crack mechanism and criterion and the related research methods. The practical difficulties in revealing the central crack mechanism and developing reliable fracture criterion are clarified, for instance, to distinguish the key mechanistic factor from a wide range of potential factors. The related research methods are reviewed, including analytical study, FE modelling and CWR tests.

Chapter 3 delivers the methodology in this study, involving the CWR physical model, the mechanical and microstructural experiments and FE modelling. The physical model with model material enables the complex industrial CWR process to be experimentally simulated in the lab environment, which significantly reduces the experimental difficulties. The 3D printed dies generate specific stress states at a low cost and in a short time. The corresponding FE models present the stress/strain and damage distribution and evolution during the CWR. The underlying micro fracture mechanism can

be revealed by quantifying the inclusions, grain size, phase compositions using advanced microstructural characterisation.

In Chapter 4, the central crack mechanism and criterion are proposed by considering its unique mechanistic characteristics, i.e., strong tensile and shear stresses. The 27 groups of CWR tests quantitatively validate the proposed fracture criterion's high robustness using pure aluminium under various die geometries.

Chapter 5 focuses on further validating the central crack mechanism and criterion proposed in Chapter 4 by the in-house developed CWR simulation testing rig. The individual role of a wide range of potential critical mechanistic factors is clarified through varying the die geometries to get specific stress states. The dominant role of the maximum shear stress is determined. In addition, a new method is proposed to determine the associated material constants in the fracture criterion, which presents high accuracy and cost/time efficiency.

In Chapter 6, the fundamental understanding of the central crack mechanism and criterion achieved in Chapter 5 is introduced to industrial applications. With the consideration of the multiple fracture mechanisms, a new damage model set is proposed, which is appliable for both the low and high ductility materials. The high accuracy of the damage model set has been checked by 60 groups of CWR tests with various materials, including pure aluminium, plasticine at different ductility levels and C45 steels. This finding will impact the CWR industry significantly by effectively solving the long-standing central cracking issues.

The microstructural effects of the high-strength steel CWR billets on central cracking are revealed in Chapter 7. The microstructural factors (including the chemical and phase compositions, grain size and inclusions) in two billets

(one expected to form crack and the other crack-free) are carefully quantified and compared under the CWR conditions. The critical microstructural factor to form central cracking is clarified. The finding will help effectively prevent central crack formation by controlling the initial billet microstructure.

Chapter 8 summarises the main achievements made in this study and suggests the future work to adopt for a developed understanding of the central crack mechanism and criterion.

Chapter 2 Literature review

This chapter focuses on the understanding of the previous work on central crack mechanism and criterion. The main difficulties that limit the sufficient understanding of central cracking are clarified. The involved research methods used in the literature are summarised in Section 2.3.

2.1 Central crack mechanism

The central cracks form in the central region of the CWR workpiece along the axial direction due to the external forces applied by the dies. The interaction between the dies and the workpiece causes complex stress/strain states within the workpiece and damages the material when the stress/strain/energy reaches a critical value. The factors related to the central cracking include the die and workpiece geometries, temperature, rolling speed and the mechanical/microstructural properties of the billets, etc. Intensive studies have been conducted on how the process parameters affect central cracking and which are the critical mechanistic or microstructural factors for central cracking.

2.1.1 Effects of process parameters

The die geometry (including the forming angle, stretching angle and area reduction ratio) is acknowledged as the most critical process parameter for central cracking due to its significance in affecting the material flow and stress/strain distribution. However, achieving crack-free products by controlling the die geometry has been a myth for over seven decades. Some work found that the central cracking could be mitigated by reducing the forming angle or the stretching angle [3, 26], while some other investigations suggested that the large forming angle was beneficial for crack-free products

13

[27]. Similarly, there is an inconsistency on the influential trends of the area reduction ratio on the central cracking [26–28]. This is because the effects of the die geometry on the stress/strain response of the workpiece are nonlinear due to its complexity, and how the stress/strain affects the material failure in a CWR condition is still unknown. Thus, there is no unified monotonous influential trend of the effects of geometrical parameters on central crack formation.

Besides the die geometries, the temperature and rolling speed have also been investigated. By comparing the effective stress and strain in copper and steel at variable temperatures (23.85, 223.85 and 423.85 °C) and strain rates (1, 100, 10,000/s, calculated based on rolling rates), Li [4] found that the lower temperature facilitated central cracking, while the strain rate effect was not significant. By experimentally analysing the central cracking in hot steel (1050 ~ 1250 °C) at diffident rolling speeds (150 ~ 500 mm/s), however, Meyer et al. [29] found a lower temperature or low rolling speed could accelerate internal cracking. Recently, by analysing the damage in steels, Pater et al. [23] found that the effect of temperature is not as significant as the forming angle and stretching angle. The inconsistency is related to the lack of a unified fracture criterion to determine central cracking. For example, the effective stress/strain was applied by Li [4] to study the effect of temperature and rolling speed on central cracking, while a newly proposed strain-based damage model considering the central crack mechanisms was adopted by Pater et al. [23]. Thus, it is necessary to build a reliable consistent criterion to determine the occurrence of central cracking.

Apart from the process-related factors, the material properties also exhibit effects on central crack behaviours. It was observed that the central crack is always larger in pure aluminium than that in copper [4]. It was also noticed in the industry that the billets from different batches experienced different

central crack behaviours [30]. On a microscopic scale, the inclusions were observed in the cracked CWR products [27, 31]; however, no systematic research to clarify the effects of inclusions and exclude other potential factors such as chemical compositions, phase transformation and grain size.

2.1.2 Mechanistic study

Due to the complex loading conditions in CWR, including triaxle stress states, severe plastic deformation, cyclic loadings and severe shear effects, a wide range of mechanistic factors have been suspected to be critical for the central cracking formation, such as the tensile stress, the shear stress, the axial tensile stress, the secondary tensile stress (the tensile stress component on the minimum cross section), and the cyclic tensile and compressive loadings.

One early study of the central cracking in CWR was made by Smirnov [32] in 1947, which attributed the reason for central crack formation to shear stress and the secondary tensile stress generated by the normal compression between the rolling tools. Tselikov et al. (1961) [33] thought the accumulated tensile stress was the main reason, which increased with the workpiece's revolution. This opinion was supported by Sucharev and Uchakov [34] and Poluchin et al. [35]. Smirnov and Lunvev [36, 37] suggested the secondary tensile stress generated by the normal compression was the main reason by analysing the stress state in rotary compression. Higashino et al. [38] attributed it to the alternative tensile and compressive stresses after analysing the velocity and strain distributions on the cross-section in the workpiece. The low cycle fatigue in the central region was reported by Menson in 1974 [39]. Based on the viscous crack theory developed by Kolmogorov [40, 41], Makushok and Shukin [42] and Shukin [43–45] established a stress-based mathematical model to describe the mechanism of central crack formation. It demonstrated that the microfracture in the central region occurred when the deformation reached the material limit of

the critical shear intensity, followed by the microfracture accumulation under successive load cycles, and finally developed into central cracks. In 1976, according to the experimental investigation, Guzavichus et al. [46] found a strong velocity gradient between the flanges and the workpiece steps, which led to strong torsion. The increase of the rotation number increased the torsion, causing strong shear stress. When the shear stress exceeded the critical value of the workpiece, fracture occurred.

Teterin and Liuzin [47] considered the presence of an intensive plastic deformation zone in the centre of the workpiece facilitated central crack formation in cross rolling, and voids would be opened when the plastic strain exceeded the critical cohesive value. Lee et al. [48] supported this view by comparing the plastic strain history in the central region with the cracking evolution and identifying the maximum plastic strain as a determining factor with the comparison of the other four damage models. Li et al. [26] made the same conclusion by comparing the maximum equivalent plastic strains under two die geometries with three materials.

Recently, it is acknowledged that the combined shear and normal stress leads to central crack formation. In 2002, Li et al. [31, 49] illustrated that the tensile stress opened the initial microvoids/cracks around the inclusions, and the shear stress promoted the aggregation and deformation of voids by experimentally observing the crack morphology in the pure aluminium workpiece. Yang et al. [27] observed the intensive tensile and shear deformation in the central region of the C45 steel samples by FE modelling. Pater et al. [7] revealed that the central crack in CWR is a mix-mode fracture (void formation and shear fracture) by analysing the stress invariants in the central region of the C45 steel workpiece via FEM [50].

In summary, the mechanistic factors for central crack formation can be categorised into the following three groups:

- **Stress-based factors:** normal stress (the axial tensile stress, secondary tensile stress and the first principal stress); shear stress (on the transverse cross-section); the combined effects of shear and normal stress;

- **Strain-based factors**: equivalent plastic strain;

- **Low cyclic fatigue**: cyclic loadings on the transverse cross-section.

A wide range of potential mechanistic factors has been proposed and investigated in previous studies. However, no comprehensive or comparative work has been conducted to clarify the dominant factor for central crack formation. The main difficulty lies in requiring a high number of CWR tests with various-shaped dies, which enable specific stress states to be created. The cost of CWR dies is extremely high, and the lead time is long. Replicate the industrial CWR process in the lab in the project is not feasible, considering the limited project duration and reasonable budgets. Thus, it is necessary to explore novel methods to address these experimental difficulties.

2.1.3 Microstructural study

It was reported that the batch difference of CWR billets caused different central cracking behaviours under the same CWR process parameters, including the same die geometry, temperature and rolling rate [30]. The reason was suspected to the billet microstructure, which could be different in each batch. A wide range of microstructural factors could affect material fracture such as grain size and phase/chemical compositions. However, limited study has been conducted on the microstructural factors relating to central crack formation. Recently, with the scanning electron microscopy (SEM) and energy-dispersive X-ray spectroscopy (EDX) techniques, the

17

inclusions were observed in various metals for CWR, such as pure aluminium [31], C45 steel [27] and 25CrMo4 steel [8]. It is considered that the inclusions provided the nucleated sites for void formation and accelerated the propagation due to the strong stress concentration around the inclusions [27]. Nevertheless, no quantitative research has been conducted to clarify the critical effects of inclusions in CWR, nor any research to exclude the other potential factors. Thus, it is necessary to conduct a systematic investigation to determine the dominant role of the inclusions.

2.1.4 Summary

Intensive research has been conducted on exploring the central crack mechanism, but there is yet no agreement on what is the critical mechanistic or microstructural factor in central cracking. The main reasons include (1) the experimental limitations in manufacturing many CWR dies with limited project duration and budget and (2) the insufficient attention to the microstructural effects. In this study, a novel experimental method has been proposed to address the die manufacturing problem, and the microstructural factors have been quantitively analysed and compared using advanced microstructural characterisation techniques, including SEM, EDX, and electron backscatter diffraction (EBSD).

2.2 Fracture criteria/damage models

2.2.1 Fracture criteria/damage models for central crack formation

A robust damage model or fracture criterion is essential for manufacturing products with high geometric accuracy and high mechanical performance without taking numerous experimental trials. With the robust damage model or fracture criterion, the forming window with potential product failures can be

effectively avoided by FE modelling. Many damage models or fracture criteria have been investigated for central cracking prediction.

The central crack prediction began with the work conducted by Makushok and Shchukin [42] and Krasnievskin et al. [51] around 1980. Based on Kolmogorov's fracture criterion [52], a central crack predictive model was proposed, assuming that the material fails when the shear strain reaches a critical value. The critical value is associated with the cyclic effects. The lower strain amplitude per deformation cycle results in a higher accumulated fracture strain. After conducting over 50 groups of CWR tests on pure aluminium AA1100, Li et al. [53] built a non-dimensional fracture criterion. However, this criterion is limited to specific geometries and materials. Later on, by numerically analysing the mean stress, the first principal stress and effective plastic strain evolution under two different die, Li et al. [49] concluded that the effective plastic strain was the best to describe the central crack formation.

The rapid development of continuum damage mechanics brings in a wide range of damage models in the form presented in Equation 2.1, which integrates the dominant effect of the equivalent plastic strain and the assistant effect of the stress variables in degrading materials. In this formula, D represents the damage value and $\overline{\varepsilon_p}$ is the effective plastic strain. $f(\sigma)$ is a stress-related formula, describing the effects of stress variables on fracture as presented in Equation **2.2** - Equation **2.5**. In these equations, σ_1 represents the first principal stress, σ_m is the mean stress (also called hydrostatic stress), and $\bar{\sigma}$ is the von Mises stress. A_0 represents the material constant, which varies with materials. Fracture occurs when the damage value D exceeds the critical damage value D_c. The value of D_c is usually obtained experimentally. These models are extensively used in predicting the ductile fracture in metal forming.

$$D = \int_0^{\bar{\varepsilon}} f(\sigma) \, d\overline{\varepsilon_p}$$

Equation 2.1

Cockcroft-Latham
[28, 54, 55]

$$\boldsymbol{D} = \int_0^{\bar{\varepsilon}} \boldsymbol{\sigma_1} \, \mathbf{d}\overline{\boldsymbol{\varepsilon_p}}$$

Equation 2.2

Normalised
Cockcroft-Latham
[56–59]

$$\boldsymbol{D} = \int_0^{\bar{\varepsilon}} \boldsymbol{\sigma_1}/\overline{\boldsymbol{\sigma}} \, \mathbf{d}\overline{\boldsymbol{\varepsilon_p}}$$

Equation 2.3

Modified Oyane

model [60]

$$\boldsymbol{D} = \int_0^{\bar{\varepsilon}} \boldsymbol{g(T, \dot{\varepsilon})}\left(\boldsymbol{1} + {}^{\boldsymbol{\sigma_m}}/_{\boldsymbol{A_0\overline{\sigma}}}\right) \mathbf{d}\overline{\boldsymbol{\varepsilon_p}}$$

Equation 2.4

Stress triaxiality $\eta_t = \frac{\sigma_m}{\overline{\sigma}}$

Oyane model [61]

$$\boldsymbol{D} = \int_0^{\bar{\varepsilon}} \left(\boldsymbol{1} + {}^{\boldsymbol{\sigma_m}}/_{\boldsymbol{A_0\overline{\sigma}}}\right) \mathbf{d}\overline{\boldsymbol{\varepsilon_p}}$$

Equation 2.5

In 2005, Piedrahita et al. [28] applied the Cockcroft-Latham (C&L) damage model (in Equation 2.2) to determine the forming window for crack-free CWR products. With this damage model, the highest damage value was not always observed in the central region [3, 54, 55]. The main reason is that the C&L damage model, a phenomenological model, was proposed to predict the internal defects in the extrusion process based on experimental observations [62, 63]. In this model, the first principal stress was considered as the dominant factor for material fracture. However, in CWR, the driving force for central cracking is still uncertain. Oh et al. [64] modified the C&L damage model by introducing the von mises stress (in Equation 2.3) considering that stress ratio ($^{\sigma_1}/_{\overline{\sigma}}$) was more suitable to present the void growth than the first principal stress. The modified model, called the normalised C&L damage model, was widely applied in the prediction of central cracks in CWR [56–59]. Liu et al. [56] found that this model could accurately predict the fracture

location since the highest damage value was observed in the central region of the CWR workpiece. By comparing the central cracking in hot CWR (1050 °C) and warm CWR (650 °C), Huang et al. [58] numerically predicted that central crack was more likely to form at the warm condition; however, the experiments showed an opposite trend. The inconsistency implies that more research is required to understand the dominant mechanistic factor to central cracking.

Novella et al. [60] modified the classical Oyane model (in Equation 2.5) by introducing the effects of strain rate $\dot{\varepsilon}$ and temperature T as shown in Equation 2.4. The simulated results show the crack occurred in the central region along the axial direction. The classical Oyane model, a micromechanics-based model, was proposed to predict the fracture strain in pore-free materials with the consideration of void growth [61]. However, strong shear effects occur in CWR, implying this model's accuracy needs to be further examined.

In 2019, Pater et al.[65] compared nine classical damage models (in Equation 2.2 - Equation 2.3 and Equation 2.5 - Equation 2.11) in predicting the central cracking in C45 steels, but none of them showed a high accuracy level. This is because the physical meanings are insufficiently considered in these damage models. Most of these damage models are phenomenological models derived from experimental observations with limited applications. For example, the C&L damage model was experimentally proved to be applicable only in low or negative triaxiality states [66]. Although the micro-mechanism-based models, R&T model and Oyane model, account for void growth, mathematically presented by the stress triaxiality, it showed that the triaxiality dependent fracture is limited in predicting shear dominated fracture [67], while the shear fracture is the main fracture type in CWR as proved by Pater et al. [7].

In 2020, Pater et al. [7] proposed an innovative hybrid damage model (in Equation 2.12) based on the maximum shear stress criterion and the normalised C&L damage model in Equation 2.3. The underlying fracture mechanisms, void formation and shear fracture, were revealed based on the value of the stress triaxiality. It is defined when the stress triaxiality is negative, the shear fracture is the dominant fracture mechanism; when it is higher than 0.33, the void formation is dominant; otherwise, two fracture mechanisms coexist. The accuracy of this model was validated by 6 groups of CWR tests with hot steels at various temperatures and die geometries by comparing the cracking lengths. However, as mentioned before, the C&L damage model has been experimentally validated to be only accurate in the low or negative stress states [7, 66]. Therefore, the robustness of this damage model set is required to be re-examined.

Freudenthal [68]
$$D = \int_0^{\bar{\varepsilon}} \bar{\sigma} \, d\bar{\varepsilon_p}$$
Equation 2.6

Rice and Tracey [69]
$$D = \int_0^{\bar{\varepsilon}} exp(\frac{3\sigma_m}{2\bar{\sigma}}) \, d\bar{\varepsilon_p}$$
Equation 2.7

Brozzo et al. [70]
$$D = \int_0^{\bar{\varepsilon}} \frac{2\sigma_1}{3(\bar{\sigma} - \sigma_m)} \, d\bar{\varepsilon_p}$$
Equation 2.8

Argon et al. [71]
$$D = \int_0^{\bar{\varepsilon}} (\bar{\sigma} + \sigma_m) \, d\bar{\varepsilon_p}$$
Equation 2.9

Ayada et al. [72]
$$D = \int_0^{\bar{\varepsilon}} \frac{\sigma_m}{\bar{\sigma}} \, d\bar{\varepsilon_p}$$
Equation 2.10

Zhan et al. [73]
$$D = \int_0^{\bar{\varepsilon}} (\sigma_m - \bar{\sigma}) \, d\bar{\varepsilon_p}$$
Equation 2.11

Pater et al. [7]
$$D = \int_0^{\bar{\varepsilon}} [(1 - \Phi_P)\frac{\sqrt{3}}{2}\frac{\sigma_1 - \sigma_3}{\bar{\sigma}} + \Phi_P \frac{\sigma_1}{\bar{\sigma}}] \, d\bar{\varepsilon_p}$$
Equation 2.12

$$\Phi_P = \begin{cases} 0, & \eta_t \leq 0 \\ \sqrt{3\eta_t}, & 0 < \eta_t \leq 0.33 \\ 1 & \eta_t > 0.33 \end{cases}$$
Equation 2.13

2.2.2 Ductile damage models with shear effects

As mentioned above, some classical damage models take into account the void growth but not the severe shear effects. Great progress has been made in the field of damage models in predicting ductile fracture with shear effects. Zhu et al. [74] introduced a new term, shear ratio ($\frac{\tau_{max}}{\bar{\sigma}}$) into the R&T model to describe the damage caused by shear effects (in Equation 2.14). Smith et al. [75] modified the R&T model by involving the shear shrinking mechanism (in Equation 2.15), which expanded its application from the high triaxiality to the low or negative triaxiality states, appliable to predict the shear fracture. Meanwhile, new parameters, Lode angle parameters such as the normalised third stress invariant ξ and the Lode angle parameter $\bar{\theta}$ defined in Equation 2.16 are introduced to make up with the limitation of the triaxiality dependent model in predicting the shear fracture. Bai and Wierzbicki modified the classic Mohr-Coulomb criterion (MMC model) (Equation 2.16) by transferring the local stress states to a stress-strain mixed coordinate made by the equivalent plastic strain to fracture $\bar{\varepsilon}_f$, the stress triaxiality η_t and the Lode angle parameter $\bar{\theta}$, which shows a high accuracy in predicting shear dominant fracture [76]. Xue and Wierzbicki (X&W) modified the plastic strain criterion by accounting for the effects of triaxiality and the normalised third stress invariant ξ (Equation 2.17) [77, 78], enabling to cover the whole range of stress states. These models are highly likely to predict the central cracking accurately because they consider the shear effects; thus, examining their robustness in the CWR process quantitively is necessary.

Zhu [74]	$\int_0^{\bar{\varepsilon}_f} a_1 \exp\left(a_2 * \eta_t\right)\left(\frac{\sigma_1 - \sigma_3}{\bar{\sigma}}\right)^{\frac{a_3}{a_4 + \eta_t}} d\bar{\varepsilon} = D_c$ Material constants a_1, a_2, a_3 and a_4 = 1.37, -2.04, -9.47 and 1.57 respectively for AISI 1045 steel [74]	Equation 2.14

Smith [75]	$$\int_0^{\bar{\varepsilon}_f} b_1 \exp(b_2 * \eta_t) - b_3 \exp(-b_4 * \eta_t) \ d\bar{\varepsilon} = D_c$$ Material constants b_1, b_2, b_3 and b_4 = 2.4, -0.49, 1.5 and 0.08 respectively for AISI 1045 steel [74]	Equation 2.15

MMC model [76]	$$\int_0^{\bar{\varepsilon}_f} \frac{c_1}{c_2} \sqrt{\frac{1 + c_3{}^2}{3}} \cos\left(\frac{\pi\bar{\theta}}{6}\right) + c_3\left(\eta_t + \frac{1}{3} \sin\left(\frac{\pi\bar{\theta}}{6}\right)\right)^{-\frac{1}{n}} d\bar{\varepsilon} = D_c$$ The normalised third stress invariant $$\xi = \frac{27 J_3}{2\bar{\sigma}^3} = \frac{27(\sigma_1 - \sigma_m)(\sigma_2 - \sigma_m)(\sigma_3 - \sigma_m)}{2\bar{\sigma}^3}$$ The normalised Lode angle $$\bar{\theta} = 1 - \frac{2}{\pi} \arccos \xi$$ c_1 = 753 MPa, c_2 = 410 MPa, c_3= 0.137 and n = 0.13 for AISI 1045 steel [74, 79]	Equation 2.16

X&W model [66]	$$\int_0^{\bar{\varepsilon}_f} d_1 \exp(-d_2 * \eta_t) - [d_1 \exp(-d_2 * \eta_t)$$ $$- d_3 \exp(-d_4 * \eta_t)](1 - \xi^M)^M \ d\bar{\varepsilon} = D_c$$ d_1 = 0.49, d_2 = 0.001, d_3=0.76, d_4= 1.89, and M = 6 for AISI 1045 steel [74]	Equation 2.17

2.2.3 Summary

In summary, the damage models for central crack have been studied intensively, and evident progress has been made. Introducing the fracture mechanism has been attempted in the damage model, such as the shear effects were taken into account in the Pater's model in Equation 6.2. However, the understanding of the dominant fracture mechanism in central cracking is still unclear. Meanwhile, these models have never been quantitatively validated due to the lack of a large number of CWR dies.

2.3 Research methodologies in cross wedge rolling

Various research methods have been adopted and developed for CWR, including theoretical analysis, FE modelling and physical modelling.

2.3.1 Theoretical development

The first nomograms to calculate the contact surface between the die and workpiece during CWR were designed by Tichauer [80] and developed by Awano and Danno based on the experimental investigation [81]. Later on, a new formula with the consideration of the process parameters in CWR was proposed based on the surface integration method [82]. The contact pressure was calculated with the known contact area using the upper-bound method [83] and the energy method [84]. A new method called layer modelling was applied to analyse the rolling stability because the metal flow patterns on the workpiece cross-section are similar to that in rotary compression [21, 85–87]. Slip-line field theory [88] and viscous crack theory [40, 41] were applied to investigate the deformation and fracture mechanisms. These formulas guided designing the CWR process when the FEM was unavailable. However, these theoretical models were built under simplifications and assumptions due to the nonlinear and dynamic workpiece-tools contact behaviours. Their accuracy cannot be guaranteed, especially at high temperature. Currently, the theoretical derivation is gradually replaced by the advanced FE model.

2.3.2 Numerical simulation

At the beginning of the 21st century, the FE model's appearance significantly improved the understandings of central cracking. The mechanical and microstructural characteristics of the CWR workpiece can be presented in 3D models clearly and in detail.

A wide range of FE software programs has been applied to simulate the complex CWR process in literature, such as Deform 3D [89–92], ANSYS/LS-DYNA [93–95], Forge 3 [29, 60, 96], Simufact Forming [97–100], QForm [101].

25

A three-dimensional CWR FE model was established in ANSYS/LS-DYNA by Dong [93], through which the displacement, interfacial slip and stress on the pure aluminium workpiece were recorded, where the nonlinear deformation behaviours matched well with the experimental observation. This model was then applied to investigate central cracking under 14 rolling conditions. The first principal stress was considered critical by comparing its evolution with the central cracking behaviours [102]. Since then, the temperature characteristics in CWR were widely investigated by FEM [54, 103, 104].

Meanwhile, many damage models and fracture criterion were implemented into the FE model to predict central cracking [7, 54, 60]. The damage distribution on a cross wedge rolled part was predicted by the modified Oyane fracture criterion in the FE program FORGE 2011 [60]. The predicted fracture was located in the central region and along the axial direction, agreeing well with the experimental observation.

2.3.3 Experimental research

The experimental investigation is always essential in exploring the nature of the deformation and the fracture processes. A great deal of experimental research on CWR can be found in the literature.

In practice, the typical industrial CWR machine is large and mostly applied to produce steel products at high temperature. It is a big challenge to build an industry scaled CWR machine in a lab environment. For fundamental understanding, many simplified steps have been taken as follow:

- Building lab-scale prototypes to replace the industrial machine
- Using model material such as plasticine, pure aluminium or copper as billets

- Conducting the rotary compression test to simulate the stress state in CWR

These simplifications can provide high efficiency in conducting the tests by saving manufacturing time and cost and guarantee high accuracy in investigating the mechanistic factors by avoiding unnecessary microstructural effects.

Cross wedge rolling prototype apparatus

A CWR prototype with two flat dies was built at the University of Pittsburgh, which was capable of deforming soft metals such as pure aluminium and copper at room temperature [4, 31, 93, 102]. The simplified CWR prototype can be used to track the deformation and fracture evolution conveniently. Due to its small size, 27 pairs of dies with different geometries were manufactured to study the effects of the process parameters on central cracking, which effectively solves the difficulties in manufacturing industrial level CWR dies [31].

Model material

Model materials bring great convenience for the researchers to study the deformation behaviours in metal forming processes. Although the model materials and metal alloys are different in material structures, they exhibit similar mechanical behaviours such as the stress-strain relationship, yield criterion, plastic strain hardening, strain rate sensitivity and fracture, with the flow stress difference in one or two order magnitude [105]. The application of model materials in CWR can be traced back to 1984 when the internal defects were simulated in a rotary side-compression test with plasticine. The shear distortion was observed in the central region of the workpiece [106]. Fu and Dean [107] also used the plasticine to study the defect formation during the necking and twisting. Soft metals such as pure aluminium and copper were

used to study the uncontrolled slipping and internal defects [4, 31, 93]. High similarities between the commercial plasticine and C45 steel were recently achieved in terms of mechanical properties and defect features in CWR [108, 109].

Meanwhile, it is interesting to see that the central crack formation is material independent, which occurs in a variety of solid materials such as steels [7, 108], aluminium [4, 60] and plasticine [106, 108]. Hence, the central cracking during CWR is a general mechanistic problem rather than specific to metals. Thus, it is reasonable to build the fundamental understandings through the model material due to its softness. This enables a wide range of stress states to be investigated by rapidly additive prototyping dies (rollers) with various geometries at a low cost and a short lead time.

Rotary compression test

Rotary compression is a process that a cylindrical billet is compressed along the radial direction as well as rotated driven by the strong tangential force applied by the dies, as presented in Figure 2.1. The feed angle γ is defined to describe the die geometry. This process is usually used as a simplified model for the CWR, which weakens the axial extension effect. The triaxial stress state in CWR is simplified to a plane strain state in the rotary compression. The simplified model greatly facilitates the theoretical calculation and the experimental calibration of the material constants.

The stress-strain distribution of a cylindrical billet in rotary compression was revealed in 1977 [38, 110]. In 1990, the velocity field in a rotary compression condition was proposed based on the upper bound method, which enabled predicting the forming force and contact length in CWR [111, 112]. In 1996, the rotary compression was reused for obtaining the width of the contact area, contact pressure and rotational compression stability [113]. The rotary

compression test was recently conducted to determine the material constants in damage models for central cracking prediction [114–116].

Central cracks appear in rotary compression tests [116], implying that the axial tensile stress is not the critical factor for central cracking formation. Therefore, it is reasonable to investigate the central cracking mechanism based on the rotary compression test.
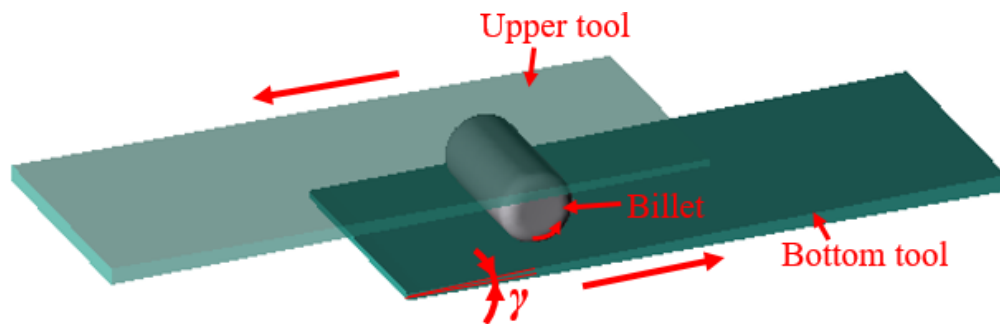
Figure 2.1 Rotary compression configuration.

In this study, the FE model was applied to track the stress/strain/damage distribution and evolution. The central cracking behaviours were observed in a physical model, including a lab-scale CWR prototype, plasticine billets and 3D printed CWR dies.

2.4 Summary

This chapter reviewed the literature relevant to the studied topic, including fracture mechanism and fracture criteria/damage model for central cracking and the latest methods for CWR studies. The mechanical and microstructural characteristics in CWR are very complex, with a wide range of potential critical factors to central cracking. In the previous studies, no comprehensive and comparative work has been conducted to distinguish the critical factors. Meanwhile, a large number of damage models have been applied to predict

the central cracking, but the accuracy was unsatisfying due to the limited understanding of the underlying fracture mechanism. Thus, in this study, the critical mechanistic and microstructural factors to central cracking have been determined, and the physically-based damage model has been proposed and validated quantitatively. A new research method has been developed to address the previous experimental limitations, such as manufacturing a large number of CWR dies to investigate various stress states.

Chapter 3 Methodology

3.1 Introduction

This chapter introduces the research method involved in this study, including physical model, FE model, mechanical test and microstructure characterization.

Section 3.2 details the physical model with the CWR prototype and the plasticine billets. The physical model was used to reveal the cracking behaviours under various die geometries and various material properties (ductility). New plasticine materials were designed to accelerate the occurrence of central cracking for better experimental observations. The softness of the plasticine allowed the CWR dies to be rapidly prototyped with plastic materials. This physical model's application effectively addressed the experimental limitations in manufacturing a large number of CWR dies within limited time and budgets. This physical model was applied to explore the critical mechanistic factor for central cracking and examine the accuracy of all the investigated fracture criteria/damage model.

Section 3.3 briefly introduces the newly designed plasticine materials and the high-strength steels used in the industry. A uniaxial tensile test machine Instron 5543 and thermomechanical simulator Gleeble 3800, were adopted to obtain the stress-strain curves at room or high temperatures. Specific rigs were designed and 3D printed for clamping the soft plasticine specimens. Pre-heat treatment was designed and applied to simulate the practical heat treatment on steels before the CWR process.

The CWR FE model is described in Section 3.4, including selecting FE software, the material model, the friction model and the embedding of the

damage models. A robust CWR FE model was established, with high flexibility for subroutine embedding and high computational efficiency. The material flow, stress/strain/damage distribution and evolution within the workpiece during CWR were outputted.

Microstructural characterisation techniques were applied for revealing the underlying microscopic fracture mechanism, as described in Section 3.4. The quantitative analysis on the microstructure (e.g., chemical/phase compositions, grain size and inclusions) of the high-strength steel billets at both room and high temperatures was conducted to distinguish the dominant microstructural factors for central cracking.

3.2 Cross wedge rolling lab test

Model material, plasticine, was applied to study the fracture mechanism of central cracking on a macroscopic scale. Figure 3.1 compares the stress flows between the hot steel and the plasticine within a strain rate range, showing their high similarities in stress-strain relationships such as work hardening and strain rate dependency. It implies the high similarities in deformation mechanisms and high possibilities to simulate the central cracking behaviours with plasticine. New plasticine materials with different additives were designed and manufactured to obtain specific mechanical properties and generate central cracks in CWR conditions. A CWR prototype was built, capable of reproducing the industrial CWR process in a lab environment.
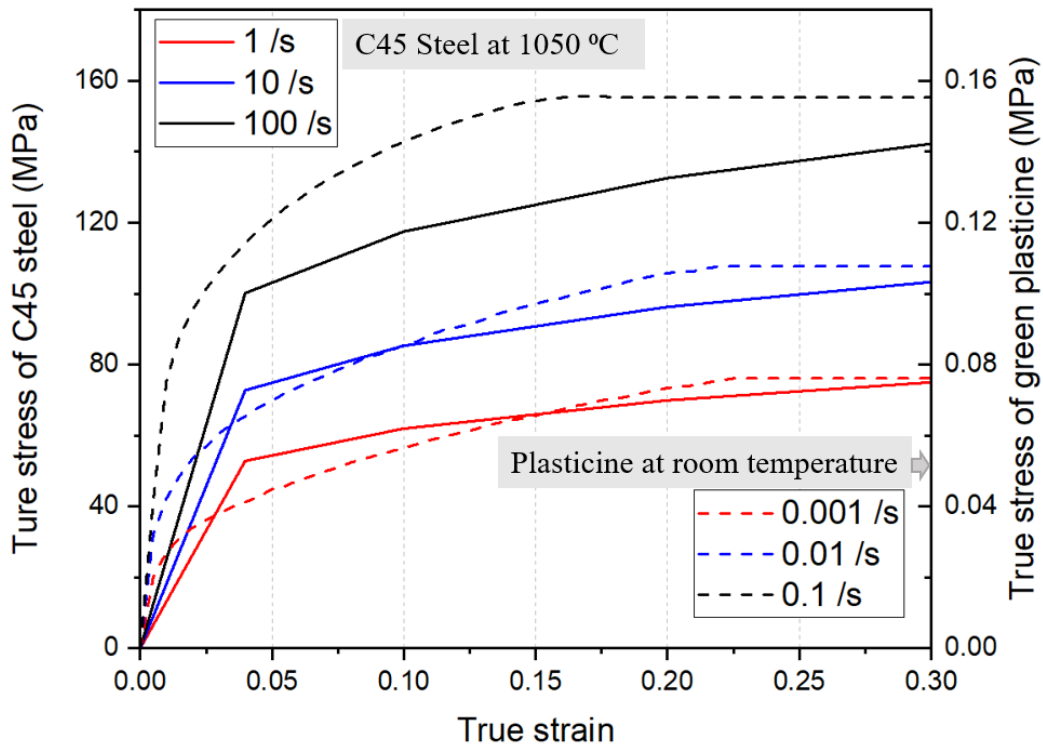
Figure 3.1 Comparison of material flow between C45 steel at 1050 °C and plasticine at room temperature under various strain rates (data for hot steels exacted from QForm material library [117]).

3.2.1 Selection and preparation of model material

Selection of plasticine

Three types of plasticine from three companies were compared to find the suitable model material for this research, including Newplast Modelling Clay 500g bars, Hasbro Playdoh 120g tubs and Flair plasticine 500g slab, as presented in Figure 3.2. The workability of three materials was analysed carefully under plastic deformation. It is found that the modelling clay in Figure 3.2 (a) was dry and crumbly, being difficult to be bonded well after folding. In Figure 3.2 (b), the material was too soft to keep the desired geometry. The plasticine in Figure 3.2 (c) exhibited the desired performance, neither too dry nor too soft, with a great characteristic to achieve homogeneous structure

and desired geometry. More importantly, it features as never-drying, enabling the material property as time-independent. Thus, the Flair plasticine 500g slabs were selected and applied in this research for revealing the fracture mechanism of central cracking.

Figure 3.2 Comparison of three kinds of plasticine (a) Newplast Modelling Clay 500g bar [118] **(b) Hasbro Playdoh 120g tubs** [119]**, and (c) Flair plasticine 500g slab** [120]**.**

Selection of additives

The additive was added to the pure plasticine to reduce the ductility and accelerate the central crack generation. Three types of additives were selected and compared, including fine sand (with a grain diameter ~ 0.1 mm), carbon powder (at nm level) and organic plain flour from Tesco. The cracking morphologies of the samples made by these three different compositions after the same CWR process were compared in Figure 3.3. Central cracking occurred in all three cases. In Figure 3.3 (a), however, it is difficult to distinguish the voids caused by the deformation process or the separation of sands during the cutting process. In Figure 3.3 (b) and (c), the sample mixed with carbon particles or flour showed similar cracking morphology to the metal ones, but the carbon particles caused health and safety hazard due to the very small diameter of particles involved. Therefore, the flour was finally selected as the additive.
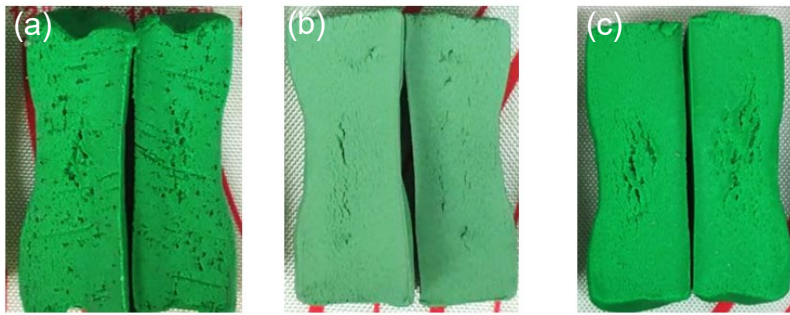
Figure 3.3 Cross wedge rolled samples made by plasticine with various additives at a weight ratio of 10:1 (a) fine sand; (b) carbon powder; (c) flour.

Effects of weight ratio

The weight ratio effects between the additive and plasticine on the material's ductility are presented in Figure 3.4. The weight ratio was calculated by dividing the initial plasticine weight by the initial flour weight. The ductility of this newly designed flour-plasticine composite material decreased with the increase of the flour/plasticine weight ratio. The possible reason is that the high content of flour affects the internal cohesion strength by separating the plasticine matrix.
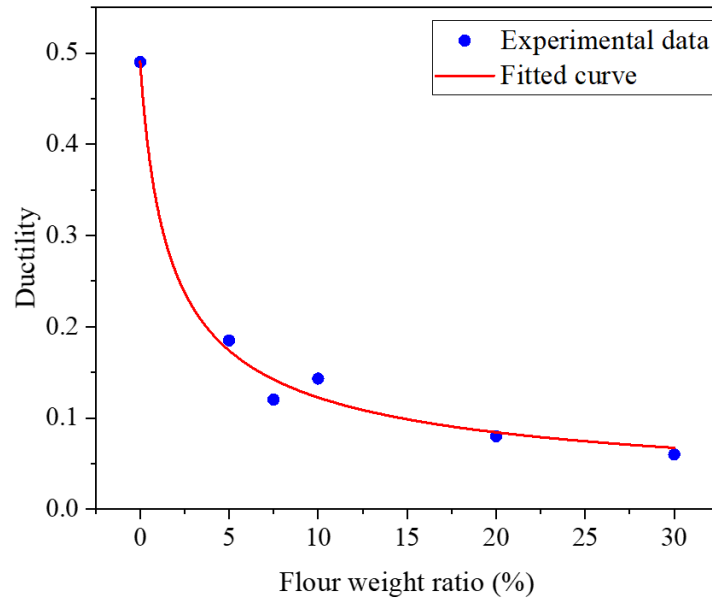
Figure 3.4 Ductility of the materials varying with different flour/plasticine weight ratios.

3.2.2 Sample preparation

CWR test plasticine samples are shown in Figure 3.5. The sample dimensions were kept at $\Phi 25.4 \times 50$ mm^2 in this study. The plasticine from the same batch was selected to keep consistent mechanical properties. The plasticine with the same colour was used for the same series of tests to mitigate the mechanical properties inconsistency caused by different compositions.

The sample preparation process was carefully designed and controlled to keep a high level of consistency in structural homogeneity and geometric accuracy. Initially, the plasticine at a certain weight was cut into small chunks from the initial slabs, and then mixed with the flour at a set weight ratio in a food grinder. Their weights were accurately measured with a digital lab scale with 0.01g resolution. Then, the plasticine and flour mixture were ground into particles at a diameter less than 0.5 mm. Subsequently, these particles were

pressed and rolled manually to a blocky piece, followed by hammering and folding more than ten times to homogenise the structure and achieve consistent mechanical properties. In the end, a cylinder closed to the designed geometry could be achieved. In order to get the high geometric accuracy, a die forging process was applied subsequently. In addition, a utility knife was used to trim the flash and the two ends. The forging moulds were manufactured by 3D printing with the plastic material polylactic acid (PLA).
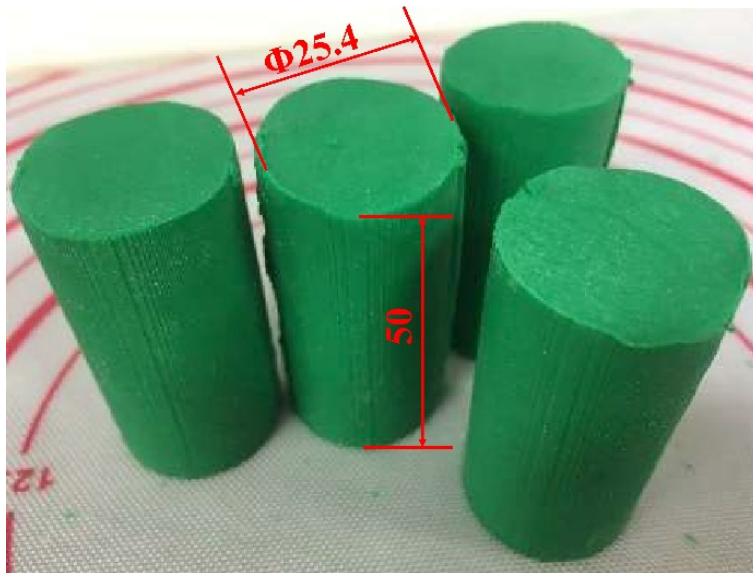
Figure 3.5 Plasticine samples for cross wedge rolling test (unit: mm).

3.2.3 Setup of cross wedge rolling prototype

Figure 3.6 schematically presents the setup of the CWR lab testing rig. A cylindrical plasticine billet is placed in between two flat dies. The upper die is fixed on the frame, while the step motor drives the bottom die. The speed and the moving distance of the bottom die are precisely controlled by an electronically controlled system. The upper and lower dies share the same geometry. The billet rotates along its axle during the test and moves forward, driven by the bottom die. As shown in the inserted figure, a cylindrical billet is deformed into a stepped shaft after rolling. Tests were repeated at least three

times to guarantee the result accuracy. The dies with various geometries were rapidly manufactured by a 3D printer Fortus 400mc with PLA. Only ~ 2 hours is required to manufacture one pair of dies at the cost of ~ £20. Specific stress states on the central region of the workpiece were obtained by varying the die geometries.
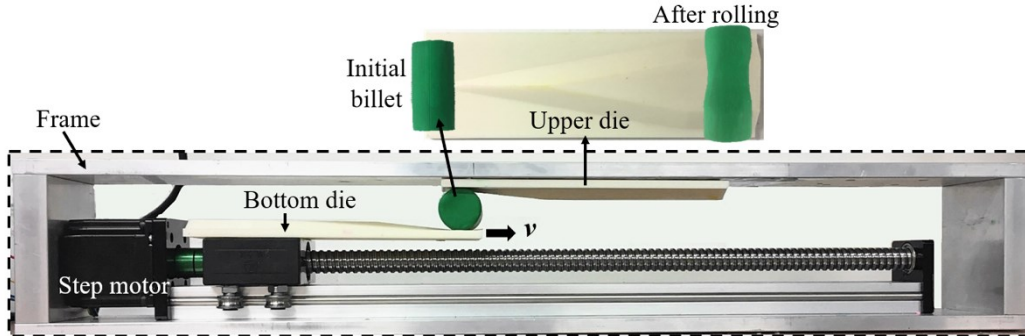
Figure 3.6 Illustration of the cross wedge rolling lab testing rig.

3.2.4 Crack measurement and damage definition

Given that central cracking occurs on the minimum cross-section and propagates along the axial direction, the axial cross-section was examined to define the damage severity. Figure 3.7 presents four rolled products at various damage levels. The central region's damage process is divided into four stages; namely, stage I no damage, stage II void nucleation, stage III macro crack, and stage IV fully cracked. The central region is defined in Figure 3.7 (a) as a rectangle with a length 1/2 of the final length L_f along the axial direction and a width 1/4 of the final diameter D_f along the radial direction. The stage II void nucleation is when separated voids/cracks with a diameter less than 0.5 mm are formed, followed by the stage III macro crack stage when the separate voids coalesce together along the axial direction, as shown in Figure 3.7(c). In stage IV, the crack propagates along the workpiece's whole shaft (Figure 3.7(d)). As observed in the plasticine, the

crack formation process is consistent with the fracture mechanism in metals [27, 31].
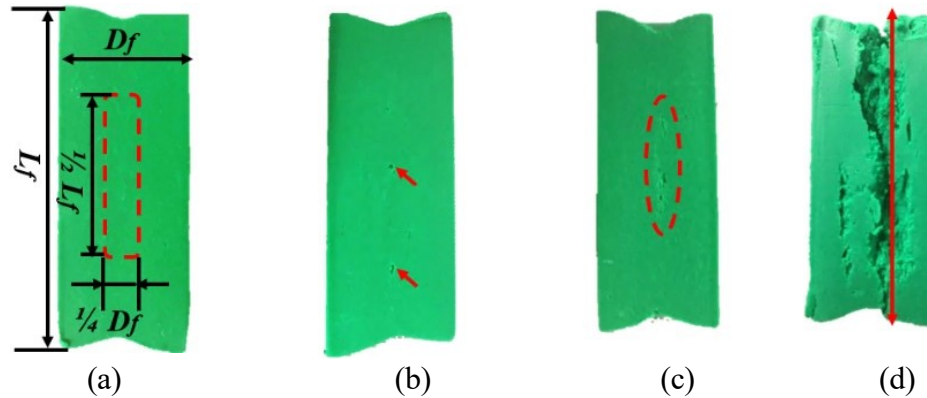
Figure 3.7 Definition of damage levels for quantitative analysis: (a) stage I no damage; (b) stage II void nucleation with voids less than 0.5 mm; (c) stage III macro crack when the void coalescence occurs; (d) stage IV fully cracked when the crack propagates across the whole sample.

3.3 Uniaxial tensile test

3.3.1 Sample preparation

Uniaxial tensile tests were conducted to characterise the mechanical property of the studied materials. Two groups of materials were investigated, the plasticine/flour composites and the high strength steel 20CrNi3H. The specimen geometries are presented in Figure 3.8, designed based on the related standard [121]. The plasticine sample in Figure 3.8(a) was manufactured in the same way as the CWR test plasticine samples introduced in Section 3.2.2. The steel sample was cut from the as-received billets and manufactured to the designed geometry in Figure 3.8(b) by electrical discharge machining (EDM).

The uniaxial tensile test rather than compression test was selected to investigate the mechanical properties of the plasticine for two reasons: (i)

central cracking in CWR is mainly caused by the combination of the tensile stress and the shear stress. The tensile test results demonstrate higher relevance to the central cracking; and (ii) to achieve the fracture parameters e.g., fracture strain.
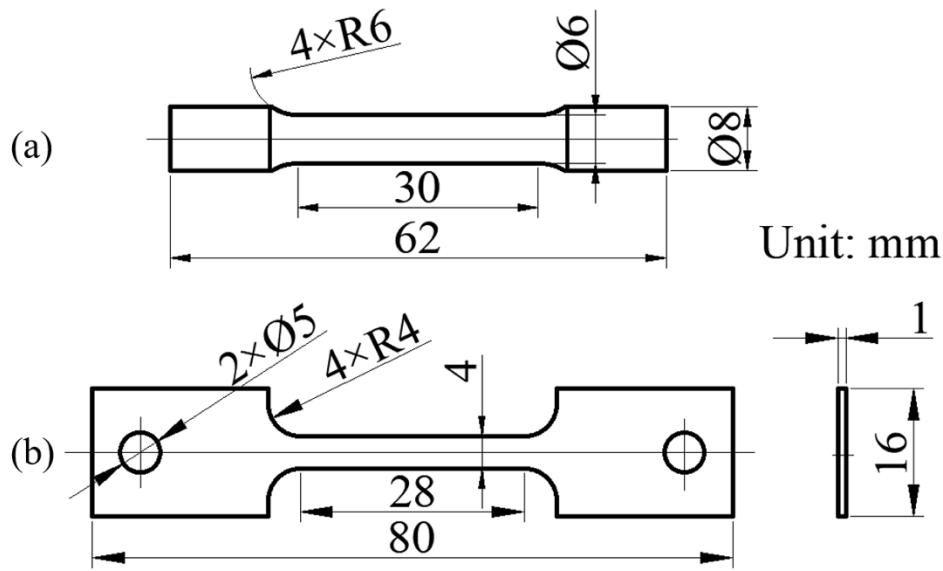
Figure 3.8 Specimens for the uniaxial tensile test of two types of materials: (a) plasticine; (b) high-strength steel.

3.3.2 Test setups

The plasticine samples' mechanical properties were tested by using Instron, while for the 20CrNi3H steel, the Gleeble 3800 was used, as presented in Figure 3.9.

A small load cell 1000 g was used to test the mechanical property of plasticine-based material for achieving high accuracy. The grips were 3D printed using the plastic material, PLA. Steps were designed on the connection holes for effectively clamping the sample without slippage during the test. The engineering stress strain values were calculated according to

the force and displacement readings from the machine and specimen geometries. The convention from the engineering stress/strain curve to the true stress/strain curve referred the report [122]. Each group of tests under the same testing condition was repeated at least three times to determine the average values to ensure the result accuracy.

The thermomechanical simulator Gleeble 3800 was applied for simulating the thermal-mechanical process in the industrial CWR process. The specimen was firstly heated to 1080 °C and then pulled to fracture. A thermocouple was spot welded on the surface of the specimen's central region to record and control the temperature. A dilatometer was applied to record the width change during the tests.
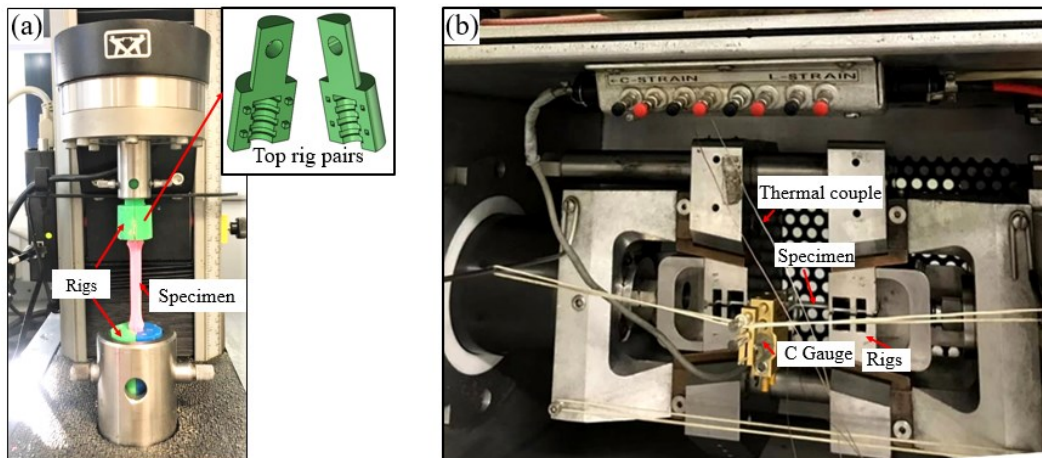
Figure 3.9 Uniaxial tensile test setups for a specimen with different materials mounted on different machines: (a) plasticine on Instron; (b) high-strength steel on Gleeble.

3.4 Finite element model

CWR is a complex metal forming process that includes large plastic deformation, strong shear effects, and a high-temperature gradient. A variety

of FE programs have been applied to simulate the CWR process. However, these FE programs' capability and flexibility to simulate the complex CWR process have never been compared. Therefore, a comparative study has been conducted to determine reliable software for this study. Three FE programs are compared, Abaqus, Deform 3D and QForm.

The example of C45 steel billet being rolled at 1050 °C is taken for this comparative study. The geometry models were built in 3D modelling software ProE and then inputted to corresponding FE modelling software. Issues in terms of convergency, computational efficiency and capability for user-defined subroutines were investigated in detail.

3.4.1 Selection of software

Abaqus

One CWR FE model was built in Abaqus Explicit, as presented in Figure 3.10. Due to the symmetric nature, half of the whole system was modelled. Abaqus Explicit was applied mainly because of its advanced adaptive meshing technique, which enabled the simulation's completion without any convergent problems caused by the severe plastic deformation and strong shear stress. As a result, the workpiece elements after rolling were regularly distributed without substantial distortions, as shown in the insert. The plastic strain increased from the centre region to the surface, consistent with the literature [3]. Figure 3.11 presents the damage distribution on the rolled sample predicted by the R&T damage model and Oyane damage model. The damage models were embedded into the FE model by the user subroutine VUSDFLD. The subroutine code is attached in Appendix A. However, the thermal effect has not been taken into account due to the incompatibility of the adaptive meshing technique with the thermal element. Regarding computational efficiency, it takes over one day to finish one CWR job.

In general, it is not the right candidate due to the incapability of the thermal process and low computational efficiency.
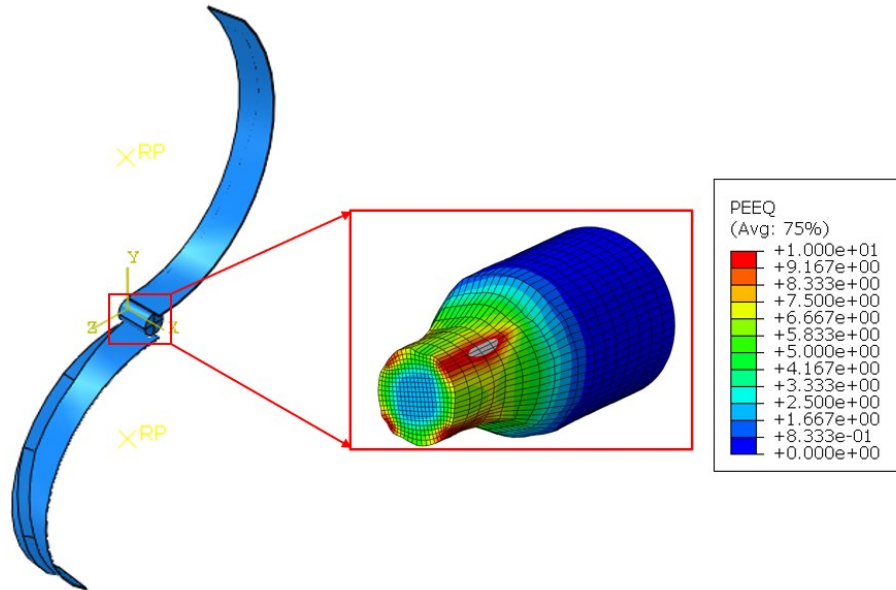
Figure 3.10 Finite element model configuration in Abaqus Explicit along with plastic strain distribution on the sample at the end of the CWR.

(a) Rice & Tracy   (b) Oyane
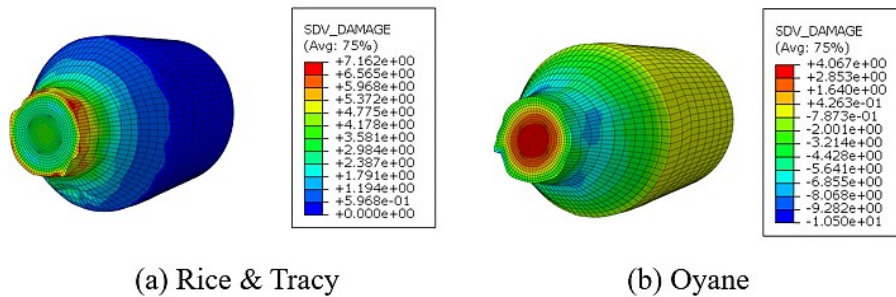
Figure 3.11 Damage distribution predicted in Abaqus predicted by (a) the R&T model and (b) the Oyane model.

Deform 3D

Deform 3D is a specific FE program for the metal forming process with high flexibility in using user-defined subroutines. The literature has proved its competitive capabilities in simulating the CWR coupled with the thermal

process and user-defined subroutines for complex constitutive models [5, 123]. Preliminary work has been conducted, as shown in Figure 3.12. The self-embedded Oyane damage model was applied, and the predicted result is presented in Figure 3.12 (b). It is noted that the convergence problem frequently countered in Abaqus was efficiently mitigated in Deform 3D. Meanwhile, the thermal process was easily coupled with the deformation process. More importantly, the calculating time was significantly reduced due to the adaptive and optimised mesh strategy.

(a) FE model　　　　(b) Damage distribution
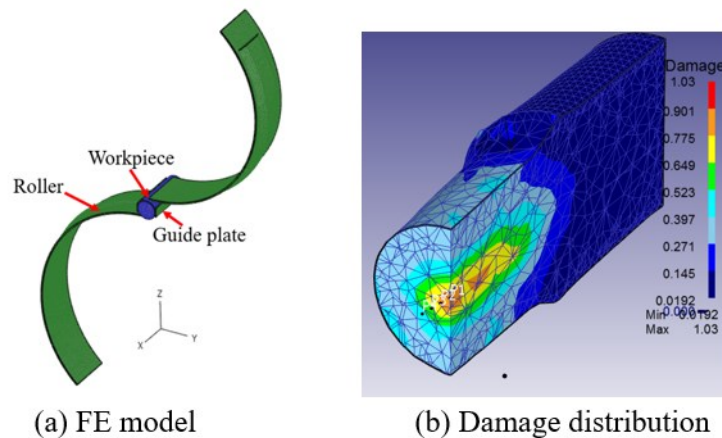
Figure 3.12 Cross wedge rolling simulation in Deform 3D: (a) finite element model; (b) damage distribution on the workpiece predicted by the Oyane damage model.

One disadvantage of Deform 3D lies in the limitation of the multi-processors function. The single Deform 3D license only allows one processor, which limits the computational efficiency. Even so, the computational efficiency of Deform 3D is competitive compared with Abaqus. The approximate computational time to run the created CWR model is around 3 hours.

QForm

QForm, as another specific FE software program for complex metal forming processes, is worth a detailed investigation due to its powerful dual mesh method. The dual mesh method allows the elements to automatically mesh

at the region with high stress/strain localisation or complex geometry, which guarantees high computational efficiency as well as calculation reliability. The computational time is reduced to 2 hours due to the powerful meshing technique and the permit of multi-processors with only one license, which significantly improves the calculating efficiency for the complex metal forming process. Therefore, QForm was selected for this study.

The detailed QForm setting, including the material model, friction model and damage subroutines, are described as follow.

3.4.2 Material model

Due to the large plastic deformation on the workpiece in CWR, the Lévy-Mises equation was applied to describe the stress-strain relationship, which ignores the elastic deformation as presented in Equation 3.1.

$$\dot{\varepsilon}_{ij} = \frac{3}{2} \frac{\dot{\bar{\varepsilon}}}{\bar{\sigma}} \cdot \sigma'_{ij}$$

Equation 3.1

where $\dot{\bar{\varepsilon}}$ is the effective deformation rate, $\dot{\varepsilon}_{ij}$ is the strain rate tensor and σ'_{ij} is the stress deviator.

In this study, three groups of materials are involved for FEA, including the plasticine/flour composites, pure aluminium AA 1100 and C45 steels. The material data of pure aluminium AA 1100 and C45 steels are available in QForm material library. The material database for the plasticine/flour composites were created based on the uniaxial tensile tests.

3.4.3 Friction model

Various friction models are available in QForm, such as the Coulomb friction model, Siebel friction model (also named the constant shear friction model), a hybrid form of Coulomb and Siebel friction models and Levanov friction

model with the consideration of contact pressure. Two classical friction models, the Coulomb friction model and Siebel friction model, are presented in Equation 3.2 and Equation 3.3, respectively. In the Coulomb friction model, the shear stress τ on the contact area is linearly related to the contact stress σ_n with a friction coefficient μ, while in Siebel friction model, the shear stress is a constant, which is related to the maximum shear strength k with the friction factor m. The shear strength is normally defined as $k = \sigma_y / \sqrt{3}$.

$$\tau = \mu\sigma_n$$

Equation 3.2

$$\tau = mk$$

Equation 3.3

The workpiece-die contact condition in CWR is very complex, including large plastic deformation and uneven temperature distribution. The comparison of the Coulomb and Siebel friction models in the CWR was conducted as presented in Figure 3.13. It is found that the friction model does not affect the stress/strain distribution and even magnitudes when the workpiece is appropriately rotated without slipping, as investigated in the reference [124]. The Coulomb friction model with high friction coefficient values (over 0.577) was employed in the FE simulation to prevent the slipping of the workpiece from the dies. However, this high friction value does not cause the frictional stress to exceed the shear yield strength of the materials because of the automatic shear yield stress correction algorithm embedded in QForm [125]. QForm set the maximum value of the friction deduced shear stress to the shearing yield strength of the material to avoid an unphysical stress state. The FE model's accuracy has been experimentally validated by comparing the final geometries of the rolled workpiece in the FE model and physical model.
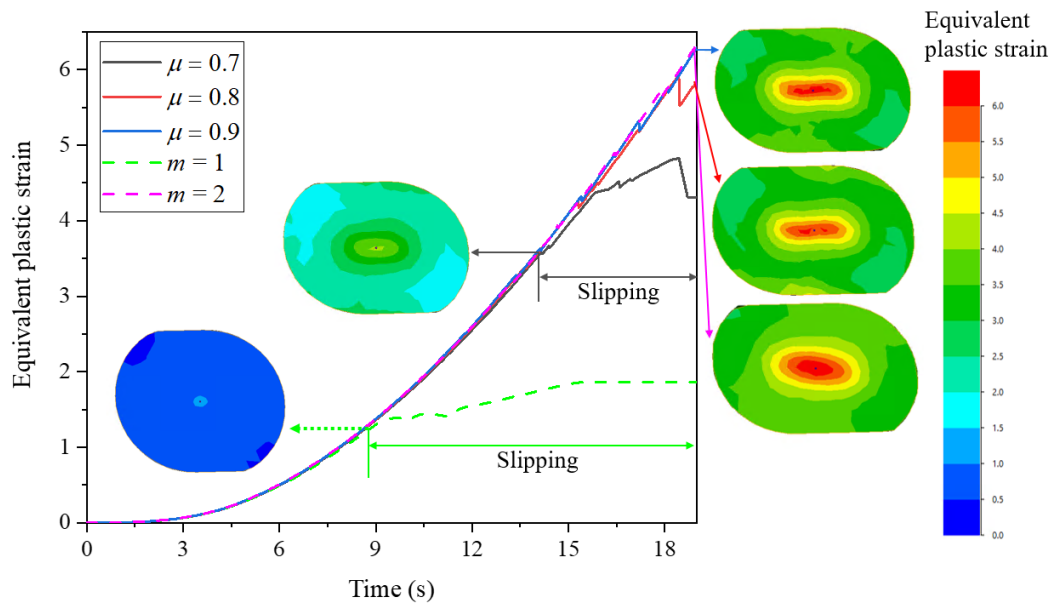
Figure 3.13 Comparison of plastic strain at the central point of the workpiece under different friction models and coefficient values along with the corresponding plastic strain distribution (*μ*: friction coefficient in Coulomb friction model; *m*: friction factor in Siebel friction model)

3.4.4 Damage model

QForm provides a wide range of damage models as well as the flexibility to input subroutines with user-defined damage models. The new damage models were compiled in Notepad written in LUA language and input into the material database. One subroutine code with the damage models is attached in the Appendix.

3.5 Microstructure characterisation

The high-strength steel billets from two batches (one to crack and the other without crack) were analysed and compared carefully on a microstructural scale. The SEM system embedded with EDX and EBSD detectors used in this research is presented in Figure 3.14.

47

Samples were cut from as-received billets by EDM and then ground progressively with grinding papers from P800 to P4000, followed by 1 µm diamond suspension polishing. The polished sample surfaces were then etched by the 2% Nital for approximately 20 seconds to reveal the phase structure. For EBSD characterisations, the samples were polished further via colloidal silica suspension for 20 minutes.

The inclusions in the samples were characterised using optical microscopy (OM) and SEM. The inclusions' statistical distribution was quantified by using Image J software [126], which enable separating the steel matrix with inclusions based on their high colour contrast. SEM/EDX was applied to identify the chemical composition of inclusions.

SEM/EDX was also used to identify the chemical elements Ni, Cr and Mn, across the transverse section. Three points per map were taken at each area, and the average values were calculated.

The phase and grain size evolution were characterised using the Bruker Esprit EBSD system. The SEM operating voltage was 25 kV, the magnification was set at 500x, and the scanning step size was set at 0.5 µm. The post-process for phase identification was carried out using Atex software [127]. A 15° misorientation between adjacent points was set as the grain boundary definition. No smoothing process was applied to these obtained EBSD maps.
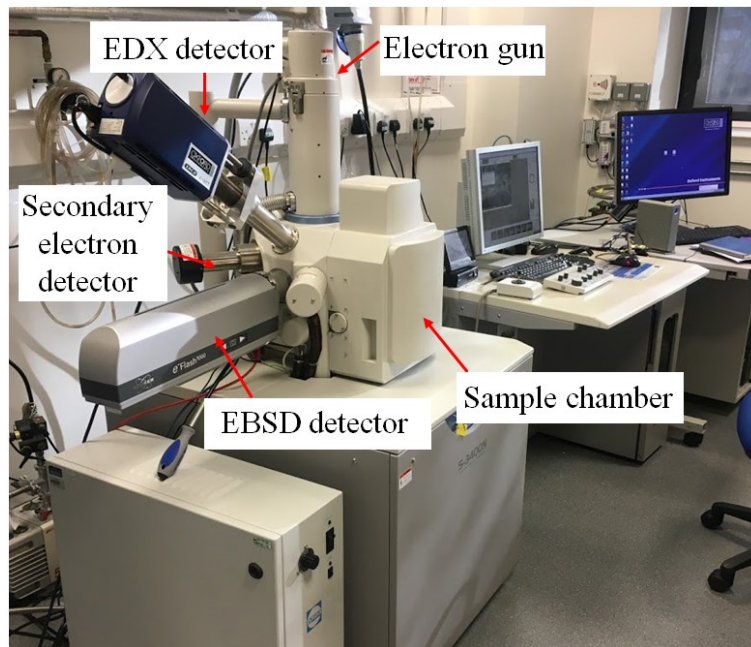
Figure 3.14 SEM system embedded with EDX and EBSD detectors at Imperial College London.

Chapter 4 Central crack mechanism and criterion

4.1 Introduction

Central cracking has been intensively studied in the literature, but the fracture mechanism is still unclear, and there is no robust fracture criterion for central crack prediction. This chapter focuses on establishing the fundamental understanding of the central crack mechanism and criterion based on the mechanistic analysis of the 27 CWR experimental cases with different die geometries. The die geometries and the cracking conditions in all 27 cases are described in Section 4.2, along with the corresponding FE model. A new physically-based fracture criterion was proposed in Section 4.3, which considered the effects of the maximum shear stress and the first principal stress. The mechanistic meaning of the proposed criterion was demonstrated by comparing the classic Tresca criterion and the maximum principal stress theory. In Section 4.4, the workpiece's mechanistic characteristics in CWR were understood comprehensively by analysing the stress/strain distribution and evolution during the CWR. The proposed fracture criterion was then validated by the 27 CWR cases with pure aluminium in Section 4.5. In the end, the central crack mechanism was illustrated systematically from both the transverse and the longitudinal views.

4.2 Descriptions of experimental data and finite element model

Table 4.1 lists the 27 groups of the CWR experimental data on pure aluminium, including the die geometries and cracking behaviours. The die geometrical parameters (area reduction ratio, stretching angle and forming angle) were varied systematically, and the cracks within the rolled samples

were observed accordingly. It can be seen that the increase of the forming angle α prevents the formation of the central crack, while the increase of the stretching angle facilitates the central crack formation. The influence of the area reduction ratio is not evident.

Table 4.1 Central cracking status of 27 cross wedge rolling experiments under various die geometries [4, 31].

Case Number	η (%)	β (°)	α (°)	Experimental results
1	27	3	15	No crack
2	27	5	15	Central crack
3	27	7	15	Central crack
4	35	3	15	No crack
5	35	5	15	Central crack
6	35	7	15	Central crack
7	44	3	15	No crack
8	44	5	15	Central crack
9	44	7	15	Central crack
10	27	3	20	No crack
11	27	5	20	Central crack
12	27	7	20	Central crack
13	35	3	20	No crack
14	35	5	20	Central crack
15	35	7	20	Central crack
16	44	3	20	No crack
17	44	5	20	Central crack
18	44	7	20	Central crack
19	27	3	30	No crack
20	27	5	30	No crack
21	27	7	30	No crack
22	35	3	30	No crack
23	35	5	30	No crack
24	35	7	30	No crack
25	44	3	30	No crack
26	44	5	30	No crack
27	44	7	30	No crack

The corresponding FE model configuration is presented in Figure 4.1. Only the left-hand side of the CWR model was modelled due to the symmetrical

nature of the process and for the sake of computational efficiency. The diameters of the workpiece and the rollers are 25.4 and 500 mm, respectively. The material model and friction model were described in Section 3.4. The material model of the pure aluminium workpiece was selected from the material library in QForm. The friction coefficient between the workpiece and dies was set at 0.6. It was assumed to be zero between the workpiece and the guide plates, as these guide plates were only used to keep the workpiece in place. The friction model and friction coefficient used in the FE simulation were validated experimentally by comparing the final diameter of the CWR formed part between the FE model (22.72 mm) and the experimental one (22.97 mm).
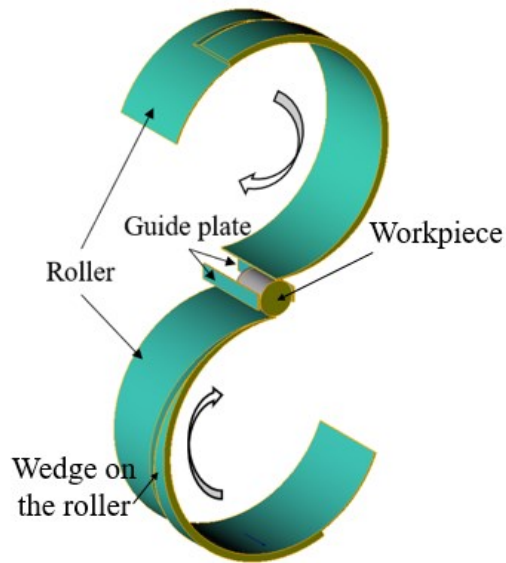
Figure 4.1 Schematic of the cross wedge rolling finite element model.

4.3 Proposal for a new fracture criterion

4.3.1 Definition of the fracture criterion

A new central crack formation criterion is proposed in this study. This criterion considers the effects of the maximum shear stress (τ_m) and the first principal stress (σ_1). It effectively combines the Tresca and first principal stress fracture criterion. The proposed criterion is described in Equation 4.1. Once the damage value D exceeds the critical damage value D_f in the central region, central cracking is predicted to take place.

$$D = A\tau_m + B\sigma_1 \begin{cases} \geq D_f & \text{Central Crack} \\ < D_f & \text{No crack} \end{cases} \qquad \text{Equation 4.1}$$

The material constants A and B are used, which allow this criterion to be applied to various materials. A linear relationship between the contribution of the maximum shear stress and the first principal stress to fracture was defined as $A + B = 1$, allowing to reduce the number of material constants. Then, the proposed fracture criterion was rewritten as Equation 4.2. D_n donates the normalised damage value by the critical damage value D_f.

$$D_n = (\frac{A}{D_f})\tau_m + (\frac{1-A}{D_f})\sigma_1 \begin{cases} \geq 1 & \text{Central Crack} \\ < 1 & \text{No crack} \end{cases} \qquad \text{Equation 4.2}$$

4.3.2 Mechanistic basis of the fracture criterion

The proposed damage model considers two classic fracture criteria, the classic Tresca and the first principal stress fracture criterion, both of which were carefully compared and discussed by Yu [128]. It is well acknowledged that the Tresca criterion can be applied to predict ductile fracture, while the first principal stress theory is more suitable for predicting brittle fracture. Li et al. [129] discovered that the Tresca criterion is accurate for predicting the fracture in the pure shear condition but not accurate when the normal stress

is applied. This is because the fracture in the pure shear mode and the uniaxial extension is led by two different fracture mechanisms, which are not independent under a multiaxial stress state but interact with each other. In the present study that simulates the CWR routine, the central region of the workpiece was subjected to triaxial stresses, with the first principal stress varying among a wide range, whereas the maximum shear stress is accumulating during the whole process. Thus, the interaction and combined effects of the normal stress and the shear stress are considered to determine the damage progress.

Equation 4.1 describes the proposed fracture criterion and considers the fact that under complex stress states, both the normal stress and shear stress are important to generate fracture. If the material is ideally brittle (no evidence of plastic deformation during the fracture process), $A = 0$, and the new damage model is reduced to the maximum principal stress theory with $B = 1$. Whereas, when the material is extremely ductile, B can be regarded as 0, and the new model is reduced to the maximum shear stress criterion with $A = 1$. However, as for general materials, they possess some resistances to both the shear stress and normal stress. If the material behaviour is resistant to normal stress and is weak under shear stress, the fracture mechanism is a shear dominant fracture. Thus, A will be positive and larger than B. If B is positive, it means that the normal stress has a positive effect on the shear dominant fracture. If B is zero, it means the normal stress does not affect the fracture. Otherwise, it has a negative effect and restrains the fracture. This law also applies for B. If B is larger than A, it will be a normal stress dominant fracture, positive A accelerates the fracture, and negative A constrains the fracture.

Figure 4.2 illustrates the fracture locus of the maximum principal stress theory (two vertical dashed lines), Tresca criterion (horizontal dashed line) and the proposed model (two solid lines). Nonetheless, neither the maximum

principal stress nor the Tresca criterion considers the interaction between the normal stress and shear stress and their combined effects on fracture, which are now considered in the new criterion as indicated by Equation 4.1 and Equation 4.2. Note that only the domain above σ axle is discussed because the maximum shear stress ($\tau_m = {}^{(\sigma_1 - \sigma_3)}/_2$) is equal or over zero. $\sigma_{f,t}$ and $\sigma_{f,c}$ present the ultimate strength in uniaxial tension and compression, respectively.
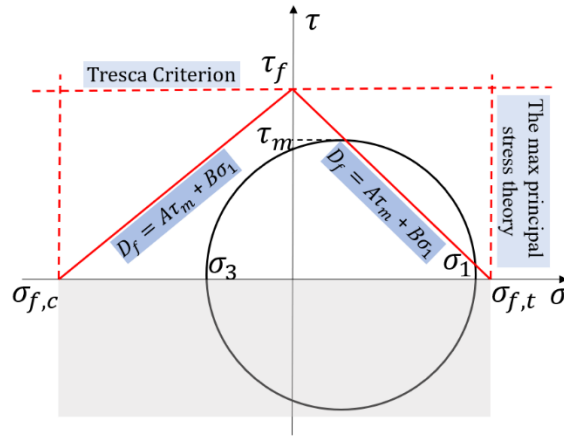
Figure 4.2 Representation of fracture locus by the proposed criterion using the fracture lines and Mohr's circle.

The new model can also be presented as the following to keep consistent with the Tresca criterion and the first principal stress theory:

$$\begin{cases} \sigma_{f,t}\tau_m + \tau_f\sigma_1 = \sigma_{f,t}\tau_f & (\sigma_1 \geq 0) \\ \sigma_{f,c}\tau_m + \tau_f\sigma_1 = \sigma_{f,c}\tau_f & (\sigma_1 < 0) \end{cases} \qquad \text{Equation 4.3}$$

Considering *A* + *B* = 1, this equation set can be rewritten as follow.

$$\begin{cases} \dfrac{\sigma_{f,t}}{\tau_f + \sigma_{f,t}}\tau_m + \dfrac{\tau_f}{\tau_f + \sigma_{f,t}}\sigma_1 = \dfrac{\sigma_{f,t}\tau_f}{\tau_f + \sigma_{f,t}} & (\sigma_1 \geq 0) \\[3mm] \dfrac{\sigma_{f,c}}{\tau_f + \sigma_{f,c}}\tau_m + \dfrac{\tau_f}{\tau_f + \sigma_{f,c}}\sigma_1 = \dfrac{\sigma_{f,c}\tau_f}{\tau_f + \sigma_{f,c}} & (\sigma_1 < 0) \end{cases} \qquad \text{Equation 4.4}$$

Then,

$$\begin{cases} A = \dfrac{\sigma_{f,t}}{\tau_f + \sigma_{f,t}}, B = \dfrac{\tau_f}{\tau_f + \sigma_{f,t}}, D_f = \dfrac{\sigma_{f,t}\tau_f}{\tau_f + \sigma_{f,t}} \ (\sigma_1 \geq 0) \\ A = \dfrac{\sigma_{f,c}}{\tau_f + \sigma_{f,c}}, B = \dfrac{\tau_f}{\tau_f + \sigma_{f,c}}, D_f = \dfrac{\sigma_{f,c}\tau_f}{\tau_f + \sigma_{f,c}} \ (\sigma_1 < 0) \end{cases}$$ Equation 4.5

The constants of *A, B* and *D_f* are now expressed in terms of the fracture/critical principal stress and maximum shear stress, which can be readily determined experimentally. In the case of CWR, the first principal stress σ_1 is always positive. Therefore, these three material constants can be determined by only two simple tests (pure shear test and uniaxial tensile test).

4.4 Mechanical analysis of cross wedge rolling

Complicated stress and strain behaviours are found in the workpiece during the CWR process in Case 3 listed in Table 4.1. The qualitative and quantitative analysis of the von Mises stress and equivalent plastic strain on eight points along the radial direction (P1 - P4) and axial direction (P5 - P8) are revealed in Figure 4.3. Note that P1-8 are initially evenly distributed before rolling. The non-uniform spatial distribution at the final position of the CWR, as seen in Figure 4.3, indicates that the severe heterogeneous deformation occurred on these eight points. The overall effective stress and strain generally increase with the CWR process, given some fluctuations and cyclic variations are found near the free surface caused by the workpiece rotation. Along the axial direction, the central point P1 tends to accumulate higher effective stress and strain (~130 MPa, ~0.7) compared to the points toward the workpiece end, e.g. P5-8 (~120 MPa and ~0.4). However, the central point's stress and strain are much lower than the points adjacent to the outer surface of the workpiece P2-4 (160 MPa and 3.25). This indicates that large plastic deformation occurs near the free surface, and due to the stretching stress along the axial direction, the central interior region is

imposed with higher deformation than the points near the side ends. Note that the central point P1 is neither the highest effective stress nor strain points during the CWR process. It implies more detailed analyses of the stress and strain states are required to understand the mechanistic crack formation process.

The exact stress and strain states in the tensor forms under the free surface and the central point during the CWR process (Case 3 in Table 4.1) are interrogated and shown in Figure 4.4. The stress and strain components vary in a more complex form than the effective stress and strain, particularly for the point near the free surface due to the workpiece rotation. Large in-phase and out-phase oscillations between tensile and compression exist in almost all stress and strain components.

The stress and strain state variations are in a simpler form at the central point. However, the terms of stress and strain are still complex to interpret. The predominate stress terms σ_{xx} and σ_{yy} of the workpiece's central point (Figure 4.4 (c)) are under tension along the axial and radial direction, while the σ_{zz} and shear stress σ_{zx} are in compression state, and their magnitudes are relatively smaller. Further, the strain components generated at the centre (Figure 4.4 (d)) follow a similar trend as stresses with some minor fluctuations for ε_{yy} and ε_{zz} due to the workpiece rotation. Note, that the peak value of the axial stress and strain is found at different stages. The peak strain along the axial direction of 0.9 is found near the end of the rolling process, i.e. at the sizing stage (in Figure 4.4 (d)), so is the highest stress as shown in Figure 4.4 (c).

Therefore, based on the stress-strain analyses, it can be concluded that on the workpiece's transverse section, the surface is subjected to the largest plastic deformation and material flow, while at the central region, the large axial and radial tension presents.
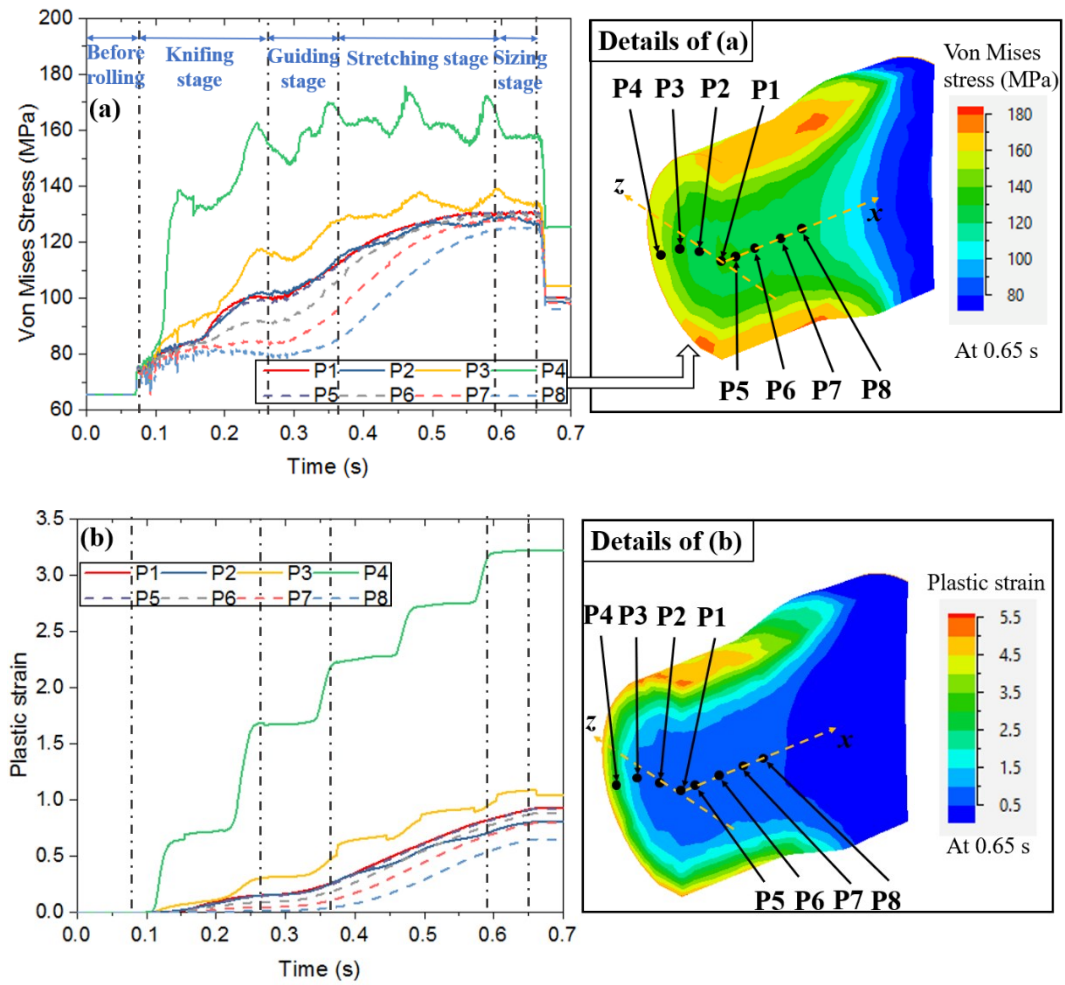
Figure 4.3 Stress and strain distributions on the workpiece along the radial and axial directions during CWR (a) von Mises stress and (b) equivalent plastic strain.
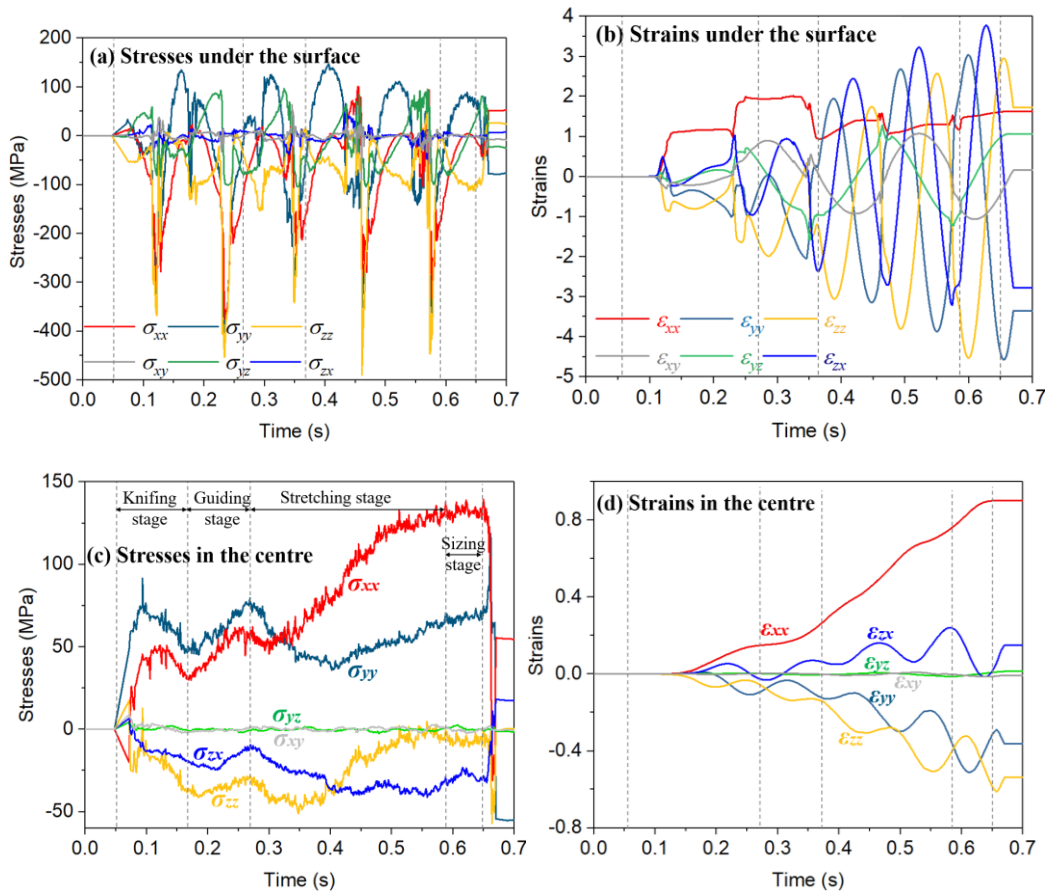
Figure 4.4 Stress and strain evolution (a)(b) under the surface and (c)(d) in the centre during the CWR.

4.5 Validation of fracture criterion

All 27 experimental tests of dies and the CWR processes were simulated by QForm. Four representative cases were selected to demonstrate the variation and evolution of the existing damage criterion (accumulated plastic strain and C&L damage model) during the CWR at the central point, as shown in Figure 4.5 (a) and (b). The first two cases (case 2 and case 3) cracked, while case 1 and case 7 did not crack. The damage values based on the selected cases keep increasing during the CWR and reach the peak value at the end of the CWR. This is expected as these two failure models are strain

or energy accumulated damage models. It is clear that these models are not appropriate to predict central crack formation. For example, case 7, with the highest plastic strain and the highest C&L damage value among the four cases, did not crack.
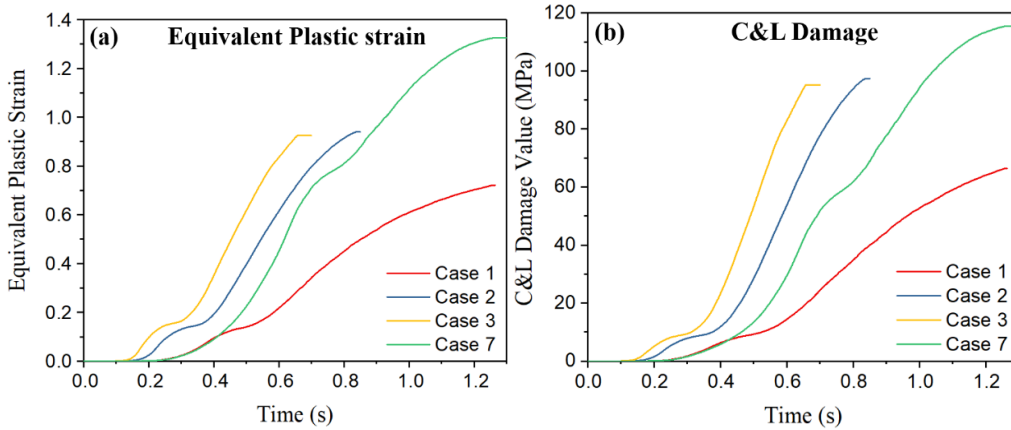
Figure 4.5 Details of the damage evolution of 4 selected cases predicted by different damage models: (a) the maximum plastic strain criterion and (b) the C&L damage model.

A more quantitative investigation was conducted to examine all 27 cases using all four commonly used fracture criteria. These criteria are found to be accurate to some extent; however, none of them can reliably predict (>80% accuracy) whether the central crack will form for a given die geometry. The statistical results are presented in Figure 4.6, for which the *x*-axis represents the case number, and the *y*-axis shows the highest damage value found during the CWR for the given die geometry. Black dots represent no cracking found, while the white dots represent cracking found after the CWR tests. A clear horizontal cut between the dark and white dots will be observed if a reliable fracture model is found, as it indicates a critical damage value to differentiate the cracking and no-cracking cases. The dots are not randomly distributed, as some patterns can be seen in these four plots. This is the result due to the systematic variation of the die parameters. However, the white and black dotes are mixed up for all four failure criteria, and hence, no critical

value can be determined. Therefore, these four damage models are not suitable for the prediction of central cracks in the CWR routine.
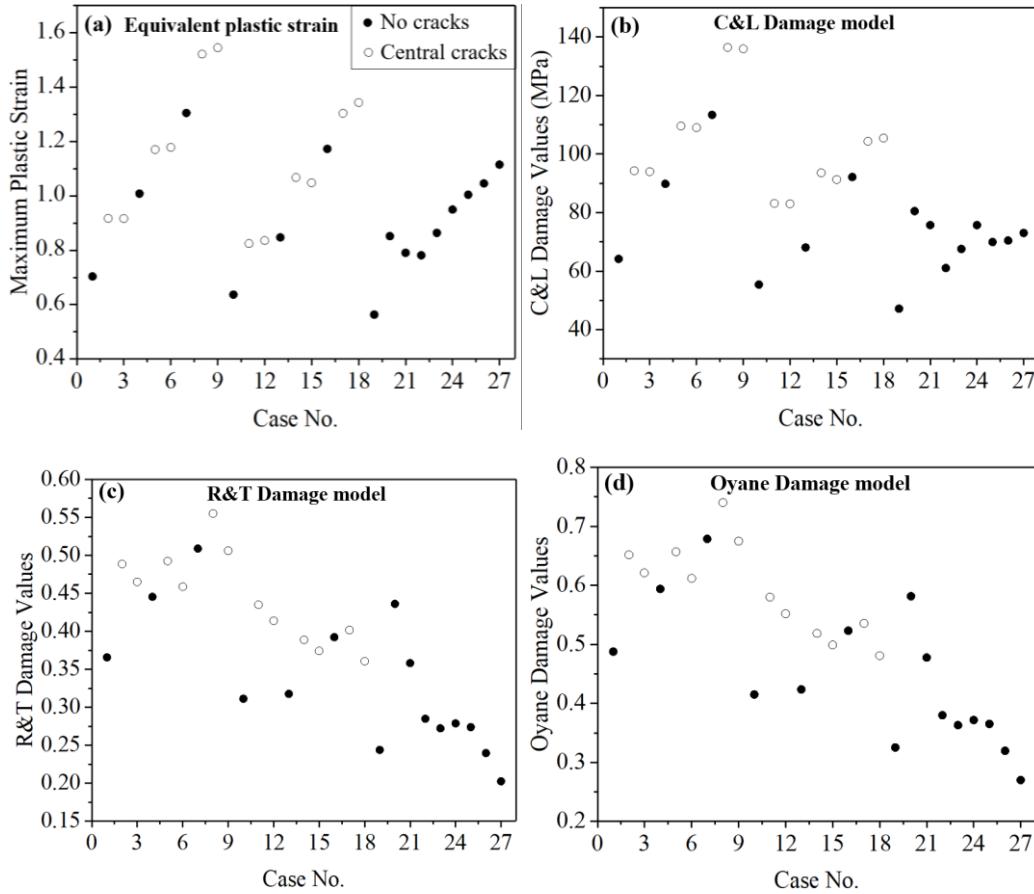
Figure 4.6 Results of damage distributions of 27 cases simulated using different damage model (a) the equivalent plastic strain criterion, (b) C&L damage model, (c) R&T damage model, and (d) Oyane damage model.

The maximum strain criterion integrates the equivalent plastic strain ($\bar{\varepsilon}_p =$ $\int \sqrt{\frac{2}{3} d\varepsilon_{ij}^p d\varepsilon_{ij}^p}$) during the deformation process. However, the signs of the strains (tensile or compressive) are not distinguished in this model. Hence, for deformation involving oscillating tensile and compressive strains, as in CWR, it is difficult to predict fracture accurately. The C&L damage model is energy-based and integrates the maximum tensile stress and the equivalent plastic strain. This damage model is based upon the first principal stress,

which ignores the effect of severe shear effects. The R&T model and Oyane model are based on the relation between stress triaxiality and micro-void growth, but these two models do not consider the severe shear effects.

The limitations mentioned above might be due to the lack of understanding of the actual fracture mechanism in CWR. For example, shear stress, which has been shown to have a significant effect on central crack formation as indicated by Li et al. [53] and Yang et al. [27], is not considered by any of these models.

Through the analyses of the complicated stress and strain state distribution and evolution during the CWR and the thorough comparison of the effects of three key die geometrical parameters on central crack formation in all 27 cases, a new failure criterion is proposed and shown in Section 4.3. It is proposed that the central crack formation is mainly driven by the combined effects of the first principal stress and shear stress. It can be expressed in a formed of $D = A\tau_m + B\sigma_1$ as seen in Equation 4.1.

High accuracy is achieved using the newly proposed criterion to predict the central cracking in all 27 cases. As presented in Figure 4.7 (a), contrary to previous failure criteria, dark and white dots are clearly separated using this new principal and maximum shear stress-based criterion. A line can now be drawn to determine all cracked and no cracked cases among all 27 cases. The critical damage value is defined and normalized as 1 for easy comparison between different materials. Take a closer look at the damage evolution of this new criterion by revisiting the previously selected four specific cases, namely, case 1, 2, 3 and 7. In Figure 4.7 (b), the calculated damage value is shown in the function of processing time. The highest damage values for each case are ranked correctly. For example, the cracked case 2 and 3 displayed higher damage values than the no cracked case 1 and 7. Significantly, case 7 previously incorrectly predicted that the highest

damage value among these four cases is predicted correctly using the new criterion. It is also interesting to note that the peak damage values do not always occur at the end of the process; in some cases, the high damage value is found in the knifing or stretching zone. Furthermore, the first principal stress σ_1 is changing its direction. Initially, its direction is along the radial (*y*) compression direction during the knifing stage. This direction changes to the axial (*x*) direction during the stretching stage, where the axial extension is predominated (see details of Figure 4.7 (c)). Case 3 was considered as an example to show the evolution of the stress components and their damage values during CWR as Figure 4.7 (c) that the first principal stress σ_1 increases in the knifing portion, and has some slight fluctuations during the next stage, after which it increases significantly and reaches the highest value at the end of the whole process.   The maximum shear stress τ_{max} was calculated by $(\sigma_1 - \sigma_3)/2$ and was noted a constant increase in its value until to the end of stretching stage. Further, the proposed damage model exhibits a similar trend as that of τ_m. The maximum damage value in case 3 exceeds the critical value of 1 at the end of the stretching stage, thus confirming the occurrence of the central crack.

Only three material constants (*A*, *B* and D_f) exist in the new damage model. The values of these three constants in this study for highly stained pure aluminium AA1100 H16 are obtained through data fitting of the 27 experimental cases, in which the damage value calculated based on these three constants should clearly discriminate the cracked and none cracked cases. The values were determined as: *A*= 0.94, *B* = 0.06, and D_f = 77.64 MPa, as parameters used in Equation 4.1. The numerical values (*A* and *B)* determined for the proposed model indicate this material during CWR is a shear stress dominant fracture, while the first principal stress is acting to accelerate the shear fracture, which is consistent with the findings made by Yang et al. [27] and later by Yamane et al. [130].

$$D = 0.94\tau_m + 0.06\sigma_1 \begin{cases} \geq 77.64 \text{ MPa} & \text{Central Crack} \\ < 77.64 \text{ MPa} & \text{No crack} \end{cases} \qquad \text{Equation 4.6}$$
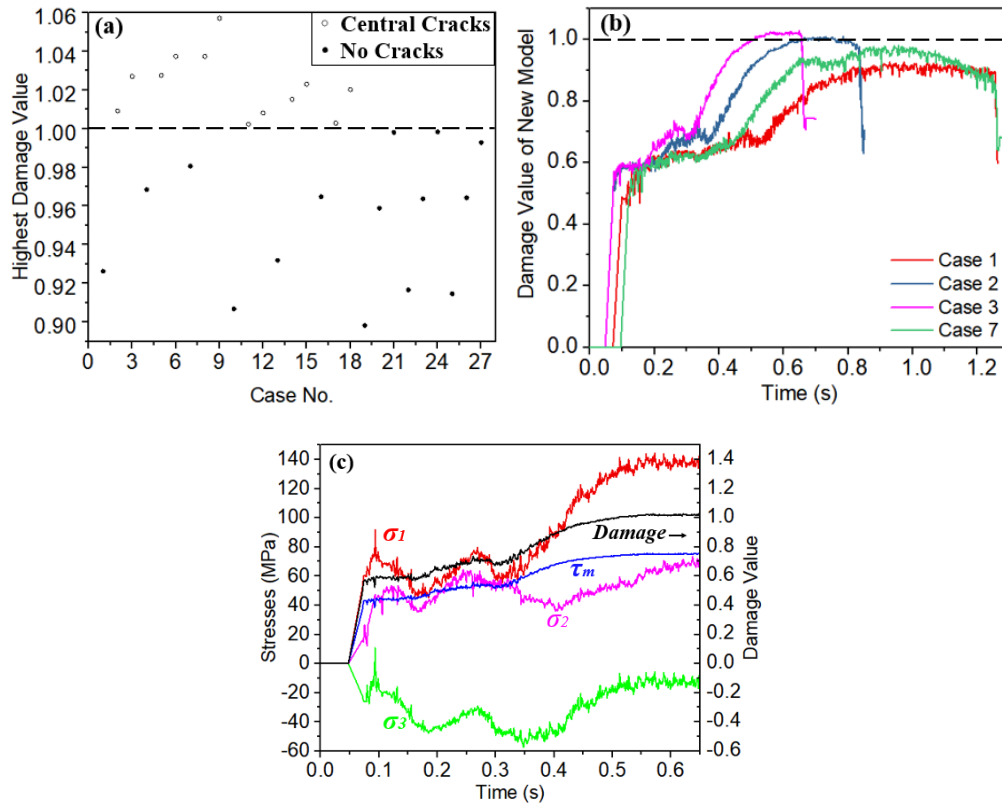
Figure 4.7 Details of damage evolution and distribution generated using the novel fracture criterion (a) comparison of the predicted damage and experimental results (hollow dots represent the experimentally cracked cases, while the solid dots mean non-cracked cases); (b) damage evolution of 4 specific cases; (c) stress components and damage evolution as a function of time for the case 3.

The predicted damage morphology at the transverse and longitudinal section of the workpiece is in excellent agreement with experimentally observed fracture morphology. The comparison is shown in Figure 4.8, indicating the high accuracy of this new damage model.

65
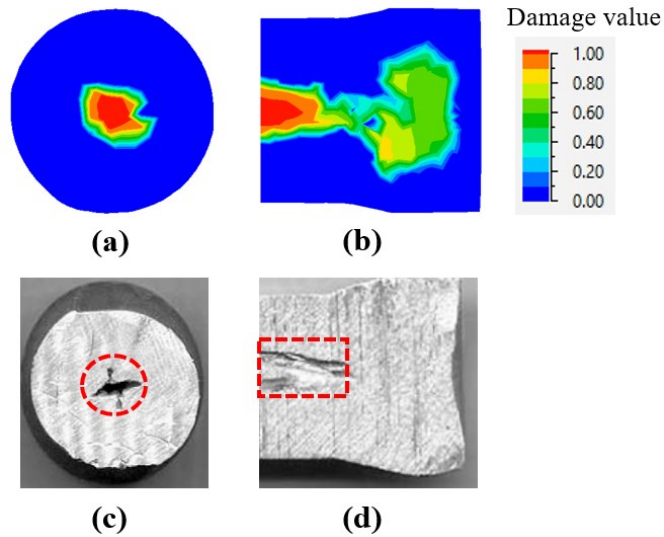
Figure 4.8 Patterns of fracture location from the simulation results and experimental process (a) transverse section of simulated result; (b) longitudinal section of simulated result; (c) transverse section of experimental result [53]; (d) longitudinal section of experimental result [53].

4.6 Fracture mechanism in cross wedge rolling

The new damage model expects to work for both shear and principal stress-driven fracture. These two failure modes can occur in the workpiece's central region during CWR, depending on the material properties and the designed die geometry. Materials (e.g. Al 1100 and AISI 1045) submitted to the CWR show evidence of void growth and coalescence in the central region as observed by Li and Lovell [49], Huo et al. [8] and Yang et al. [27]. Therefore, the fracture mechanism was assumed to be ductile fracture. However, with different materials or stress states, it is possible to be brittle fracture. Therefore, in this study, it is assumed that both fracture mechanisms exist, and they interact mutually.

The speculated fracture mechanism of the central crack in CWR is illustrated in Figure 4.9. This is based on the stress and damage analyses presented in

Section 4.4 and 4.5. Figure 4.4 (c) shows that the maximum shear stress at the stretching stage is on the transverse plane, allowing the void nucleation on the shear bands as the red lines shown in Figure 4.9(a). After voids nucleation, the voids propagate quickly due to the combined efforts of the normal stresses σ_{yy} and σ_{zz} and the shear stress σ_{zy}. The cyclic normal stresses (varying between negative and positive) caused by the workpiece rotation lead to sharp void ends. The shear stress σ_{zy} keeps increasing at the beginning of the stretching stage, increasing the voids' ovality, followed by the strong stress localisation. Once sharp ends are formed, these voids can propagate and coalescence very quickly and finally form macrocracks, as shown in Figure 4.9(b) and (c). This finding agrees well with our predicted damage value morphology at the transverse and longitudinal section, as seen in Figure 4.8.

On the longitudinal section, the voids are growing in a distinct way compared to the transverse section. The voids are elongated along the axial direction due to the presence of the large axial stress. Meanwhile, the maximum shear stress transfers to the longitudinal plane, which accelerates the void nucleation and the propagation of the existing voids. Then, the micro-voids form near the original voids' tips and propagates through a specific path as indicated by the red lines in Figure 4.9 (b) and (c). Anderson [131] noted that the crack propagation path might form approximately 45° degrees with the workpiece's axial direction, depending on the material property and the ratio of axial stress and radial stress. Once the workpiece rotates, the shear bands start to vary, generating a new crack path that always propagates along the axial direction.

In short, the microcracks initiate on the shear bands due to the maximum shear stress on the transverse plane. The cyclic loadings and increasing

shear stress accelerate crack propagation. On the longitudinal section, the workpiece rotation can control the propagation path.
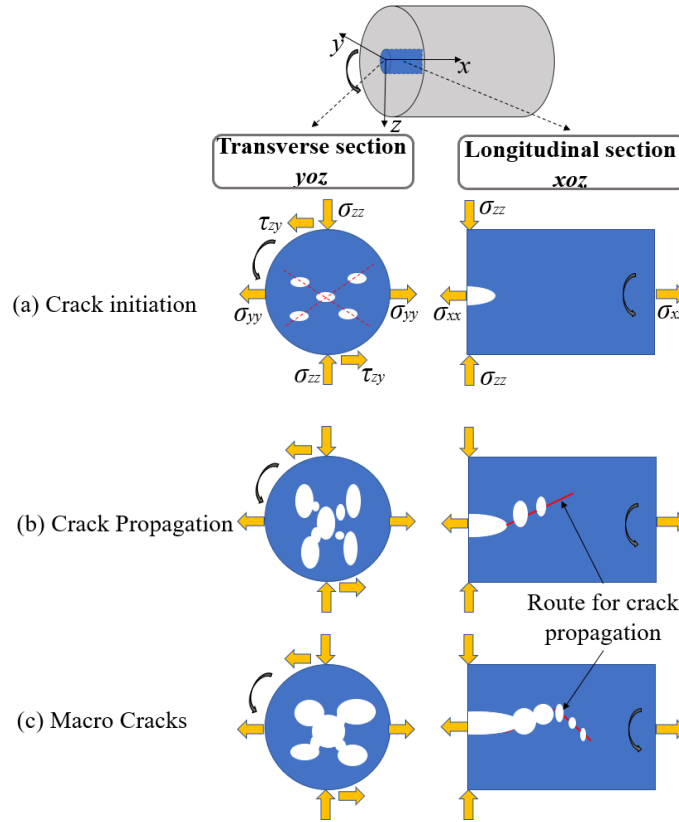
Figure 4.9 Schematics of fracture mechanisms patterns of central cracks produced by the cross wedge rolling: (a) crack initiation; (b) crack propagation, and (c) macro cracks.

4.7 Conclusion

In this study, a new shear stress driven fracture criterion is proposed to predict the central crack occurrence in the CWR. 27 rigorous experimental CWR cases with various die geometries have been simulated by QForm to investigate material response in the CWR. Complete knowledge of the stress, strain states and evolution through the CWR process was obtained, and the

key factors influencing the central crack formation have been identified. The main findings can be summarised as:

1) Two stress components (the first principal stress and the maximum shear stress) have been identified to be critical to central crack formation. The highest first principal stress occurs in the central region, while the maximum shear stress in the central region is accumulating during the CWR process.

2) The maximum shear stress driven central crack formation is found for Al 1100, CWR at room temperature. Void nucleation is caused by the maximum shear stress assisted with the longitudinal stress on the transverse plane. The crack propagation is accelerated by the normal stresses (cyclic stresses on the transverse plane and the axial stress on the longitudinal plane).

3) The maximum shear and first principal stress-driven fracture criterion is proposed based on the Tresca and first principal criterion with the fundamental understanding of fracture mechanisms in CWR. Compared with the other four studied fracture criterion or damage models, this proposed criterion shows improved accuracy in all 27 CWR cases.

Chapter 5 Physical investigation of central crack mechanism and criterion

5.1 Introduction

The maximum shear stress and the first principal stress were considered critical to central crack formation in the last chapter. Many other mechanistic factors such as axial tensile stress, secondary tensile stress and cyclic loadings have been claimed crucial for generating central cracks. However, no comparative research has been conducted to clarify the dominant effects of the maximum shear stress and the first principal stress. Moreover, the material constants in the newly proposed fracture criterion were determined based on a large number of CWR tests with various die geometries, which causes high inconvenience for the industrial applications due to the high cost and lead time in manufacturing various-shaped dies. In this chapter, the proposed fracture mechanism and criterion were validated experimentally, and an effective and efficient material constant calibration method was proposed.

The FE model and physical model are described in Section 5.2. The plasticine materials allowed to generate specific CWR stress/strain states by rapidly printing the plastic dies with different geometries. In total, nine pairs of CWR dies were manufactured. A new method to determine the material constants associated with the proposed fracture criterion was proposed in Section 5.3. The introduced simplified die geometry provides high cost and time efficiency for industrial application. The experimental and simulated results under nine pairs of CWR dies at different geometries are displayed in Section 5.4. The individual effect of all the potential mechanistic factors was clarified by comparing the cracking behaviours under all the stress states,

71

and the predominant factor was distinguished. Meanwhile, the fracture evolutions predicted by the fracture criterion and observed in the experiments were compared and match well for the first time. In Section 5.5, all the potential mechanistic factors were systematically discussed, which validated the predominant effects of the maximum shear stress and the first principal stress. The new method to determine the material constants was validated as well. A deeper understanding of the fracture mechanism was achieved by clarifying the individual effect of a wide range of mechanistic factors.

5.2 Descriptions of the physical and finite element model

The physical model of the lab-scale plasticine CWR test and the CWR FE model were established simultaneously. The physical model was applied to observe damage/fracture evolution, and the corresponding FE model was adopted to track the stress/strain and damage distribution and evolution.

5.2.1 Physical model

The sample preparation and the CWR test procedures are clearly described in Section 3.2. Two types of samples were prepared for different purposes. The one made by the green and pink plasticine layers was for the observations of the material flow. The other one made by green plasticine mixed with 7.5 wt% flour was for the investigation of the fracture mechanism and criterion. The flour weight ratio was designed at 7.5%. At levels above this, the material gets too crumbly to form the sample shapes, and at levels below 7.5%, it is difficult to generate central cracks. The sample dimension keeps constant with the pure aluminium samples in Chapter 4, $\Phi 25.4 \times 50$ mm^2. The true stress/strain curves of the two types of plasticine are shown in Figure 5.1, obtained by conducting the uniaxial tensile tests on an Instron test machine, as illustrated in Figure 3.9(a).
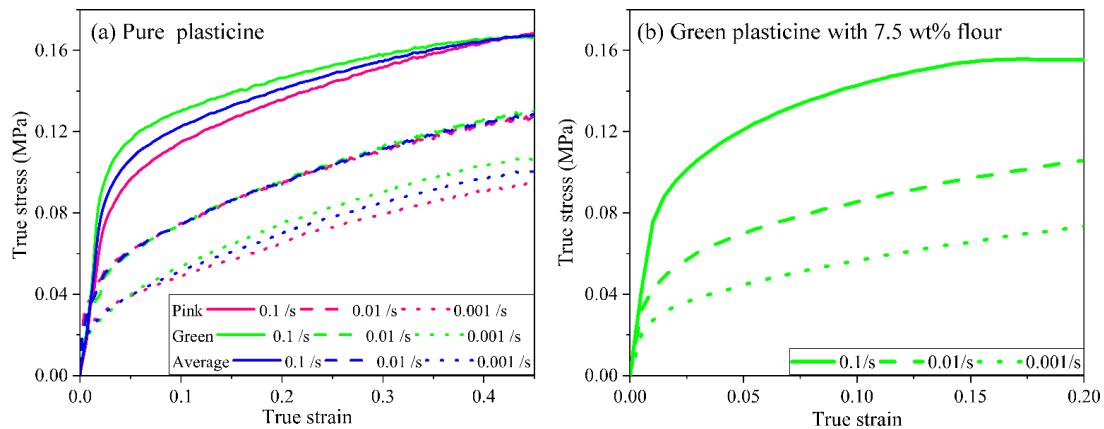
Figure 5.1 True stress-strain curves of plasticines at various strain rates: (a) pure plasticine and (b) green plasticine with 7.5 wt% flour.

5.2.2 Finite element model

The configuration of the CWR FE model is shown in Figure 5.2. Only half of the model was calculated due to the symmetrical feature for high computational efficiency. The true stress-strain data at various strain rates shown in Figure 5.1(a) and (b) was input to create the material database for the pure plasticine and plasticine/flour composite. The material properties such as the density, Young's modulus and Poisson's ratio were input and listed in Table 5.1. The density of the material was calculated by the measured weight and volume of the manufactured samples. The Young's modulus was calculated based on the stress/strain curves, while the value of the Poisson's ratio was averaged based on the investigations of plasticine materials in literature [132, 133].
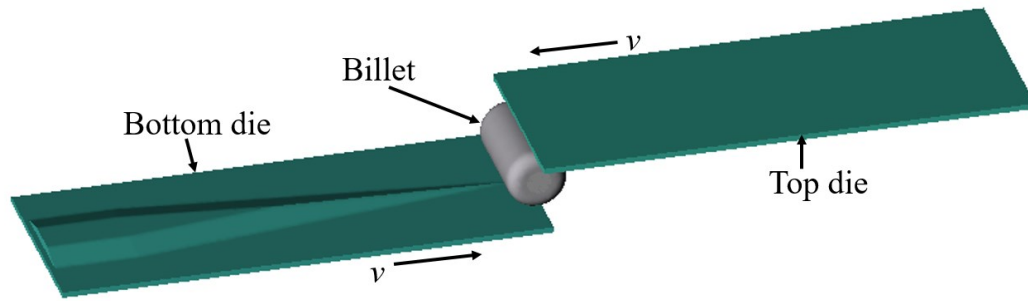
Figure 5.2 Finite element model for cross wedge rolling process.

Table 5.1 Material properties for the new plasticine materials.

	Density (kg/m³)	Young's modulus (MPa)	Poisson's ratio
Pure plasticine	1868	2.6	0.4
Plasticine/flour composite	1714	5.8	0.4

Due to the shortage of ABS material data, a rigid material, H13 steel, was selected from the QForm material library to describe the die deformation behaviour. This was considered reasonable because the deformation of the ABS die observed during CWR was minimal. The Coulomb friction model with the friction coefficient 0.9 was applied to define the contact behaviours between the workpiece and the die, which was validated by comparing the final geometries of the billets achieved from the FE model and the CWR test. More details about the material model and the friction model can be found in Section 3.4.

5.3 A new method for determining fracture criterion

The fracture criterion in Equation 4.1 can be rewritten as Equation 5.1 by defining $D_{nn} = D/A$ and $C = \frac{1-A}{A}$. Then only two material constants, C and $D_{c,nn}$, are involved in this criterion, which vary with material types.

$$D_{nn} = \tau_m + C\sigma_1 > D_{c,nn} \qquad \text{Equation 5.1}$$

The material constants $D_{c,nn}$ and C in the studied fracture criterion can be characterised by the CWR tests with simplified dies, as described in Figure 2.1. By varying the feed angle γ, various stress states can be achieved. To solve the two variables $D_{c,nn}$ and C in Equation 5.1, three simple steps are required: (1) determining the cracking nucleation points in two CWR conditions, i.e., under two different feed angles, by interrupted tests. The central crack condition in each sample can be checked by sectioning the rolled sample along the axial line; (2) calculating the stress states (*i.e.* the maximum shear stress and the first principal stress) at these two specific moments by FE modelling; and (3) solving the two variables $D_{c,nn}$ and C by inputting the acquired maximum shear stress and the first principal stress in two states into Equation 5.1. Principally, only two groups of data will be sufficient for determining the material constants. The accuracy can be further improved by collecting more testing data.

This method is advantageous over the conventional ways, such as a uniaxial tensile test or shear test, mainly because it simulates the stress states in the CWR process and central cracking behaviours, ensuring high accuracy. Meanwhile, compared with the fitting method used in Chapter 4 requiring many CWR dies, it only needs one pair of slopped/flat plates by raising the plate end to get different slopes in real applications. This method will benefit the industry significantly by its high calibration accuracy and considerable time/cost efficiency.

5.4 Results

5.4.1 Validation of finite element model

The plasticine CWR FE model was validated by comparing the final geometry and material flow within the rolled sample with the corresponding experimental data. The die with a forming angle of 15°, a stretching angle of 7° and an area reduction ratio of 44% was applied for this comparative study.

Geometry comparison

Figure 5.3 illustrates the rolled samples from the FE model and the physical model and defines the geometrical parameters, including the final length L_f, the minimum diameter D_{min} and the maximum diameter D_{max}. The comparative results are presented in Figure 5.3. It shows that the highest absolute deviation (relative to the physical value) of the three parameters is 6.6%, within the 10% range, considered acceptable for the validation of soft materials [134].
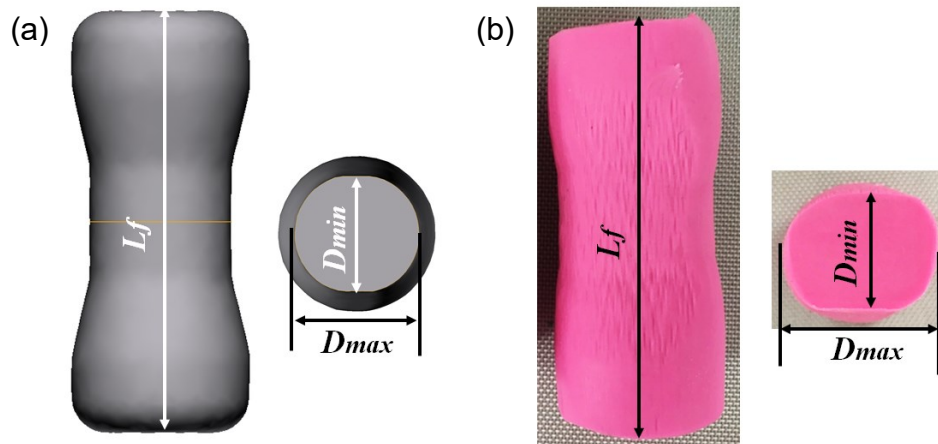
Figure 5.3 Geometrical comparison between (a) finite element model and (b) physical model.

Table 5.2 Comparison of the workpiece's geometrical parameters resulted from the finite element model and the physical model.

	Physical results (mm)	*Finite element results (mm)*	*Absolute deviation (%)*
D_{min}	18.7	18.6	0.5
D_{max}	22.8	21.3	6.6
L_f	56.7	59.4	4.8

Material flow comparison

The material flows within the sample before and after the CWR process are compared in Figure 5.4. Initially, the green and pink plasticine layers were evenly distributed on the transverse and longitudinal sections, except for the pink layer in the centre of the longitudinal section. Its thickness nearly doubled, mainly because it was the starting point to roll the pink-green layers and form the pink-green patterns on the transverse section. Note that the initial samples for the transverse and longitudinal sections were built by two different strategies. Initially, the pink and green chunks at the same weights were cut from large slabs, respectively. Then, one pink and one green layers at a set thickness about 3 mm were manufactured by a pasty roller. After that, the two layers were piled up. Regarding the sample for the transverse section, stripes at a length of 50 mm and the variable designed widths were cut from the previous pink-green layers, and then piled up to form a cylindrical shape. However, as for the sample for the longitudinal section, the two layers were rolled together to form a cylinder until the diameter exceeds the designed diameter by one cycle. For both samples, the final forging and trimming processes were applied to achieve the designed geometry.

After rolling, on the transverse section, some regions were expanded, as indicated by the blue arrows, while other regions narrowed due to the compression during CWR, as shown by the yellow arrows. The S-shape pattern of the layers appeared in the middle of both the physical and FE

models, as indicated by the red dashed curves. The thickness of the middle pink layer was increased in the longitudinal section, especially at the sample ends, as indicated by the blue arrows, while the regions near the surface were narrowed, as the yellow arrows indicate. Central cracks are found in both views. These cracks were located in the transversal section's central region and along the longitudinal section's central line. This agrees with CWR central cracking morphologies in metals, as observed in previous studies [7, 27, 53]. It is noticed that the exterior shape on the transverse section differs slightly between the physical and FE models. This is caused by the sectioning process after the CWR. The slight difference in the exterior shape does not affect the characterisation of the cracks, as indicated by the red circles.
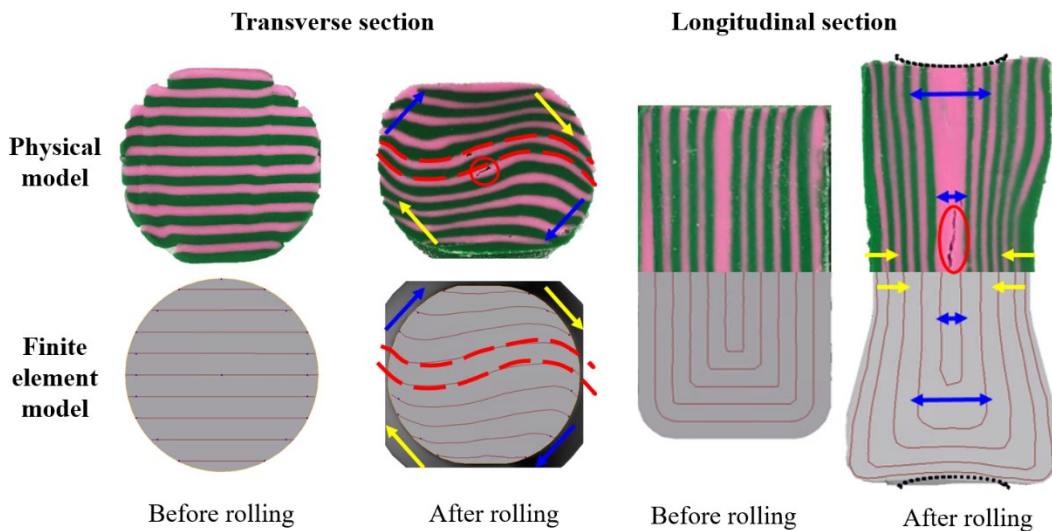
Figure 5.4 Comparison of material flows on the transverse and longitudinal sections before and after cross wedge rolling in the physical and finite element models. The red circles indicate the central cracks, with the red double dashed lines the material flows, the yellow arrows the narrowed regions and the blue arrows the expanded regions.

5.4.2 Cross wedge rolling test under various die geometries

Die description and cross wedge rolling results
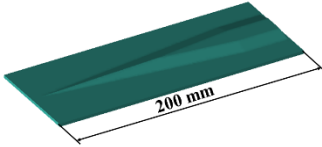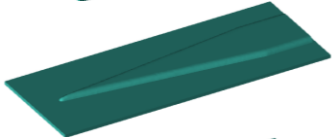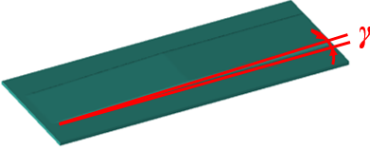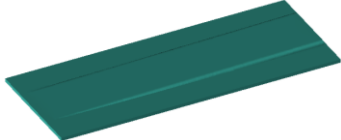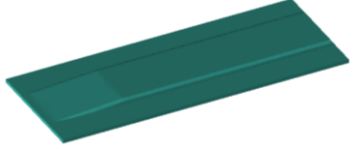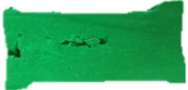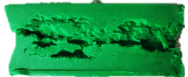
Nine pairs of CWR dies were manufactured for achieving various stress states. Table 5.3 lists the die geometry parameters and the central crack status after the corresponding CWR processes. The die geometry of the Reference case in Table 5.3 is an industrially used one. All the other cases were designed to create specific stress states within the workpiece. These stress states will differentiate the critical mechanistic factors for central crack formation and validate the fracture criterion and the new method for material constants determination.

Cases 1, 2 and 3 were designed by adjusting the forming angle or the stretching angle to the limits. The cracking severity gradually increased from Case 1 to 3, implying a significant change occurred in the value of the critical mechanistic factor, which facilitates the differentiation of the critical and non-critical factors. Case 3 was further investigated by adjusting the feeding angle, as presented in Cases 4 and 5. It is noticed that the cracking severity increased with the increasing feed angle.

The effects of cyclic loadings were clarified by comparing Cases 3 – 5. The total compressive deformation (i.e. the tool wedge height) in these three cases was kept constant, but the total cyclic number was varied. In these three cases, the dies stopped when the billet passed the highest point of the die slope to avoid the unnecessary influence of the rotation after that.

Cases 6 - 8 were simplified from Cases 3 - 5 to provide a new method to determine the material constants associated with the fracture criterion by widening the wedge. This new method requires only simple die geometry, which offers considerable convenience and cost-saving to the industry in practice.

Table 5.3 Geometrical parameters of dies for 9 cases of cross wedge rolling tests and rolled samples' longitudinal views.

Case no.	$\alpha/^o$	$\beta/^o$	$\eta/\%$	$\gamma/^o$	Die structure	Longitudinal cross-section views
Ref	15	7	44	-		
1	15	0	44	-		
2	90	7	44	-		
3	90	0	44	1.37		
4	90	0	44	0.91		
5	90	0	44	1.83		
6	90	0	44	0.91		
7	90	0	61	1.37		
8	90	0	75	1.83		

Fracture evolution

Cases 6, 7 and 8 were designed to investigate the fracture evolution and determine the material constants in the proposed fracture criterion. The damage development in Cases 6-8 is shown in Table 5.4. The damage was

monitored by conducting interrupted tests and sectioning at 25%, 50%, 64% and 100% of the whole CWR process. The damage levels were defined in Figure 3.7. The feed angle directly affected the central cracking formation. The crack would happen at the earlier stage and become more aggravated, as the feed angle was increased.

Table 5.4 Damage levels on the interrupted cross wedge rolled samples in Cases 6 to 8.

Case no.	Feed angle	25%	50%	64%	100%
6	0.91º	No crack	No crack	Void nucleation	Macro crack
7	1.37º	No crack	Macro crack	Macro crack	Fully cracked
8	1.83º	Void nucleation	Fully cracked	-	-

5.4.3 Numerical results

Stress evolutions under various die geometries

The maximum shear stress effect was distinguished by comparing the stress states in the nine cases with the cracking conditions shown in Table 5.3. Based on the detailed stress analysis of the cases Reference, Case 1 and Case 3, as shown in Figure 5.5, it is clear that the critical stress components causing central cracking are the first principal stress (σ_1) and the maximum shear stress (τ_{max}), while the axial tensile stress (σ_{xx}) is not a critical factor. The most severe cracking occurred in Case 3, where the highest principal stress (σ_1) and the highest maximum shear stress (τ_{max}) of all the three cases are found. For the axial direction (*x*-axis), as seen in Figure 5.5 (b), the stress σ_{xx} in the Reference case (no crack) is the highest. Along the *y*-axis, the highest value of σ_{yy} occurs in Case 3, implying that it could have potential effect on central cracking, which will be further examined.
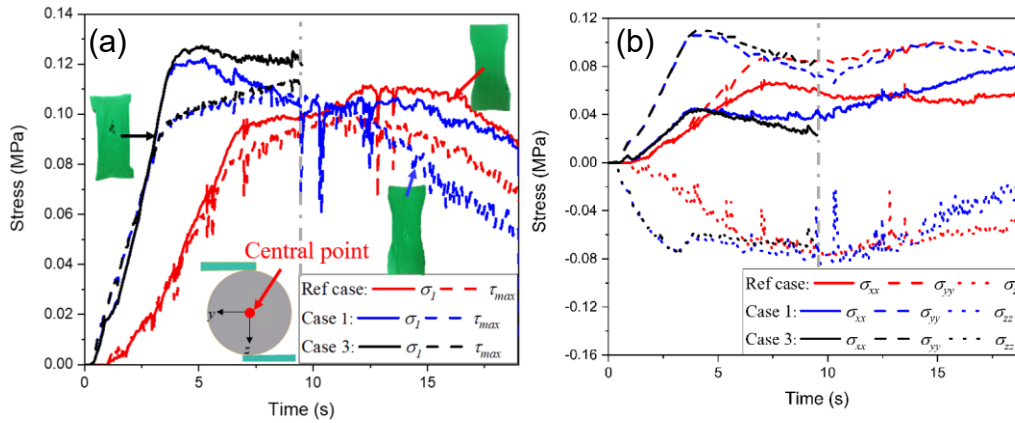
Figure 5.5 Comparison of (a) the first principal stress and the maximum shear stress and (b) stress components along x, y and z axles in Ref case and Cases 1 and 3 with experimental observations (Ref case: α=15°, β=7° and η=44%; Case 1: α=15°, β=0° and η=44%; Case 3: α=15°, β=0°, η=44% and γ=1.37°).

Cases 3-5 investigate the effects of the maximum shear stress on the central cracking further. These cases were designed to generate approximately the same level of the first principal stress but with different maximum shear stresses in the central region of the CWR samples. Case 4 with the smallest feed angle is crack-free, Cases 3 and 5 with larger feed angles show evident central cracking. Figure 5.6 compares the stress states in Cases 3 - 5 in both cartesian and cylindrical coordinate systems. The feed angle increases successively from Case 4 to 3 and 5. As seen in Figure 5.6 (a), with a similar level of the first principal stress, the crack formation trends increased with the increase in the maximum shear stress. For example, Case 5, with the largest feed angle and the largest crack, exhibited the highest maximum shear stress of the three cases, while Case 4 experienced the lowest maximum shear stress, and no central crack was found. Also, the other tensile stress components such as σ_{xx} and σ_{yy} seem to have little influence on the central cracking process, as seen in Figure 5.6 (b). The highest values of σ_{xx} and σ_{yy} are found in Case 4, where no central crack is observed. Thus, all three

stress variables, including the first principal stress σ_1, the axial stress σ_{xx} and the secondary tensile stress σ_{yy} are excluded from the critical factors.

The extremely low cyclic deformation in CWR is a unique feature of the forming process. However, its effects on central cracking are still unclear. Cases 3 - 5 were also designed to investigate the cyclic loading effect on the central cracking process. Figure 5.6(c) compares the cyclic loadings in the three cases. Figure 5.6(d) shows that P1 instead of the central point was taken to study cyclic loadings mainly because the central point could not present the reversal pattern precisely due to its singular position. Only the radial stress in the three cases is compared because it has the same pattern as the hoop stress. The cyclic loading in three cases was analysed, and the results are listed in Table 5. It is of great interest to see that in Case 5, both the effective cyclic number and the average loading amplitude are the lowest, but the cracking is the most severe. In contrast, the highest number of cycles and the maximum stress amplitude are found in crack-free case 4. This is mainly because the total compressive deformation in all three cases, Cases 3-5, was constant. In Case 5, the CWR was completed within half cycle of the workpiece rotation, leading to the high compressive stress (σ_3) in the central region, followed by the high maximum shear stress (τ_{max}). Therefore, it can be concluded that the cyclic loadings are not the critical reason for central crack formation in CWR.
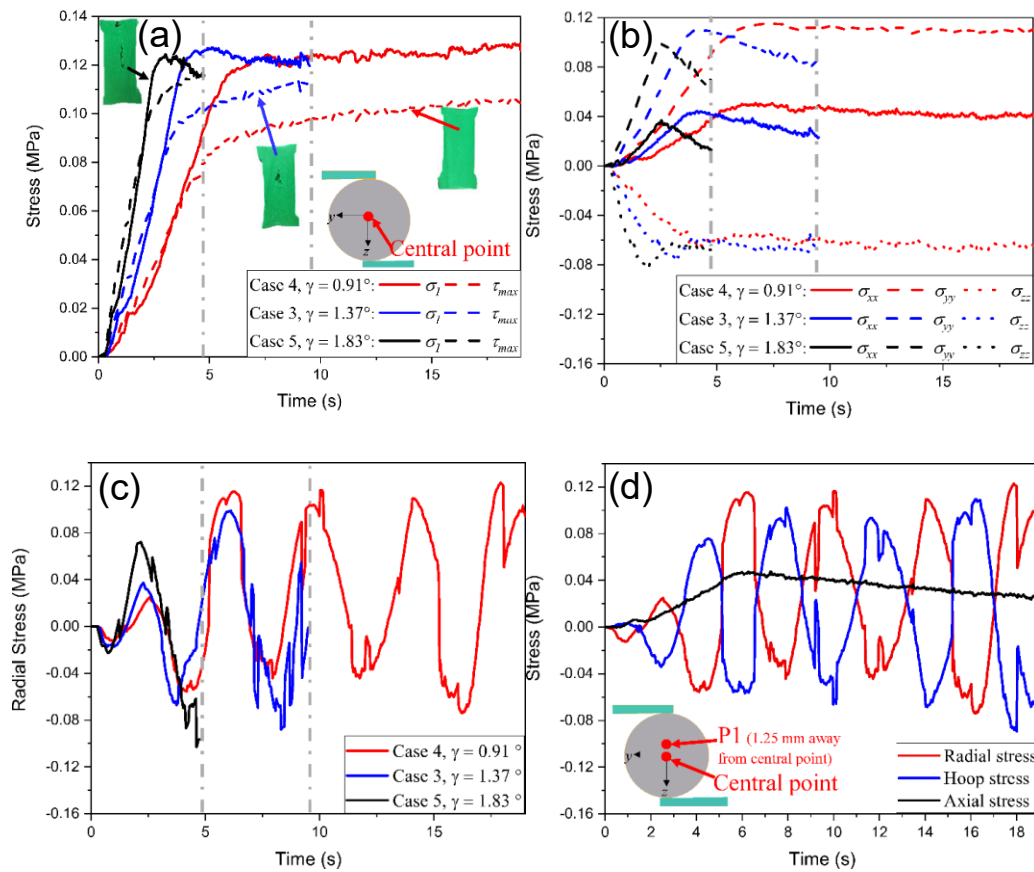
Figure 5.6 Stress components at the central point in Cases 3 - 5 in a cartesian coordinate system: (a) the first principal stress and the maximum shear stress; (b) the stress components along three axes; and at point P1 in a cylindrical coordinate system with the central point as the original point and the x-direction as cylindrical axis: (c) radial stress in three cases; (d) stress components in Case 4.

Table 5.5 Cyclic loadings at P1 in cases 3 – 5.

Case No.	4	3	5
Effective cyclic number	5	2	1
Average amplitude (MPa)	0.0735	0.0548	0.0469

The effect of the maximum shear stress is further investigated in Cases 6 - 8. Figure 5.7 presents the variation of the first principal stress and the maximum shear stress at the workpiece's central point. It is seen that the maximum

84

shear stress in Cases 7 and 8 is much higher than that in Case 6, in agreement with the experimental observation, as shown in Table 5.3. Meanwhile, the maximum shear stress at the void nucleation point, 4.75 s in Case 8, is at the same level as that in Case 6 at 12.16 s, as the solid green dots show, implying that the potential nucleation point in Case 7 is between 4.75 s and 9.5 s as the hollow green dot shows. This agrees with the experimental observation shown in Table 5.4. This finding further confirms the predominant effect of the maximum shear stress and its potential capability to predict void nucleation.

It is noticed that the first principal stress in cases 7 and 8 is reduced after reaching the maximum value. It is mainly because there is less or no axial extension deformation in these two cases, due to the elimination of the forming angle. Without the axial extension deformation, the material is mainly subjected to the radial compression. This leads to the reduced first principal stress, increased third principal stress and increased maximum shear stress. This phenomenon matches the trend in many other cases such as Cases 1 and 3 (in Figure 5.5 (a)) and Case 5 (in Figure 5.6 (a)). The forming angle in all these cases was removed.
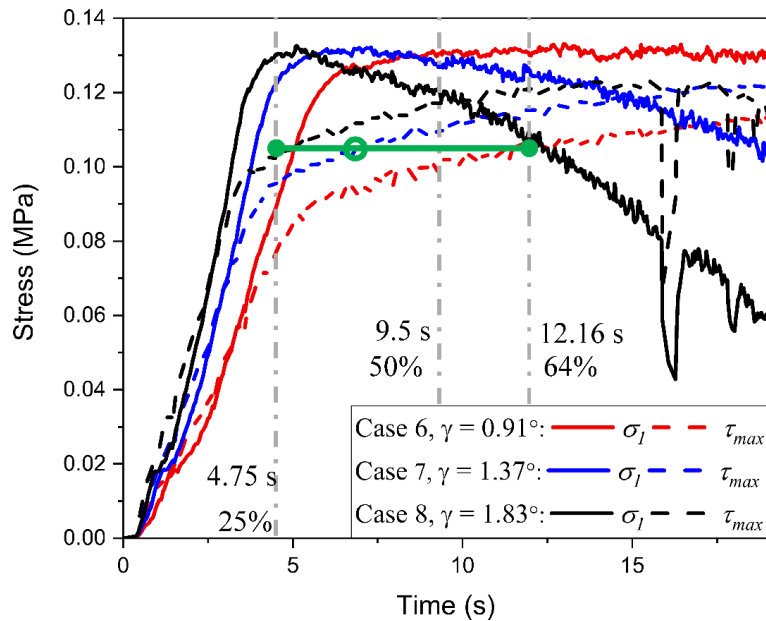
Figure 5.7 The first principal stress and the maximum shear stress at the central point in Cases 6 – 8 with solid green dots showing the void nucleation points and the hollowed one showing the potential void nucleation moment.

Material flow, stress and damage analysis

A more detailed investigation on Case 6 was undertaken to demonstrate the material flow, stress and predicted damage evolution over the fracture process, from the no damage stage to void formation and then to the macro crack, as shown in Figure 5.8. According to Table 5.4, it is known that the void formation in Case 6 occurred at 64% of the whole CWR process, and the macro crack was observed at the end.

Figure 5.8 (a) and (b) presents the material flows in the radial and hoop directions on the transverse cross-section. Along the radial direction, materials under the dies are flowing into the central region, while the material outside the compressive zone between the dies is squeezed to the surface, leaving the central point a singular point. With the deformation increase, the billet ovality is increased, causing the high radial velocity of the material outside the compressive zone. Along the hoop direction in Figure 5.8 (b), the

velocity increases from 0 at the centre to about 10 mm/s on the surface due to the billet self-rotation. A slight distortion is noticed in the areas near the die resulting from the strong tangential stress applied by the dies.

For the stress components in Figure 5.8 (c) to (e), none of them demonstrates a considerable change in values except for the shear stress on the cross-section (τ_{RH}), consistent with the no damage-void nucleation-macro crack trend observed in experiments. Consistent with the radial velocity, the radial stress of materials under the dies is negative, but it is interesting to notice the positive radial stress (the red region in Figure 5.8 (c)) is located around the central point, implying the centre is subject to strong tension. The hoop stress experiences a similar phenomenon that the high and positive stress is located around the central point and just normal to the red pattern for the radial stress. This jointed effect contributed to the high first principal stress in the central region, as shown in Figure 5.8 (f). In addition, strong shear bands are noticed on the cross-section, meanwhile, with the workpiece rotation, the value gets higher, and the bands get wider, which agrees with the non-crack, void nucleation and macro crack trend. The predominant effect of shear stress was demonstrated. The first principal stress distribution is shown in Figure 5.8 (f). The highest value occurs in the central region, corresponding to the central cracking location; however, there is no visible difference in the value between the three specific moments, indicating its incapability to predict fracture formation. Although the maximum shear stress shares the same trend with the cracking evolution, its highest value is located around the dies, making it insufficient to describe the cracking location. However, the first principal stress enables to guarantee the fracture location. With the combined consideration of the maximum shear stress and the first principal stress by applying the proposed fracture criterion in Equation 5.1, the predicted damage evolution well matches the cracking evolution as presented in Figure 5.8 (i), i.e. no damage at 50% CWR, void nucleation at 64% and macro crack

at the end of the CWR. Note that the lower limit of the colour bar is the critical damage value.

Comparing the stress/damage evolution with the experimental cracking evolution demonstrates the essential role of both the maximum shear stress and the principal first stress in accurately predicting the central cracking location and moment.

Time percentage of the whole CWR	50%	64%	100%
Cracking condition	No damage	Void nucleation	Macro crack
(a) Radial velocity v_R (m/s)			
(b) Hoop velocity v_H (m/s)			
(c) Radial stress σ_R (MPa)			

(d) Hoop stress σ_H (MPa)	
(e) Shear stress τ_{RH} (MPa)	
(f) The first principal stress σ_1 (MPa)	
(g) The third principal stress σ_3 (MPa)	
(h) The maximum shear stress τ_{max} (MPa)	

89

(i) Predicted damage *D* (MPa)

| 0.1320 | 0.1335 | 0.1350 | 0.1365 | 0.1380 | 0.1395 |

Figure 5.8 Material flow, stress and damage distribution on the transversal cross-section in Case 6 at three specific stages: no damage, void formation and macro crack.

5.5 Discussion

5.5.1 Determination of critical mechanistic factors for central crack formation

The essential roles of the maximum shear stress and the first principal stress in forming central cracks are identified based on the above comparison and analysis of the simulated and experimental results under various die geometries. The axial tensile stress, the secondary tensile stress and the low cyclic fatigue are not considered as critical due to their opposite trends against the experimental observation.

These non-critical stress variables play different roles in central crack formation. As investigated in literature [46], the cyclic loadings resulting from the workpiece's rotation accelerated the accumulation of the shear stress in the central region. Without the workpiece rotation (or cyclic loadings), the fracture is more likely to occur on the surface. The value of the axial tensile stress (σ_{xx}) is relatively low in this study compared with the other stress variables along *y* and *z* directions, probably because of the low stretching angle *β*. However, with the increasing stretching angle, the axial tensile stress

90

would be increased, resulting in the first principal stress shifting to the axial direction. Then the significance of the axial tensile stress would be evident. The secondary tensile stress (σ_{yy}) is generated by the compressive stress (σ_{zz}) applied by the dies, which contributes to the increase of the first principal stress and then the maximum shear stress.

5.5.2 Determination and validation of material constants

Different cracking levels were defined through three groups of interrupted CWR tests, as shown in Table 5.4. All ten situations were taken into account to achieve high accuracy of the material constants defined in Equation 6.2. The material constant value *C* was calculated to be 0.22, and the critical damage value was calculated to be 0.1319 MPa by determining the average value of the minimum damage value for the void formation cases and the highest damage value for the non-cracked cases. Figure 5.9 shows the damage value in cases 6 - 8 at various moments, as presented in Table 5.4. The *x*-axis presents the situation number, 1 to 10, while the *y*-axis shows the predicted damage value at each situation. The critical line, marked as the dashed red line in the figure, clearly differentiates the cracked and non-cracked cases. The void nucleation cases are presented in blue triangles, located just above the critical line.

Furthermore, the damage value was calculated in all the other six cases in Table 5.3, as shown in Figure 5.10. The damage value matches the experimental crack condition well. The red dots represent the experimentally cracked cases, all of which are located above the red critical damage line, while all the green squares are below the critical damage line. The damage value of case 1 is close to the critical line, agreeing with the minor cracks observed in Table 5.3. This demonstrates the high effectiveness of the new material constant determination approach and the robustness of the proposed fracture criterion for predicting central crack formation.
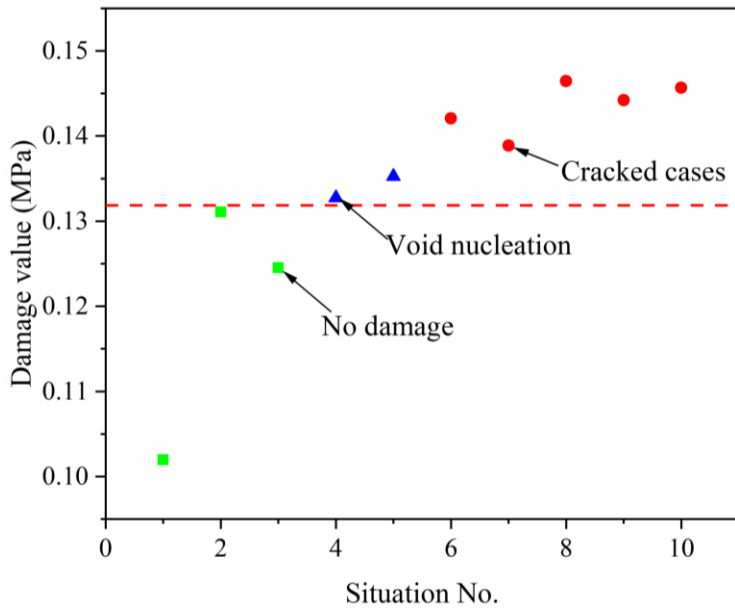
Figure 5.9 Damage value at the ten situations (including the 25%, 50%, 64% and 100% cross wedge rolling moments in Cases 6 - 8 given in Table 5.4) with the critical damage line (the red dashed line).
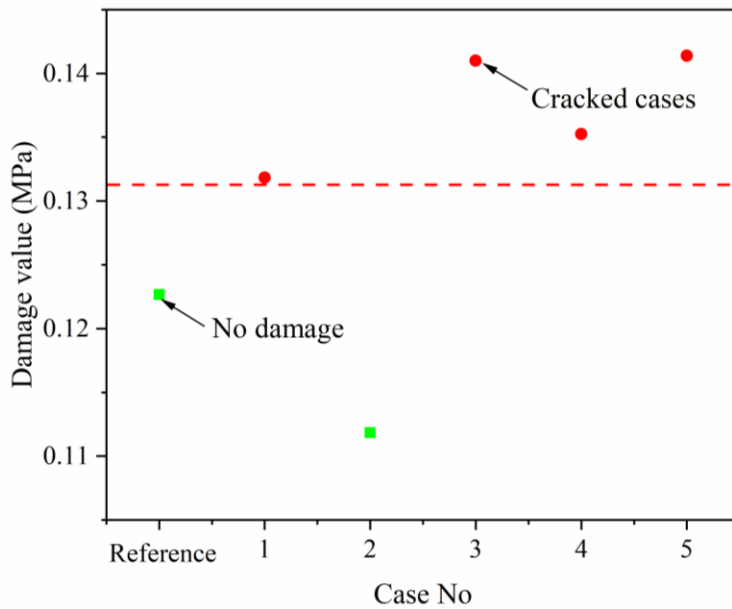
Figure 5.10 Comparison of the damage value in Ref case and Cases 1 - 5 with the critical damage value.

5.5.3 Fracture mechanism

The proposed model's reliability was further demonstrated through the achieved high consistency of central crack formed in the FE model, plasticine and pure aluminium, as shown in Figure 5.11. It can be seen that in all three cases, the greatest damage occurs in the central region of the transversal section and distributes along the axial direction. Both the plasticine and pure aluminium billets present the same fracture features, i.e. cross-shape cracks in the central region and voids ahead of the cracking tips, which agree with the central crack features in C45 steel [27, 31].

It is understood from Figure 5.8 that the highest first principal stress (σ_1) occurs in the central region of the billet transversal cross-section during the CWR. Due to the increasing compressive stress (σ_3) generated by the die compression, the maximum shear stress (τ_{max}) under the dies increases, as shown in the FE model of Figure 5.11. Both the first principal stress and the maximum shear stress accelerate the crack formation, but to different degrees, as the proposed fracture criterion implies. With their combined effects, fracture occurs in the central region when the damage value reaches the critical damage value.

Based on the current study and previous literature [7, 27, 31], the central cracking process in CWR can be summarised as (i) the microvoids/cracks form around the initial defects by interface decohesion driven by the maximum shear stress and the first principal stress; (ii) with the increase of the maximum shear stress and the first principal stress, the voids are severely distorted and enlarged. The shear stress sharpens the void ends/cracking tips, causing high stress concentration, while the first principal stress enlarges the voids or opens the cracking tips. Both of them accelerate the coalescence and propagation of voids/cracks, followed by the macrocrack forms on the transversal cross-section; (iii) the rotation of the workpiece

facilitates the secondary cracks form perpendicularly or roughly perpendicularly to the first cracking path due to the central symmetrical feature, generating the cross-shape morphology on the transversal cross-section. Meanwhile, with the increase of damage value along the axial direction and the sharpening of cracking tips, the cracks propagate along the axial direction quickly, forming the longitudinal cracking as shown in Figure 5.11.
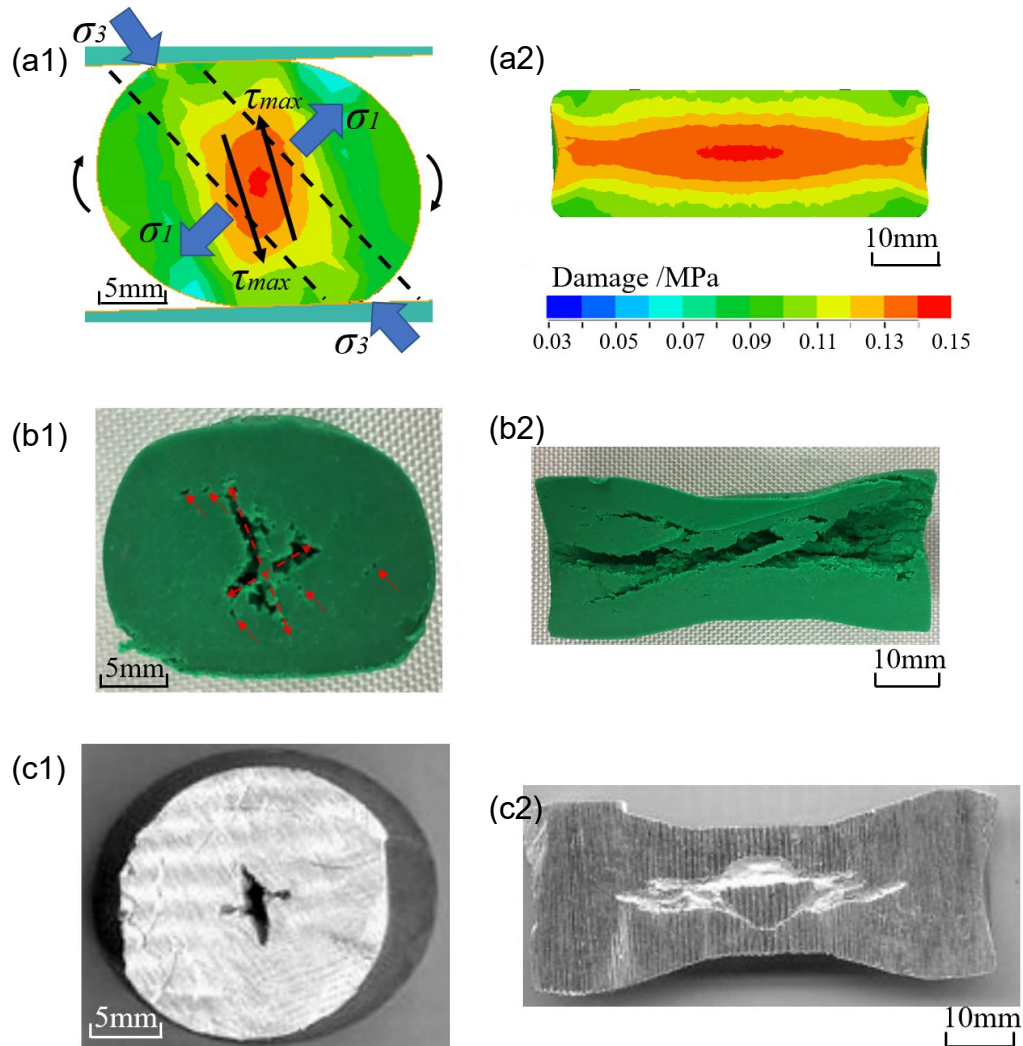
Figure 5.11 Comparison of central cracks on (1) transverse and (2) longitudinal views (a)predicted by the FE model, (b) observed in plasticine/flour composites, and (c) pure aluminium [53]**.**

5.6 Conclusions

The effects of individual stress components, cyclic loading, and central cracking mechanism in CWR were clarified using a modelling material, plasticine. The plasticine was cross wedge rolled using a range of shaped

dies. These CWR dies were 3D printed. A lab-scale CWR prototype was developed such that it could generate the specific stress states found during CWR. An FE model of the CWR process was also developed. The FE CWR models were used to reveal the distribution and evolution of stress components. The following conclusions can be drawn:

(1) The individual effects of the potential mechanistic factors on central cracking were systematically analysed and compared experimentally and numerically. The dominant effect of the maximum shear stress was verified. The integration of the maximum shear stress with the first principal stress is essential for the accurate prediction of central crack formation. The effects of the low cycle fatigue, axial tensile stress and secondary tensile stress are less significant.

(2) The fracture mechanisms of central cracking involve the void formation and shear decohesion. This experimental finding enhances the analytical finding in the literature.

(3) A novel method for determining the material constants used in the previously proposed criterion is established. The method involves a small number of interrupted CWR tests and FE process simulation. Only one pair of inclined CWR plates is required, resulting in greater efficiency and convenience in both research and industrial applications. The high accuracy of this technique was demonstrated by six groups of CWR tests. The novelty in this new method is also suitable for the investigations of other complex manufacturing processes.

Chapter 6 A unified central crack criterion for industrial application

6.1 Introduction

The previously proposed fracture mechanisms and fracture criterion show high accuracy when applied in low ductility materials, such as the pure aluminium (highly strained) and plasticine/flour composite at the room temperature. It is known that the materials show different fracture mechanisms based on ductility levels, implying the incapability of the previously proposed fracture criterion when applied in high ductility materials, such as C45 steel at the elevated temperature. This chapter focuses on developing a unified physically-based central crack damage model for materials with various values of ductility, including pure aluminium at the room temperature and steels at the elevated temperature.

The methodology, including the experiments, FE model and the involved existing damage models, is described in Section 6.2, followed by introducing a new damage model set. Multiple central crack mechanisms were considered in this new model. The experimental and simulated results are listed in Section 6.4, where the high accuracy of this new model was validated by 60 groups of experimental data with different materials and compared with the other 10 existing damage models. The underlying multiple fracture mechanism and the advance and significance of the proposed damage model set are discussed in Section 6.5.

6.2 Methodology

The lab-scale CWR physical model, as described in Section 3.2.3, was applied for this study. Plasticines with various flour weight ratios were applied to experimentally reveal the multiple fracture mechanisms for materials with different ductility. The proposed damage model was validated with various die geometries. The corresponding CWR FE models were established to track the stress/strain and damage distribution and evolution. The proposed damage model was compared with 9 representative existing damage models in the robustness of predicting central cracking. In total, 60 groups of CWR data were referred to validate the 11 damage models, including the 12 groups of CWR tests in industrial conditions, i.e. steels at high temperature.

6.2.1 Cross wedge rolling tests

Pure plasticine was applied for the validation of the proposed damage model for high ductility materials. The plasticine & flour composites with various weight ratio were employed for investigating the multiple fracture mechanisms. Figure 6.1(a) shows the engineering stress-strain curves of the plasticine with various flour weight ratios. In general, the increase of the flour content correlates with the reduction of the ductility or the increase of the yield/ultimate strength of the composite materials. The existing scattering could be attributed to some remaining flour particle agglomerates. However, to control the content of these flour agglomerates, cares were taken in preparation by mixing the plasticine and flour thoroughly in the grinder, followed by the hammering and folding for over ten times. The Figure 6.1 (b) presents the true stress-strain curves of pure plasticine at different strain rates, showing the material yield strengths rise with an increase in strain rate.
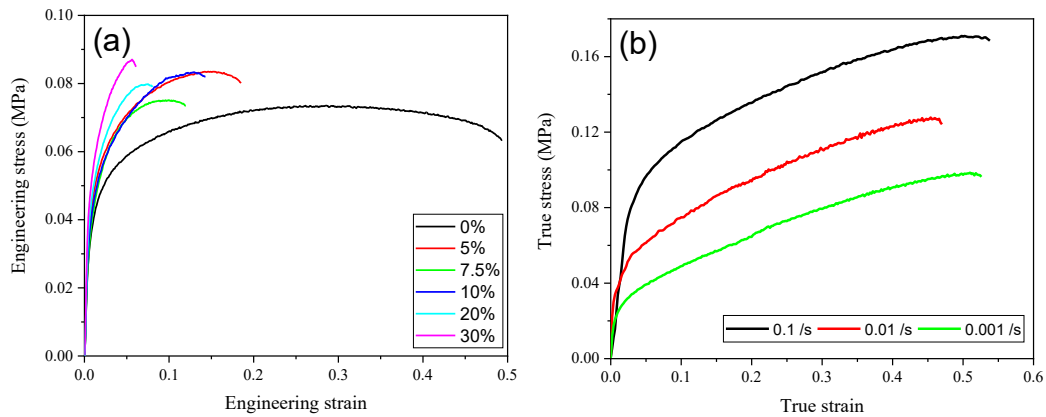
Figure 6.1 (a) Engineering stress-strain curves of plasticine with different flour weight ratios (strain rate 0.5/s); (b) true strain-stress curves of pure plasticine at different strain rates.

The die geometries used to examine the fracture criterion are listed in Table 6.1. The simplified dies in Cases 7-9 could be applied to calibrate the material constants, with the rest two cases adopted to validate the accuracy of the proposed damage criterion.

Table 6.1 Geometrical parameters of dies for cross wedge rolling tests

Case no.	α/º	β/º	η/%	γ/º
Reference	15	7	44	-
6	90	0	44	0.91
7	90	0	61	1.37
8	90	0	75	1.83
9	90	0	94	2.74

6.2.2 Experimental cross wedge rolling data for C45 steel

Two groups of CWR tests in various conditions were summarised in Table 6.2 with respect to process parameters, workpiece, die geometry, and crack condition in the rolled product. Note that in Yang's research, the dies were on rollers, while in Pater's research, the dies were on plates. Meanwhile, in Yang's research, the initial diameter keeps constant at 40 mm, while Pater

keeps the final diameter consistent at 22 mm. The difference in the temperature and rolling speed between the two groups of tests is in a narrow range. The cracking results of Pater's research of Case S8-10 are consistent with Yang's results in Case S1-3, i.e. the status of rolled workpiece changes from crack-free to cracking with the increase of area reduction ratio. Each group of data includes cracked and non-cracked cases.

Table 6.2 Experimental data of cross wedge rolling test for C45 steel

Ref	Case No	Temperature/°C	Rolling speed/ mm/s	Initial billet diameter/ mm	Die geometry			Cracking condition
					$\alpha(°)$	$\beta(°)$	$\eta(\%)$	
Yang et al. [27]	S1	1100	396	40	15	10	35.00	No crack
	S2				15	10	55.00	Cracked
	S3				15	10	75.00	Cracked
	S4				15	5	75.00	Cracked
	S5				15	7.5	75.00	Cracked
	S6				20	10	75.00	Cracked
	S7				25	10	75.00	No crack
Pater et al. [7]	S8	1150	300	26	15	10	28.40	No crack
	S9			33	15	10	55.60	Cracked
	S10			40	15	10	69.70	Cracked
	S11	1050		33	15	10	55.60	Cracked
	S12	1100		33	15	10	55.60	Cracked

6.2.3 Finite element model

The establishment of the FE CWR model is described in Section 3.4. The FE model configuration is presented in Figure 5.2. To build the material database for the pure plasticine billet, the stress-strain curves in Figure 6.1(b) was input to QForm. The density of the pure plasticine was set to be 1868 kg/m^3 by experimental measurement. The Young's modulus was calculated to be 2.6 MPa based on the stress/strain curves, while the Poisson's ratio was set to be 0.4 based on the data in the literature [132, 133, 135]. Coulomb friction model with a friction coefficient of 0.9 is applied.

6.2.4 Damage models

Ten existing damage models were examined by comparing the predicted damage value with the experimental cracking condition, including four classic fracture criteria/damage models, two recently proposed ones and four damage models for shear dominant ductile fracture. The first four classical damage models, including the maximum plastic strain criterion, C&L model (Equation 2.2), Oyane model (Equation 2.5) and R&T model (Equation 2.7), are widely used in literature to predict the central cracking in CWR due to the simplicity. The two recently proposed ones, including the one proposed by Pater et al. [7] (in Equation 2.11) and the one proposed in Chapter 4 (in Equation 4.1), have been quantitatively validated by C45 steels at elevated temperature and pure aluminium at room temperature, respectively. The last four damage models, including Zhu's model [74], Smith' model [75], MMC model [76] and X&W model [66] (in Equation 2.14- Equation 2.17), take the shear effect into account, implying high potentials to predict the central crack accurately. All these models were quantitatively validated in this study.

6.3 New central crack damage model set

6.3.1 Central crack predictive model for ductile materials

An energy-based damage model is proposed as presented in Equation 6.2, aiming to predict central cracking in high ductility materials such as C45 steel at high temperature (~1050 °C) when severe plastic deformation occurs before final fracture. It is defined that central cracking takes place when the damage value D exceeds the critical damage value D_c. The dominant effect of plastic strain in ductile fracture has been soundly understood [66, 136]. However, in the complex stress states such as in the CWR, the plastic strain is insufficient to predict fracture occurrence, as proved in Chapter 4. Thus, the stress states are introduced to describe the fracture behaviours

accurately. In CWR, the central crack mechanisms include shear fracture and void formation. The shear fracture is represented by the first part $\int_0^{\overline{\varepsilon_p}} \tau_m \, d\overline{\varepsilon_p}$ in Equation 6.2. The significant effect of the maximum shear stress to central cracking has been investigated in Chapter 5. The void formation is represented by the second part, $\int_0^{\overline{\varepsilon_p}} \sigma_m \, d\overline{\varepsilon_p}$. Here the mean stress but not the first principal stress is considered, mainly because the hydrostatic stress is more reasonable to describe the void formation such as in R&T model [69] and Oyane model [61]. A linear relationship between these two mechanisms is defined by a coefficient *C* to describe their interactive effects on accumulated damage. Both the critical damage value D_c and the coefficient *C* depend on material properties, which can be tested by CWR tests with simplified dies, as presented in Figure 2.1.

$$D = \int_0^{\overline{\varepsilon_p}} (\tau_m + C\sigma_m) \, d\overline{\varepsilon_p} \quad \begin{cases} < D_c, \text{No crack} \\ \geq D_c, \text{Cracked} \end{cases} \quad \text{Equation 6.1}$$

6.3.2 Establishment of a damage model set

The central cracking damage model set for ductile and brittle materials can be written as Equation 6.2. The selection of damage models is decided by the material property, fracture strain, ε_f. When the fracture strain ε_f is lower than the critical fracture strain ε'_f, the stress-based fracture criterion would be applied; otherwise, the energy-based damage model should be used. The value of the critical fracture strain ε'_f could be defined by conducting uniaxial tensile tests. For example, in Figure 6.1 (a), the plastic deformation before the final fracture is not significant except in the case of pure plasticine. Therefore, the critical value could be defined as 20% when the flour weight ratio is 5%.

$$D = \begin{cases} A\,\tau_m + B\sigma_1 & \varepsilon_f < \varepsilon'_f, \text{ low ductility} \\ \displaystyle\int_0^{\bar{\varepsilon}} (\tau_m + C\sigma_m)\, d\bar{\varepsilon}_p & \varepsilon_f \geq \varepsilon'_f, \text{ high ductility} \end{cases}$$ Equation 6.2

6.4 Results

6.4.1 Multiple central crack mechanisms with various ductility

In plasticine/flour composites

Figure 6.2 indicates that the material ductility varies with the plasticine-flour weight ratio. The longitudinal sections of the rolled samples made by the corresponding materials are also presented. The general trend is that the ductility reduces as the flour weight ratio increases. The sectioned samples demonstrate the transition of the central crack mechanism. At the flour ratio of 5%, only one dominant axial crack appears within the material, as shown in Figure 6.2(a). Then, with the increase of the flour content, more cracks appear (in Figure 6.2(b)). In the end, when the flour ratio reaches 20%, many minor cracks scatter on the whole surface (in Figure 6.2(c)). It is reasonable to attribute it to different ductility. In Figure 6.2 (a), the material is ductile (ε_f=18.5%**)** and capable to bear high plastic deformation before final fracture; thus, the fracture only occurs in the central region but not on the subsurface or at the sample ends. In Figure 6.2(c), when the material is brittle (ε_f=8%**)** with limited capacity for plastic deformation, minor cracks scatter across the whole cross section, consistent with the feature of brittle fracture.
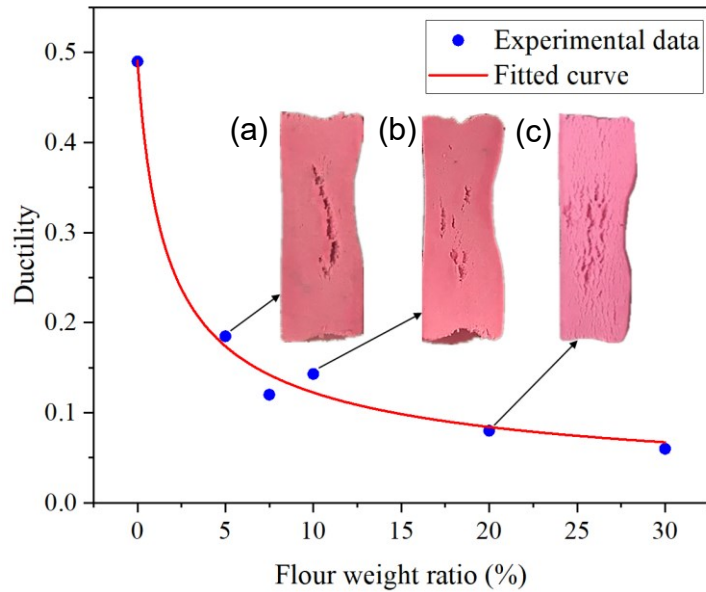
Figure 6.2 The variety of material ductility over the plasticine & flour weight ratios, along with the longitudinal sections of three selected rolled samples in (a), (b), and (c).

In pure aluminium and hot steels

The multiple fracture mechanisms found in plasticine/flour composites, that is, transferring from brittle to ductile fracture with the ductility increase, also apply to metals. As shown in Figure 6.3 (a), multiple axial cracking bands were observed in the pure aluminium AA1100 H16 during CWR, which was attributed to the low ductility (~8%) [4], while the limited axial longitudinal cracks were found in the investigations of Yang et al. [27] and Pater et al. [116] on the C45 steels due to the ductile fracture nature (~39%) [137] as seen in Figure 6.3 (b).
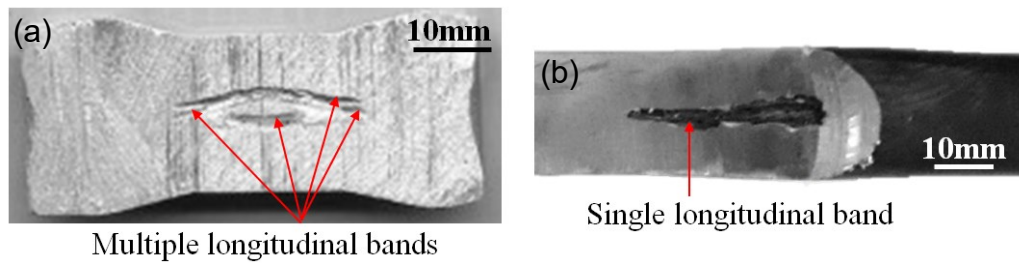
Figure 6.3 Comparison of fracture morphologies of cross wedge rolled samples on (a)pure aluminium H16 [31] **and (b) C45 steel** [116]**.**

6.4.2 Fracture criterion

Cross wedge rolling tests with plasticine under various die geometries

The crack conditions of plasticine samples in Table 6.1 were examined for the damage model validation. Figure 6.4 presents the crack-free and cracked rolled samples. Figure 6.4 (a) shows no voids/cracks on the sectioned surfaces, while in Figure 6.4 (b), evident central cracks appear on both the longitudinal and transverse sections. The cracks, located in the central region along the axial direction, are consistent with the crack in hot steels [7]. For all the cases in Table 6.1, central cracking only occurred in Case 8, mainly because of pure plasticine's high ductility and the narrow forming window for central crack formation.
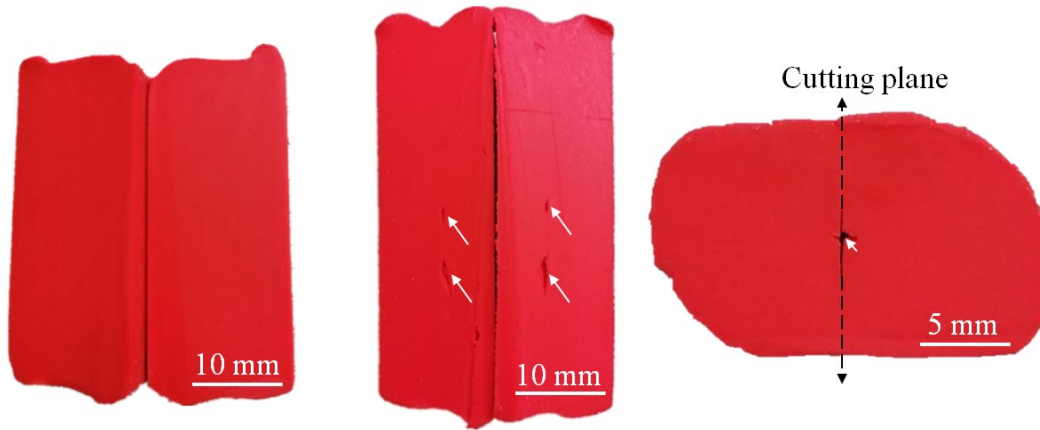
Figure 6.4 Crack conditions in the rolled samples after cross wedge rolling: (a) crack-free (Case 7 in Table 6.1) and (b) cracked (Case 8 in Table 6.1) on (b1) longitudinal section and (b2) transverse section (the white arrows indicate the central cracks and the dashed black arrows show the cutting plane).

Validation of the proposed fracture criterion by various ductility

Figure 6.5 compares the normalised damage value ($D_n = D/D_c$) on two plasticine materials in 21 CWR cases to validate the robustness of the proposed central crack in various materials. The first 16 cases for low ductility were obtained from Table 5.3 and Table 5.4, presented by green symbols and labelled as P1 – P16 in Figure 6.5. The ductility of the applied plasticine/flour composite was 12%. The proposed fracture criterion for low ductility materials was applied for the damage prediction.

The last five cases P17 – P21 correspond to the Ref case and cases 6-9 in Table 6.1. The proposed fracture criterion for high ductility was applied due to the high ductility of the pure plasticine, ~ 50%. Cases 7 - 9 were conducted to determine the associated material constants, with the rest two cases for validation. The value C and the critical damage value were calculated to be 1 and 1.07 MPa, respectively. The predicted damage values in the Ref case and Case 6 were calculated to be lower than the critical value 1.07 MPa, which matched the experimental observations that no cracking occurred in

106

these two cases. Note that the cut-off value of triaxiality at -0.33 is applied. When the triaxiality is less than -0.33, it is assumed that fracture would not happen [50, 67].

The normalised damage values in all the cracked cases are scattered above the critical line y=1, while the values of all the non-cracked cases are all below the critical line, implying the high accuracy of the proposed fracture criterion in predicting central cracks for both high and low ductility materials.
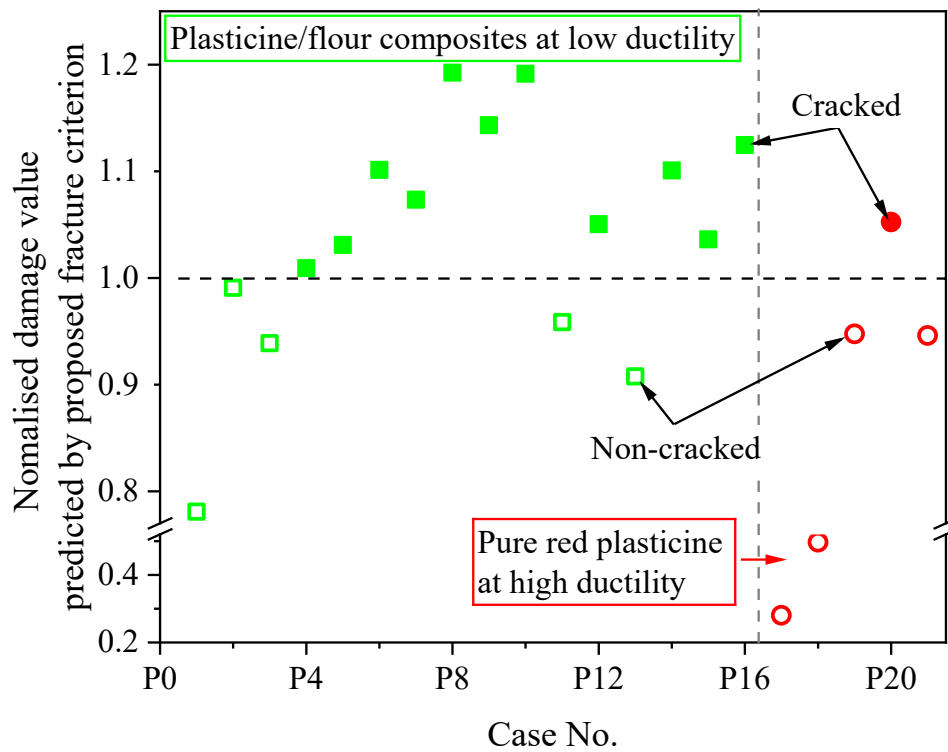
Figure 6.5 Normalised damage value on plasticine with different ductile levels predicted by the proposed fracture criterion (the hollowed symbols present the crack-free cases, while the solid cases present the cracked cases; the green cases present the cases conducted with low ductility material, with the red ones for high ductility materials).

Examination of 11 damage models by hot C45 steels

Figure 6.6 summarises the damage values at the sample central point in 12 CWR cases predicted by 11 damage models/fracture criterion. The 12 CWR experimental cases refer to the 12 C45 steel cases listed in Table 6.2, and the 11 damage models include the 10 described in Section 6.2.4 and the newly proposed one in Equation 6.1. In Figure 6.6, the horizontal axis presents the 11 damage models, and the vertical axis presents the normalised damage value, calculated by dividing the damage value acquired from the FE model by a constant, enabling the normalised value ranging from 0 to 1. The normalised damage values from 11 damage models are presented in 11 columns. There are 12 symbols in each column, 9 solid and 3 hollow ones, corresponding to the 9 cracked cases and 3 non-cracked cases in Table 6.2. It is expected that with the robust fracture criterion, the predicted damage value in all the cracked cases would be higher than the damage value in the non-cracked cases. From Figure 6.6, only the proposed model for high ductility and Zhu's model can distinguish the solid symbols from the hollow ones; namely, all the solid symbols are above all the hollow ones. Under all the other models, however, the solid and hollow symbols are mixed. It indicates the high accuracy of these two models in predicting central cracking in C45 steels. Further investigations were conducted below to explore the underlying reasons.
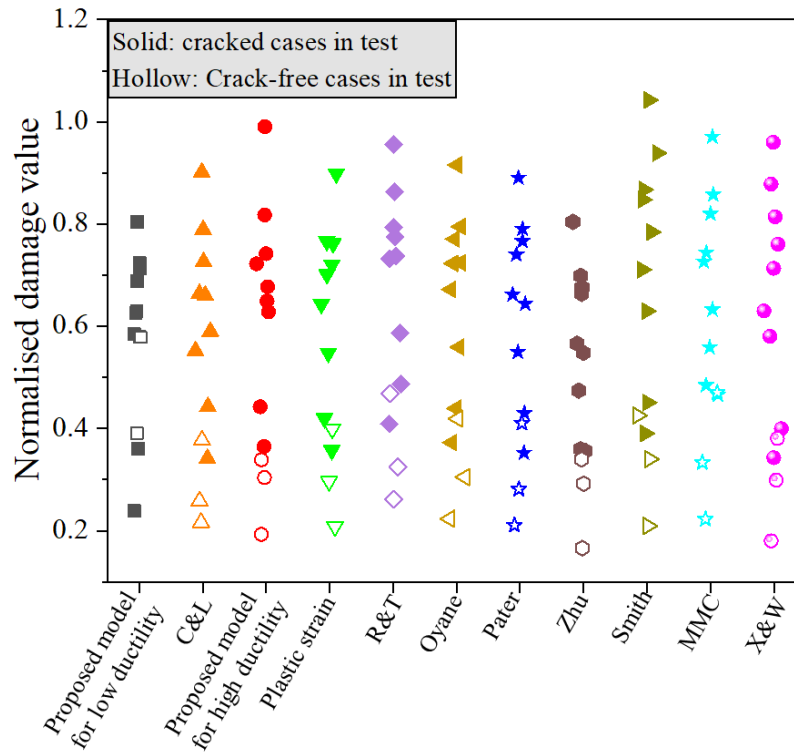
Figure 6.6 Normalised damage values of the central point at the end of 12 C45 CWR cases predicted by 11 damage models (each column contains 3 hollow symbols and 9 solid symbols, representing 3 crack-free cases and 9 cracked cases observed in experiments).

The same pattern can be seen in other models (except for the proposed model for lowly ductility) that the two hollow symbols are at the lowest of each column, followed by a solid one above them and then the third hollow one, leaving all the other solid symbols above. Four damage models, namely, the proposed model for high ductility, Pater's model, the maximum plastic strain criterion and X&W model, are taken as examples for closer examinations, as shown in Figure 6.7. The horizontal axis presents the 12 C45 steel cases listed in Table 6.2. For all the four damage models, the highest damage value for the non-cracked cases was predicted to occur in Case S8, and the lowest value for the cracked cases was predicted in Case S6. Only in the proposed damage model, the damage value in Case S6 was higher than that in Case

S8, agreeing with the experiment that central crack occurred in Case S6 but not S8. Another similar trend was noticed in the four models; that is, the damage value increases or decreases with the plastic strain variation. It implies the significance of plastic strain in predicting central crack formation. The slight difference between the trends under the damage models indicated the stress states' importance on damage evolution.

The material constant C in the proposed damage model is set as 0 in predicting the central cracks in C45 steel, mainly because it is a shear dominated fracture and the contribution of the mean stress or the void growth trend is not significant in this case.
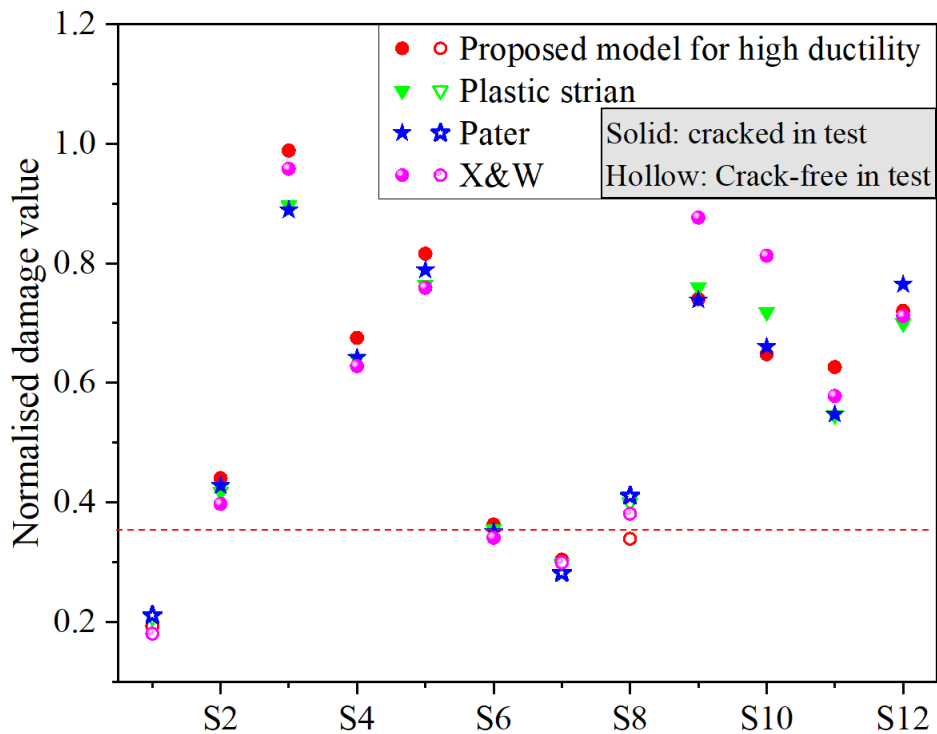
Figure 6.7 Damage value distribution of the central point at the end of CWR cases listed in Table 6.2 predicted by 4 damage models.

Figure 6.8 compares the stress/strain and damage evolution in Case S6 (cracked) and S8 (crack-free), which clearly demonstrates how the stress

state influences the cracking behaviours in a high ductility material. In both cases, the stress variables (the maximum shear stress and the mean stress) increased at the early stage at around 0.5 s, but the stress values in Case S6 increased quickly and reached a much higher value. Similarly, the plastic strain increased quickly in a short time. Although the final equivalent plastic strain in Case S6 is less than that in Case S8, it does not affect the higher accumulated damage value in Case S6.

Thus, the equivalent plastic strain can generally control the damage variation trend, but to get more accurate predictive results in complex situations such as in CWR, the stress variables must be considered.
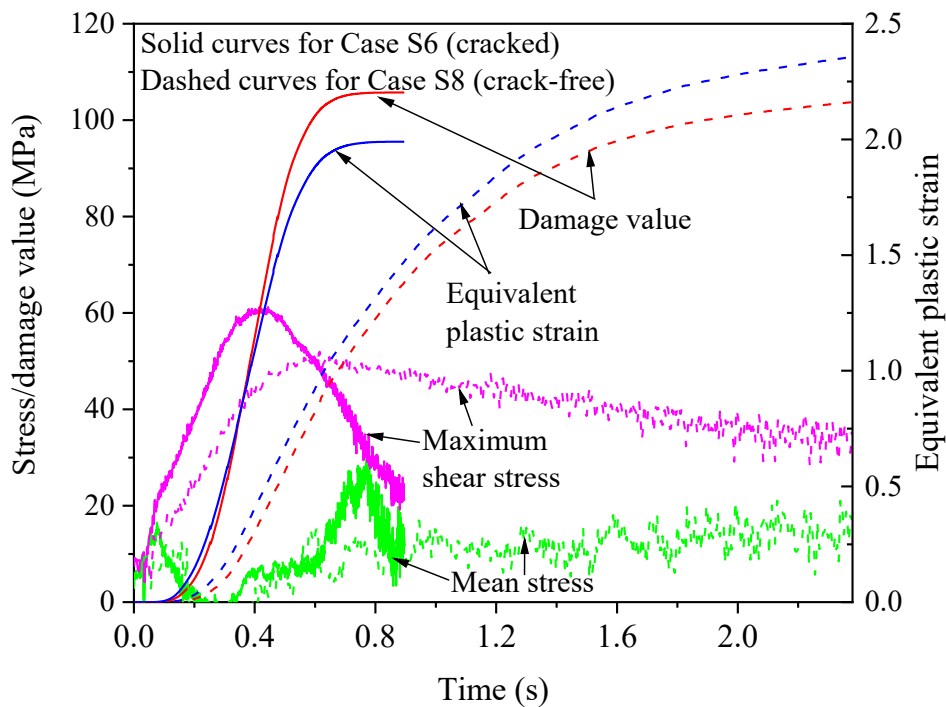
Figure 6.8 Comparison of cracked and non-cracked cases in stress/strain and damage evolution.

Material ductility effects on damage model selection

Each damage model in the damage model set is essential for the high robustness of central crack prediction in multiple materials. Using low ductility damage model for high ductility materials has been proved to be incompatible, as shown in Figure 6.6, whereas the high ductility damage model is inapplicable to predict the central cracking in low ductility materials, the green plasticine with flour (ductility 12%) and the pure aluminium AA1100 H16 (ductility around 8%), as demonstrated in Figure 6.9. Neither groups of cracked nor non-cracked cases could be distinguished by a critical value in both cases due to the different fracture natures in materials with various ductility, as discussed in the previous section.
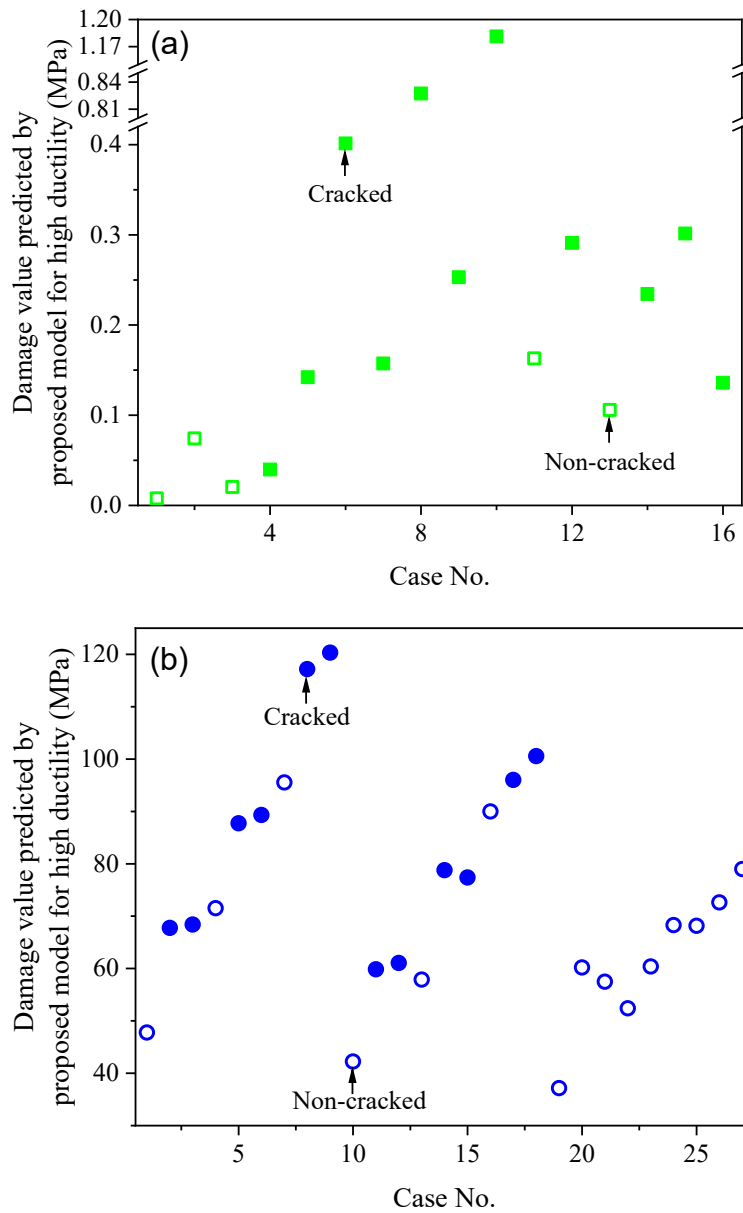
Figure 6.9 Damage value on the low ductility material predicted by the damage model for high ductility (a) green plasticine with flour; (b) Pure Al AA1100 H16.

6.5 Discussion

6.5.1 Multiple central crack mechanisms

The multiple central crack modes under different material ductility were observed in Figure 6.2 and Figure 6.3. In the low ductility materials such as pure aluminium (highly strained), the micro-cracks initiate around the initial defects such as inclusions. With the increase of the maximum shear stress and the first principal stress, the micro-cracks propagate quickly due to the relatively brittle fracture nature, leaving limited time to form voids due to the limited plastic deformation. The limited plastic deformation also facilitates intensive stress concentration, resulting in multiple crack propagations [131]. However, in high ductility materials such as hot C45 steels, microvoids/cracks form under severe plastic deformation. The increasing maximum shear stress distorts and elongates the voids and the adjacent materials and then generates intense stress concentration, accelerating the void coalescences. The mean stress accelerates the void growth, facilitating the void coalescences as well. With their combined effects, the voids grow and coalesce quickly and finally link to form macrocracks. The central crack mechanisms remain consistent with the investigations in literature [7, 27].

6.5.2 Central crack criterion

The significance of plastic strain in ductile fracture has been acknowledged and considered in many damage models. The stress states affect material fracture distinctly. The C&L model emphases the dominant effect of the first principal stress [66], while its applicability was experimentally proved in low or negative triaxiality. In CWR, the triaxiality varies in a wide range. Both the R&T model [69]and the Oyane model [61] described the void growth. Later on, Smith [75] expanded the application of the R&T model from high triaxiality to low triaxiality by introducing void shrinkage. However, none of them

considers shear effects, which is generally considered significant in CWR. The introduced Lode angle parameters enable ductile fracture prediction in low or negative triaxialities, such as shear fracture. However, the MMC model was applicable in monotonic loading conditions, while cyclic loadings are involved in CWR [76]. The X&W fracture criterion shows high accuracy in a wide range of stress states with the consideration of triaxiality and Lode parameter [66], but similarly, its application is limited in the monotonic loading conditions. Pater's model considers both the void formation and shear fracture in a hybrid damage model. The involved C&L model was applied for the high triaxiality; however, this model was proved to work well only in low or negative triaxialities [66]. Zhu's model adapted the R&T model with the consideration of shear effects, the prediction of which agrees well with the experimental observation in the 12 CWR cases, as shown in Figure 6.6. However, four independent material constants are included in Zhu's model, which will be a heavy burden for the industry to do the calibrations, especially at elevated temperature. Regarding the new fracture criterion proposed in this study, only three simplified CWR tests were conducted for the material constant calibration, requiring only one pair of dies with simplified geometry in practice.

However, for brittle fracture, the plastic strain-based fracture criterion shows insufficiency in predicting the fracture accurately. In contrast, the stress-based fracture criterion considering the maximum shear stress and the first principal stress presents high prediction accuracy, as proved in Chapter 4. Thus, the stress-based criterion is an essential part of predicting central cracking accurately.

The fundamental understanding of the central crack mechanisms and criterion solved the longstanding Mannesmann Effect problems in the

manufacturing community and provided useful guidance for the CWR industry in producing high-quality products.

6.6 Conclusion

In this research, a physical CWR model with the plasticine workpiece was built for the lab reproduction of CWR. The corresponding FE model was built to track the stress/strain/damage evolutions. New plasticine/flour composites were designed to reveal the materials ductility effects on central crack mechanisms. A damage model set was proposed and validated by 60 groups of CWR data. The following conclusions can be drawn:

(1) A physically based unified damage model set was proposed for predicting the central crack formation in materials with different levels of ductility. A stress-based fracture criterion is applicable for low ductility materials, while an energy-based one is proposed for high ductility materials. The robustness of this damage model set was validated by 60 groups of CWR experimental data with various materials, including C45 steels, pure aluminium and plasticine/flour composites. Its high robustness can effectively drive its industrial applications.

(2) The predominant effects of the plastic strain and the maximum shear stress were demonstrated in the damage model for the high ductility materials. Its robustness was validated by 17 groups of CWR tests on hot steels and pure plasticine. The 10 existing damage models were proved to be incapable of describing the central cracking quantitively.

(3) The multiple fracture mechanisms of materials at different ductility levels were revealed using newly designed plasticine/flour composites with ductility varying from 6% to 49%. When the ductility is low, stress-driven crack nucleation plays a dominant role. In contrast, in the highly ductile fracture, the

fracture mechanisms of void growth and distortion dominate, when the plastic strain effects become significant.

Chapter 7 Microstructural study on central crack mechanisms

7.1 Introduction

This chapter focuses on exploring the fracture mechanism on a microscopic scale based on industrial cases, which will enhance the understanding of macroscopic fracture mechanisms of central cracks. It frequently happens in the industry that billets from different batches for CWR result in different central cracking behaviours even all the batches have passed strict quality examinations in terms of yield and ultimate strength, ductility, porosity, etc., which causes large economic loses. It was suspected that the different initial microstructure causes central crack formation, given that all the mechanical processes are identical. However, the microstructure evolution of high strength steel is complex, including phase transformation, grain growth, recrystallization, etc., making it a challenge to determine the critical parameter for central crack formation. In this chapter, detailed investigations are conducted on the samples from two batches to determine the key microstructural parameter for central crack formation, enabling the industry to produce high-quality CWR products by controlling the microstructural evolution. The methods involved in this chapter are described in Sections 7.2, including the description of the as-received materials and heat treatment processes, etc. The uniaxial tensile test results of samples at room temperature and elevated temperature (with heat treatment) are compared in Section 7.3. The materials with or without heat treatment were characterised and compared in terms of the inclusions, grain size, chemical compositions and phase compositions in Sections 7.4 and 7.5. In the last section, the critical microstructural factor for central cracking and the cracking evolutions are discussed.

7.2 Materials and methodology

7.2.1 Material description

Two 20NiCr3H steel samples were supplied by Helai Ltd. A representative transverse section and the typical microstructure at the central region are illustrated in Figure 7.1. The samples were taken from two different steel billets, Billet 1 and Billet 2. Billet 1 was selected from the batch of steel that was not found to exhibit central cracking, while Billet 2 was selected from a different batch that had produced cracked products, as shown in Figure 7.1 (b1) and (b2). Both samples exhibited similar phase compositions, pearlite and ferrite. Table 7.1 presents the nominal chemical compositions of the steels. These two batches of steel billets were manufactured by the same process (continuous casting and rolling). The total weight of each batch was around 50 tonnes. One hundred billets from each batch were selected and processed using the same CWR process to confirm the consistency of central crack formation in each batch; that is, the billets were first heated to 1080 °C in a furnace within 65 s, then placed in a CWR machine (H1200) with the same tools (forming angle 30 °, stretching angle 7.5 °, and area reduction ratio of 58%) at the same rolling speed (20 m/min). After rolling, all of the CWR products were cooled in the air, followed by ultrasonic flaw testing to inspect central cracks. The 100 billets from Batch 1 did not show any central cracks, while those from Batch 2 were all centrally cracked.
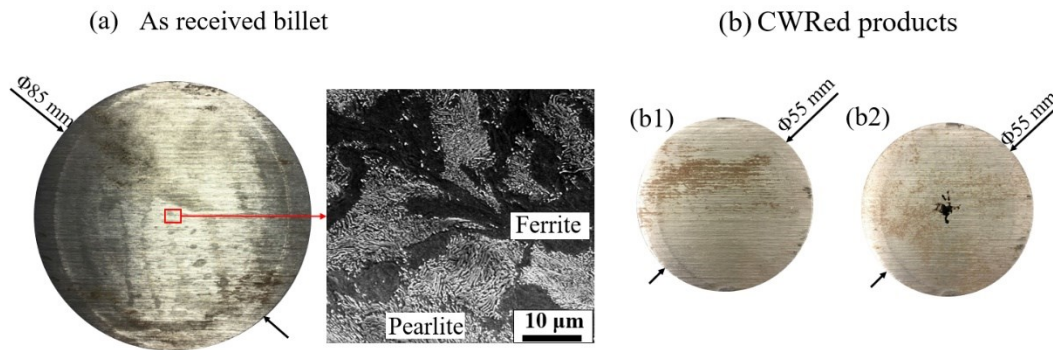
Figure 7.1 As-received materials: (a) the transverse cross-section of one billet along with the SEM characterised microstructure at the central region; (b1) and (b2) the CWR-formed axial products from Billets 1 and 2, respectively.

Table 7.1 The nominal chemical compositions of the steel 20CrNi3H [138]

Chemical compositions	C	Si	Mn	P	S	Cr	Ni	Cu	[O]
GB/T5216-85	0.17/0.23	0.17/0.37	0.30/0.65	≤0.035	≤0.035	0.60/0.95	2.70/3.25	≤0.20	≤20 ppm

7.2.2 Thermomechanical tests

The mechanical properties of two billets at both room temperature and the hot rolling temperature of 1080 °C were determined from uniaxial tensile tests using a Gleeble 3800 test machine. The tensile test specimen geometry and location in the billet cross-section is illustrated in Figure 7.2 (a). For the tests under hot rolling conditions the specimens were heated to 1080 °C within 65 seconds (at a heating rate of 16.2 °C/s), then pulled to fracture at a strain rate of 1/s. The samples were cooled down in the air. A thermocouple was spot welded on the surface of the specimen's central region to record and control the temperature. A dilatometer was applied to record the width change during the tests. The above process was repeated for the tensile tests at room

temperature with the same sample geometry and strain rate but without any heating process. At least three tests at room temperature and 1080°C were conducted to ensure the results' repeatability.
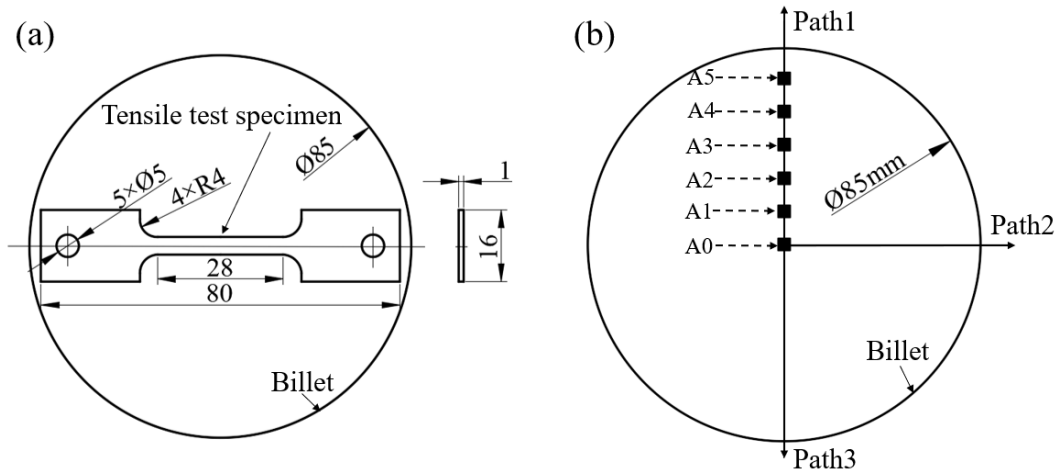
Figure 7.2 Schematic illustration of (a) geometry and location of the tensile testing specimen on the billets and (b) the regions of interest on the transverse section of the billet.

7.2.3 Heat treatment process

The same thermal profile was applied to replicate the preheating stage of CWR to investigate the preheated microstructure changes prior to plastic deformation. Cubic samples at $5 \times 5 \times 3$ mm^3 were cut from the central regions of both Billets 1 and 2, indicated as the A0 region in Figure 7.2 (b). The samples were heated to 1080 °C and held for 65 seconds in a preheated furnace, then were immediately water quenched to freeze the formed microstructure.

7.3 Thermomechanical test results

7.3.1 Stress-strain curves

The stress-strain curves for the two billets at room temperature and at 1080 °C are compared in Figure 7.3. The specimen fracture areas are displayed as insets. The ductility of Billet 1 (crack-free) was considerably higher than that of Billet 2 (central cracked), both at room temperature and at elevated temperature. At room temperature, the fracture strain of Billet 2 was approximately 50% lower than that of Billet 1 – 0.07 and 0.12, respectively. At elevated temperature, the ductility of both samples increased significantly. The fracture strain of Billet 2 doubled, but it was still only half of that of Billet 1. Although the difference in ductility between two samples was significant, it is interesting to note that their flow stress levels were similar. At room temperature, the yield strengths were almost the same, at approximately 490 MPa, and the ultimate strengths were 685 and 690 MPa, for Billets 1 and 2, respectively. At 1080 °C, the yield strength of Billet 2 was 46 MPa, with an ultimate strength of 60 MPa, slightly higher than that of Billet 1 (54 MPa).
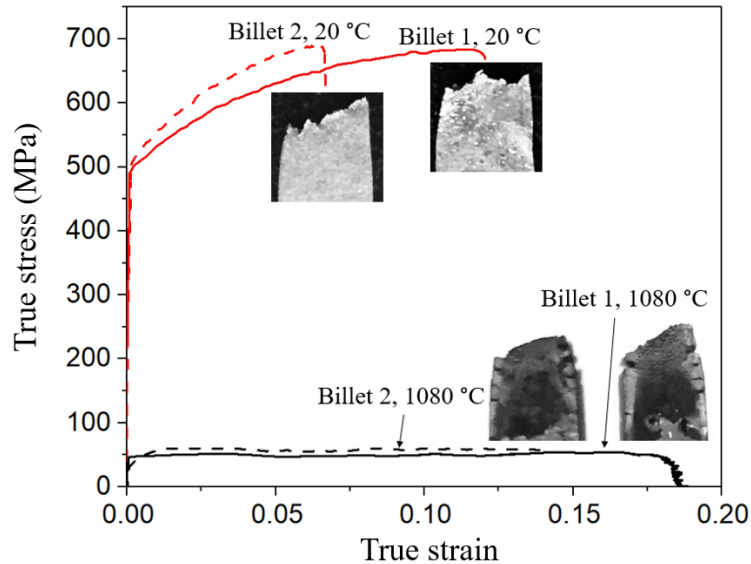
Figure 7.3 True stress - true strain curves of the two billets at room temperature and rolling temperature.

7.3.2 Fracture surface

Figure 7.4 presents the fracture micrographs from the tensile specimens. The ductile fracture was observed in billets deformed and fractured at room temperature, while the intergranular fracture was observed at elevated temperature. According to Figure 7.4 (a) and (b), large numbers of dimples and cracks were observed in both specimens, indicating ductile fracture at room temperature in both billets. The clear regular patterns show that the cracks were prone to propagate through the thickness direction, as indicated by the blue arrows in Figure 7.4 (a) and (b). This corresponds to the axial direction of the as-received billets. Based on a closer look, large and elongated inclusions were scattered throughout, identified as MnS using SEM/EDX. When comparing the room temperature fracture surfaces of the two billets, it is clear that the fracture surface of Billet 2 was rougher, and the crack propagating paths were more random, whereas the cracks in Billet 1 propagated mainly along the thickness direction. This may point to the more significant presence of MnS inclusions formed in Billet 2.

At elevated temperature, intergranular fracture occurred in both billets, as shown in Figure 7.4 (c) and (d). The fracture nucleated on the transverse section, then propagated along the loading direction, and finally failed along the transverse section. Unlike the rough surface at room temperature, the fracture surfaces were relatively smooth. Large particles were observed, and higher magnification images indicate these may be austenite grains. The austenite grains observed in Billet 2 were significantly smaller than those in Billet 1. This may be due to constrained dynamic recrystallisation in Billet 2 resulting from the inclusions hindering grain growth.
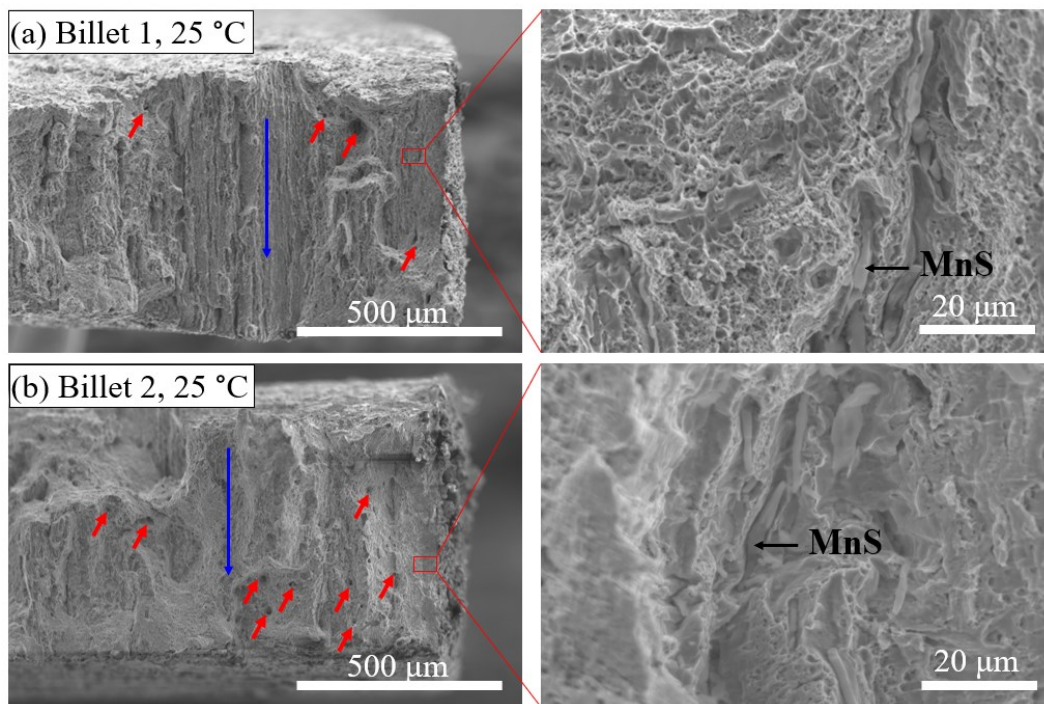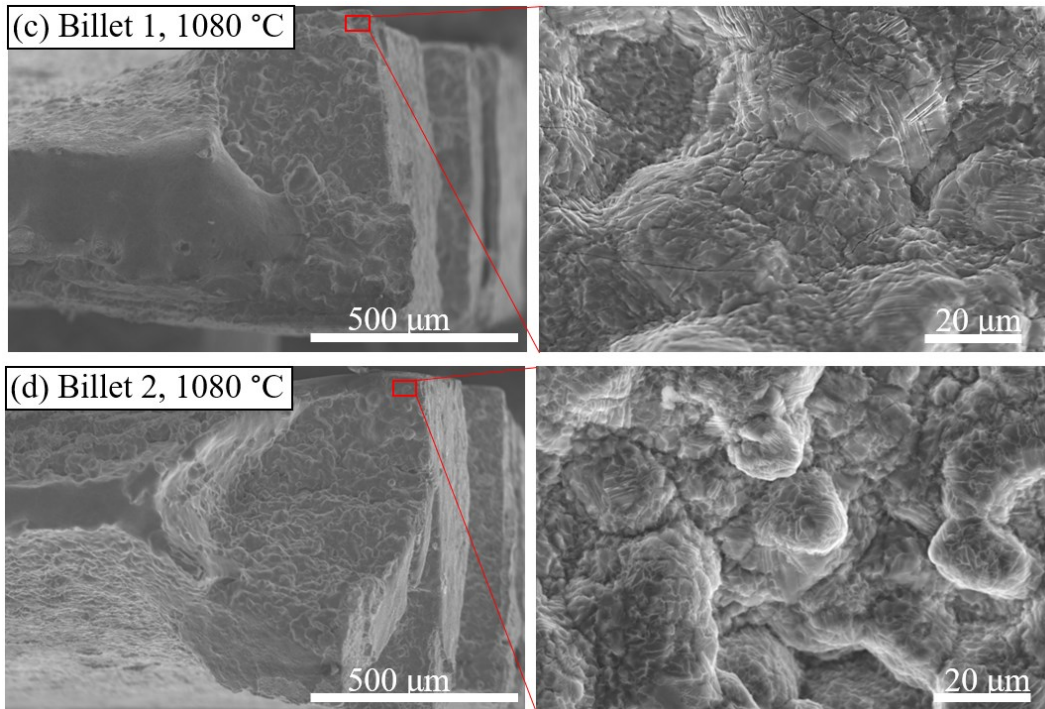
Figure 7.4 Fractography of two high strength steel billets after uniaxial tensile tests at room temperature and at 1080 °C.

The longitudinal section of the fracture tips for the two elevated temperature samples are shown in Figure 7.5. A comparison of the macroscopic images in Figure 7.5 (a) and (b) reveals intensive secondary cracks in Billet 1. In both cases, the cracks propagated along the same direction, normal to the loading direction. Under a higher magnification, as depicted in Figure 7.5 (c), it is clear that the crack edges were not strictly normal to the loading direction but were distributed along the prior austenite grain boundaries, confirming the intergranular nature of the fracture. A layer of iron oxides between the crack and the steel matrix is also observed. This layer is suspected of having been formed after the tensile test, possibly during the sample preparation process, as steel tends to oxide quickly in the air. Through observing the gap between the iron oxides and the steel matrix, as illustrated in Figure 7.5 (c) and (d), some granular voids were observed with weak signals of oxides, sulphides, and silicates. These may be attributed to the residual debris of the oxides and

126

silicates. These are 'hard' phases and may have separated from the steel matrix during the tensile test or been removed during the subsequent sample preparation. However, the EDX signal of the MnS inclusions was strong, as indicated in Figure 7.5 (g). This is probably due to the greater compatibility between the MnS inclusions and the steel matrix.

In the longitudinal section of Billet 2, no secondary cracking was observed, as shown in Figure 7.5 (b), indicating that Billet 2 was less ductile than Billet 1. The fracture occurred and propagated rapidly along the primary crack without triggering any visible secondary cracks. On investigating the crack propagation, MnS inclusions were found along the crack tip, suggesting that the MnS inclusions accelerated the crack propagation and determined the crack propagating route. This supports previous studies, which have found that MnS inclusions increase the anisotropy of ductility, as observed by Pickering [139], Holappa and Helle [140] and Bhadeshia and Honeycombe [141].
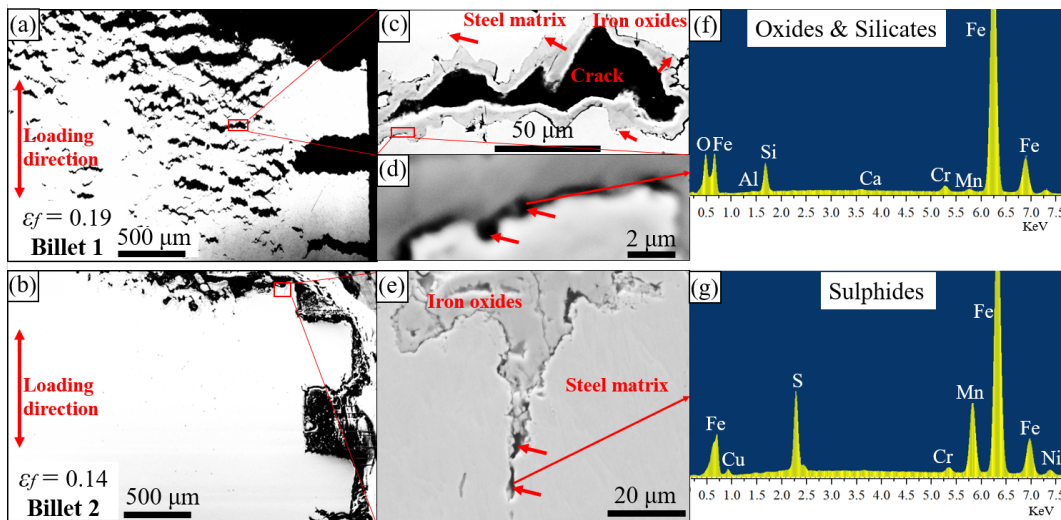
Figure 7.5 Microstructure of the longitudinal section of specimens after tensile tests at 1080 °C: (a)(b) macrostructure of Billets 1 and 2 at the fracture tips; (c)(d) one crack in Billet 1 at various magnifications; (e) crack propagation in Billet 2; (f)(g) typical inclusions in Billets 1 and 2.

7.4 Characterisation of inclusions

The inclusions present in the two as-received billets, before and after the heat treatment (heated to 1080 °C and water quenched), are compared in Figure 7.6 and Figure 7.7. Before the heat treatment, both elongated and granular defects were observed in the two billets, as depicted in Figure 7.6 (a) and (b). Figure 7.6 (c) and (d) present individual typical granular and elongated inclusions in the two billets. The granular defects were identified to be oxides, such as Al_2O_3, MgO, and CaO (Figure 7.6(f)), while the elongated ones were mostly made by sulphides, such as MnS (Figure 7.6(g)). Inclusions MnS and CaS occasionally appeared along with the oxides, as illustrated in Figure 7.6 (e).

After the heat treatment, the inclusions significantly altered in terms of size, number, and chemical composition, as demonstrated in Figure 7.7. It can be clearly seen from Figure 7.7 (a) and (b) that the size and number of inclusions increased after the heat treatment, as compared with those in Figure 7.6 (a) and (b). The number of inclusions in Billet 2 was higher than that in Billet 1, whereas this trend was not observed at room temperature. As illustrated in Figure 7.7 (c) to (e), large gaps were found between the inclusions and the steel matrix, while, at room temperature, they were well bonded, as shown in Figure 7.6 (c) to (e). In addition, based on Figure 7.7 (f) to (h), it is clear that the chemical components became more complex, with a new type of inclusion (silicates) being formed due to element diffusion at the high temperature.

In terms of the morphologies and chemical composition, there was no difference between the two billets at room temperature and at 1080 °C. However, at 1080 °C, the number and size of inclusions in Billet 2 were notably higher than in Billet 1.
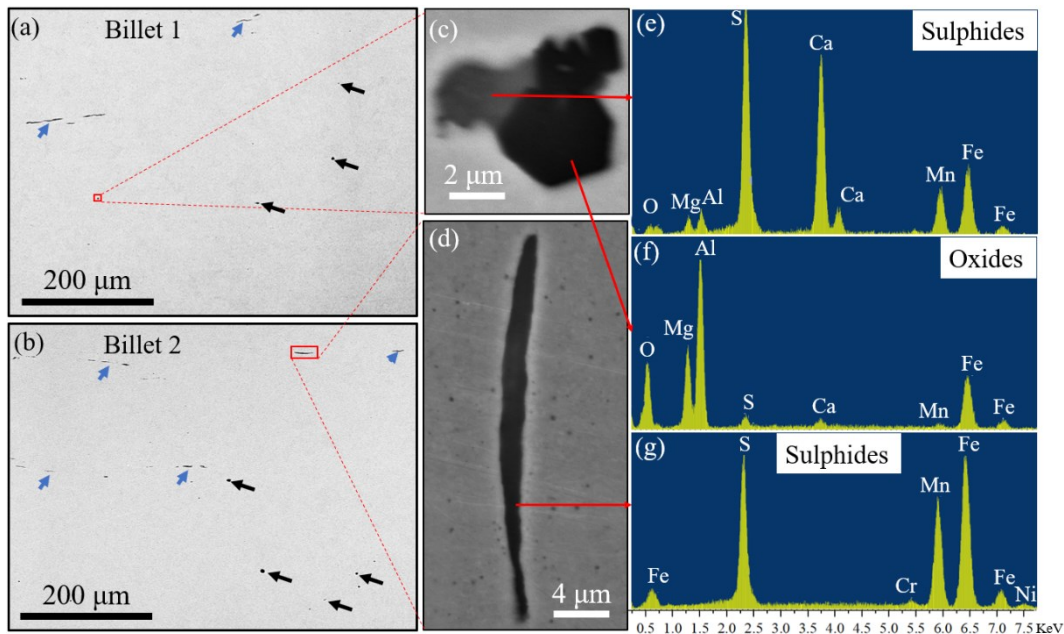
Figure 7.6 Inclusions distribution and identification in the two as-received billets: (a)(b) backscattered images showing inclusions in Billets 1 and 2; (c)(d) typical inclusions in Billets 1 and 2; (e)(f)(g) chemical compositions of the typical inclusions.

A quantitative comparison of the inclusion histograms for the two billets is presented in Figure 7.8. The histograms show that there were more small inclusions and less large ones in all samples. Comparison of the inclusions in Billets 1 and 2 reveals that the number of inclusions in Billet 2 was always higher than that of Billet 1, both with or without heat treatment and in nearly all inclusion size ranges. The heat treatment significantly increased the number of inclusions in Billet 2, especially inclusions sized between 0 and 40 μm^2. This number was nearly three times that in Billet 1, suggesting that the slight difference in inclusion quantity at room temperature became significantly enlarged at elevated temperature.
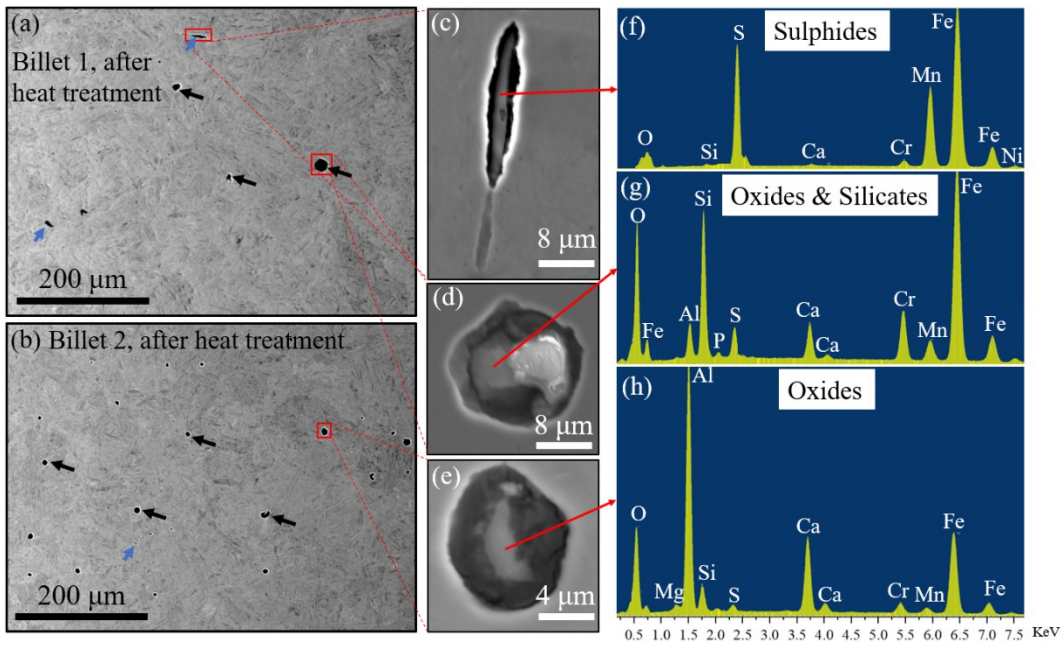
Figure 7.7 Inclusions distribution and identification in the two billets after heat treatment: (a)(b) backscattered images show impurities in Billets 1 and 2 after heat treatment; (c)(d)(e) typical inclusions in Billets 1 and 2 after heat treatment; (f)(g)(h) chemical compositions of the typical inclusions.
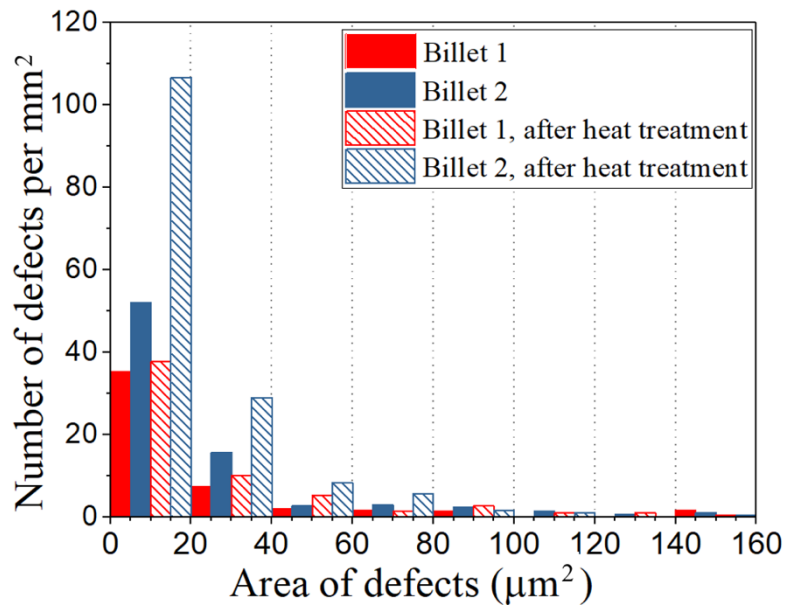
Figure 7.8 Histogram of inclusions in the two billets before and after heat treatment.

7.5 Characterisation of chemical and phase compositions and grain size

Figure 7.9 presents the chemical components of elements Cr, Mn, and Ni in the two billets and compares them with the specification. The difference in the element content between the two samples was minimal. The results also indicate that each element was uniformly distributed from the centre to the edges in both billets, and that all chemical content was within specification. This confirms that chemical composition and distribution were in close agreement with the specification provided by the steel supplier.

Figure 7.10 displays the distributions and components of the phases in the two billets before and after the heat treatment. The phase components of the four samples were consistent, containing ferrite, cementite, and austenite. However, the phase fractions between the two samples significantly differed before the heat treatment, as evidenced in Figure 7.10 (a) and (b). In Billet 1, the percentage of ferrite was as high as 95.58%, with a tiny amount of cementite and austenite, while, in Billet 2, the percentage of austenite reached 23.38%. A significant difference in phase fraction may lead to different microstructures at high temperature. Heat treatment was applied to allow comparison of the microstructures at the rolling temperature. The heat treatment was applied without any loading of deformation of these specimens.

Figure 7.10 (c) and (d) illustrate that the heat treatment induced homogeneous phase structures. The difference in ferrite content between the two samples was as little as 0.01%. The differences in the other two phases were also minimal because the steel was fully austenitised during the heat treatment at 1080 °C. The austenitising temperature for this steel is 850 °C.
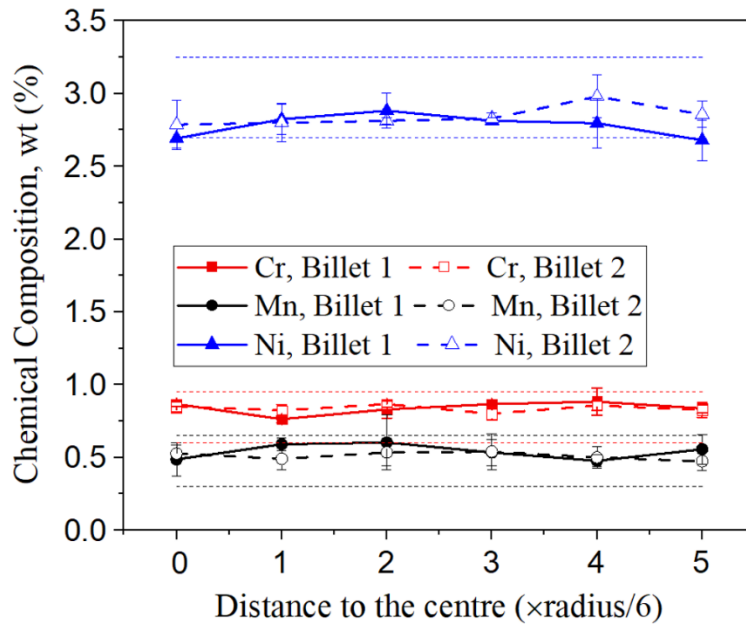
Figure 7.9 Chemical distribution of Cr, Mn, and Ni on the cross-section of the two billets (dashed lines with the same colours present the specification's requirements).

	Billet 1	Billet 2	Billet 1 (After heat treatment)	Billet 2 (After heat treatment)
Ferrite (%)	95.58	68.35	92.98	92.97
Cementite (%)	0.66	8.25	3.00	3.62
Austenite (%)	3.76	23.38	4.02	3.41
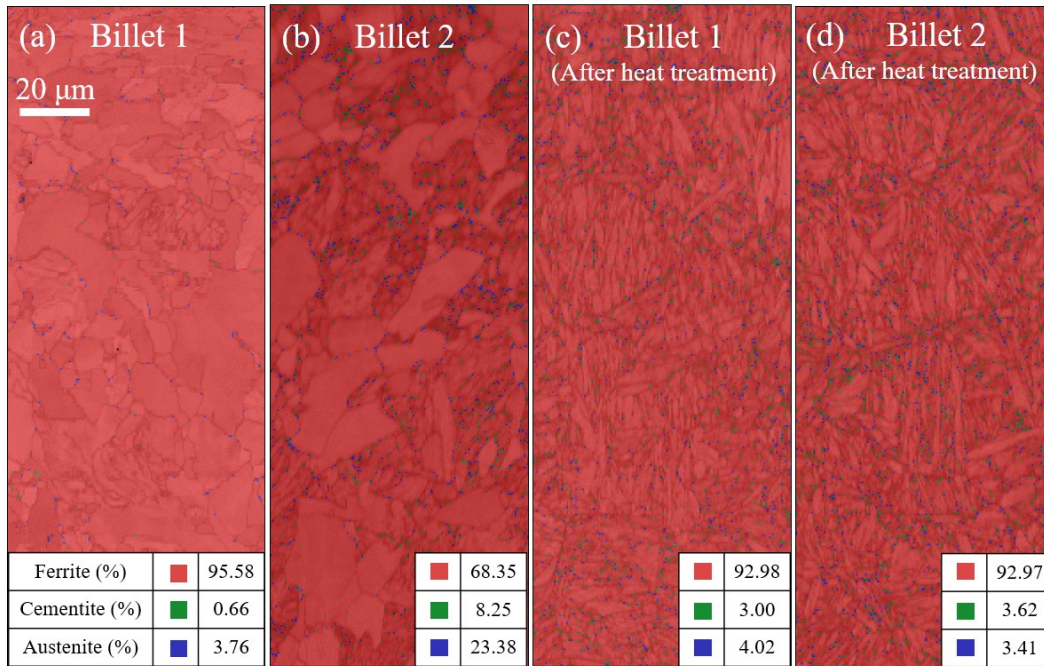
Figure 7.10 Phase comparisons of billets before and after heat treatment.

The average grain size of the two billets before and after the heat treatment is also compared in Figure 7.11. Again, only a small difference in grain size was found between the two billets. Before the heat treatment, the grain size in Billet 1 was 4.9% larger than that in Billet 2, while, after the heat treatment, the difference was reduced to 0.75%. This means that the heat treatment also reduced the difference in grain size between the two billets.

(a) Billet 1	(b) Billet 2	(c) Billet 1 (After heat treatment)	(d) Billet 2 (After heat treatment)

Average grain size (µm)	GS	4.27
Standard deviation	SD	4.02

GS	4.06
SD	5.6

GS	2.66
SD	3.41

GS	2.64
SD	3.08
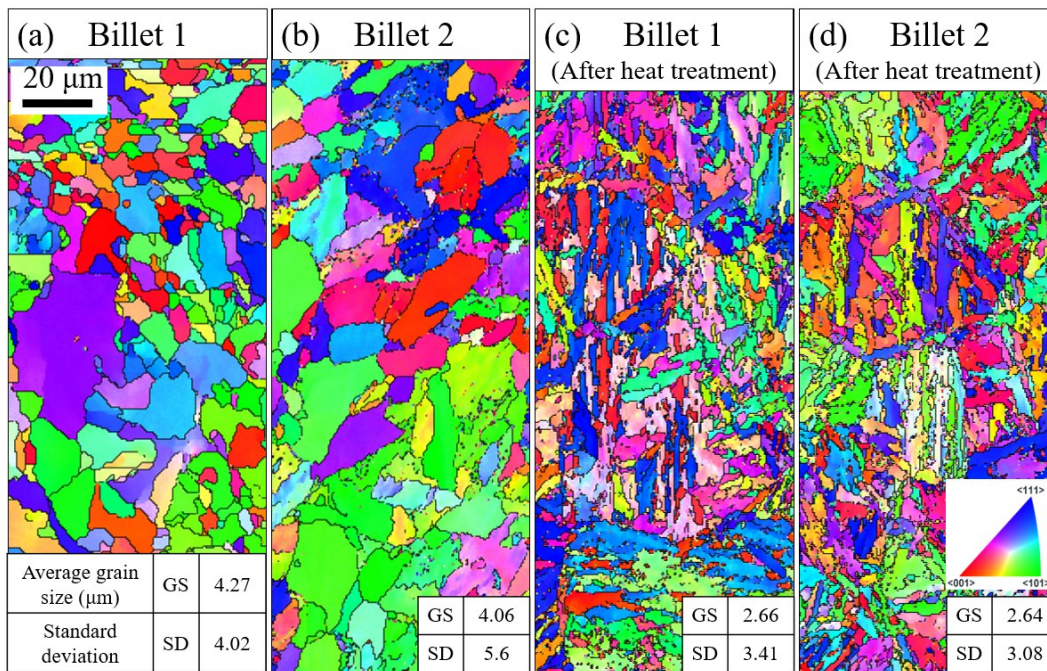
Figure 7.11 Grain size distribution of the two billets before and after the heat treatment.

7.6 Discussion

7.6.1 Reasons for low hot ductility

It is widely known that intrinsic factors such as inclusions, chemical segregation, grain size, and phase composition significantly affect ductility during subsequent hot forming for a given initial material. In most cases, a small grain size will improve hot ductility [142–145]. High amounts of large inclusions typically have a detrimental effect on metals' formability and must be strictly controlled [146–149]. Alloying elements such as V and B are beneficial to the hot ductility of steel, but some elements, such as Ti, are not [150, 151]. The initial phase composition and volume fraction affect the subsequent recrystallisation and phase transformation process, as well as ductility [152]. In the presented work, all four of these factors have been considered, analysed and compared.

Significant differences were identified between the phase volume fractions and inclusions within the two billets in the as-received condition, as illustrated by Figure 7.8 and Figure 7.10 (a) and (b). These two critical microstructural factors do, however, demonstrate highly distinct trends after the heat treatment. The differences in phase volume between the two samples were significantly reduced as phase transformation resulted in homogenisation, as demonstrated in Figure 7.10 (c) and (d). However, after the heat treatment, significantly more and larger inclusions were found in Billet 2 (the cracked billet) compared to Billet 1, as shown in Figure 7.8. Therefore, inclusions can be identified as potentially being the critical factor responsible for central crack formation. This is consistent with the findings of Huo et al. [8] and Yang et al. [27], which state that the inclusions in CWR are considered to be a nucleation source for central cracks. This also aligns well with the general concept that inclusions are primary factors driving central crack formation [1, 53].

All other microstructural factors, such as chemical composition and grain size, exhibited little difference between the two billets. Therefore, they are highly unlikely to have resulted in the central cracks found in this study.

7.6.2 Inclusions evolution and crack formation

By comparing Figure 7.5, Figure 7.6 and Figure 7.7, the inclusion evolution in terms of chemical composition, distribution, and morphologies can be seen. According to Figure 7.6 and Figure 7.7, it is clear that both samples experienced an increase in size and number of inclusions due to the thermal expansion and the formation of new inclusions at the high temperature. The newly formed microvoids/cracks resulted from the different thermal expansion coefficient and elasticity between the steel matrix and the inclusions. This generated stress concentration around the inclusions and finally led to microvoid/crack formation. These microvoids/cracks became the nucleation sites for the subsequent fracture. The complicated chemical compositions of the inclusions after the heat treatment, as depicted in Figure 7.7 (f), (g), and (h), indicates that strong diffusion occurred during the heat treatment, and new inclusions, such as silicates, were generated.

The inclusions along the edges of the tensile test cracks were characterised, as shown in Figure 7.5. Although the numbers of inclusions in Figure 7.5 (f) and (g) were not very high, oxides and silicates were observed around the crack edges and in the steel matrix. Pre-existing inclusions were still observed in the undeformed samples after the heat treatment, as shown by comparing Figure 7.6 (a) & (b), (as-received) with Figure 7.7 (a) & (b), (after heat treatment). The size of inclusions in Figure 7.5 (d) was small compared to the inclusions after the heat treatment. This is mainly due to the debonding between the steel matrix and the inclusions during the tensile test. Larger inclusions are more susceptible to this decohesion due to the accumulated stress between the interface with the matrix. However, the MnS is relatively

135

soft and deformable at high temperature, so similar numbers of MnS inclusions were still observed after the tensile test.

Under the plastic deformation, the previous microvoids/cracks in Figure 7.7 (c) to (e) grew and coalesced along the direction normal to the loading direction, as illustrated in Figure 7.5 (a). Meanwhile, as the plastic deformation proceeded, new microvoids/cracks formed due to inclusions fracture, debonding between inclusions and steel matrix, or damage to the steel matrix [153]. With increasing plastic deformation, the voids/cracks quickly propagated the crack and led to the fracture.

In summary, during the heat treatment process, element diffusion, new inclusion formation and inclusion growth occurred simultaneously. Microvoids/cracks were formed. During the tensile test, these microvoids/cracks then grew and coalesced and finally led to fracture during the plastic deformation process.

7.6.3 Fracture mechanisms in cross wedge rolling

The embrittlement resulting in premature fracture during the hot tensile test, depicted in Figure 7.4 (c) and (d), occurred when Gleeble 3800 was used to replicate the CWR process. Previous studies demonstrated that the steel experienced a ductility drop at a temperature ranging from 900 to 1200 °C, which was suggested due to the aggregation of sulphites and oxides at grain boundaries [146, 154]. The inclusions, such as oxides and sulphides, as observed in Figure 7.4 (c) and (d), are considered to be the dominant factor responsible for the low ductility.

At elevated temperature, microvoids/cracks are formed at the inclusion-steel matrix interface due to the accumulated thermal stress generated by a mismatch between the thermal expansion coefficients of inclusion and matrix. Simultaneously, grain boundary and phase boundary migration occur during

the associated recrystallisation and phase transformation, thus resulting in the aggregation of inclusions adjacent to the grain boundaries. This reduces the grain boundaries' strength as compared to the grain interiors, facilitating crack propagation along grain boundaries, as shown in Figure 7.5 (c). On a microscale, the crack propagation direction was controlled by the grain boundaries or inclusions, as indicated in Figure 7.5 (e), whereas, on a macroscale, the overall direction was determined by the stress state, as depicted in Figure 7.5 (a) and (b). As further deformation was imposed during this CWR simulation process, micro-and macrocracks formed and propagated, leading to the final fracture of the material.

The inclusions in Billet 2 were denser and larger than those in Billet 1, as seen in Figure 7.8. At the CWR temperature, the difference in the inclusions size and quantity was enlarged because the thermal process facilitated to reveal the edges of the initial inclusions (e.g. MnS) due to their thermal coefficient mismatch with the matrix materials and the formation of new inclusions (e.g. silica) caused by fast diffusion and chemical reaction. The high quantity of inclusions in Billet 2 accelerated the element concentration and facilitated new inclusions [155–157]. The large-sized inclusions facilitated crack initiation, while the large volume fraction of inclusions accelerated the crack propagation along the grain boundary. As illustrated in Figure 7.3, this resulted in the premature fracture in Billet 2, as demonstrated by the billet's lower ductility.

Furthermore, in industry, the workpiece's loading condition is much more complex as studied in Chapter 4, subjected to triaxial stress state, cyclic loading, and large plastic strain. This complex loading condition accelerates the decohesion between the inclusion and steel matrix. Figure 7.12 shows one large inclusion on the crack surface. A more detailed discussion on the important role of inclusions in cracking formation during the CWR was

presented in Ref [27]. It demonstrated that the inclusions provided the nucleation sites for voids formation, generated strong localised stress-causing voids coalescence, and finally formed visible cracks under continuous growth and coalescence. Due to the specific loading conditions and the specific fracture mechanism (shear cracking), the material is sensitive to inclusions. Therefore, to produce crack-free products, it is necessary to establish specific standards to specify the inclusion quantity and size in the CWR billet.
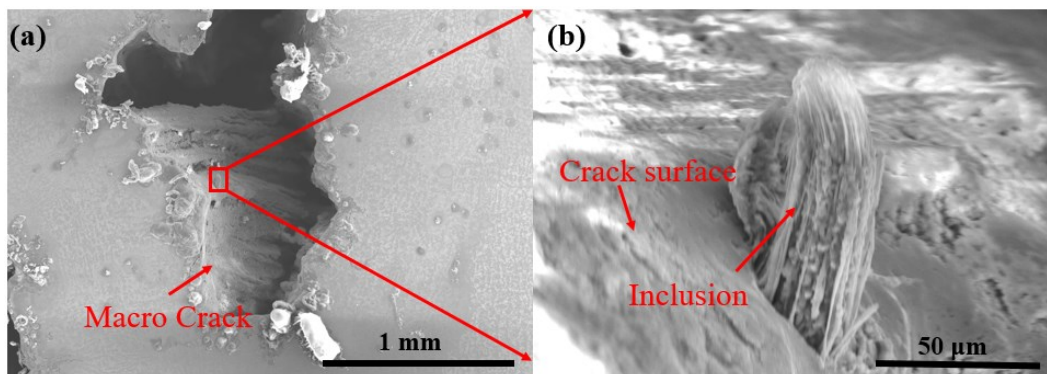
Figure 7.12 Cracked sample: (a) macro crack and (b) inclusions on the crack surface.

7.7 Conclusions

Central cracks in CWR were observed in one of two 20CrNi3H steel billets, both billets having the same chemical composition. These two billets were studied by experimentally simulating the CWR process in a tensile test using a Gleeble 3800 testing machine. The microstructure of samples taken from the two billets was characterised under various thermal and mechanical conditions. The primary reason for the central cracking was identified, and a fracture mechanism was suggested. The following conclusions can be drawn:

(1) Non-metallic inclusions, including oxides, sulphides and silicates, are the critical factors for central crack formation in the CWR of 20NiCr3H steels. The effects of the steel chemical composition, phase composition, and grain size were found less critical in this case.

(2) At the CWR temperature, the number and size of inclusions in the steels are enlarged, and microvoids/cracks initiate around the inclusions. Under the plastic deformation, microvoids/cracks propagate around the inclusions, and the presence of sulphides accelerates the crack propagation and leads to material anisotropy. The ostensibly compressive conditions in CWR makes the material more sensitive to inclusions.

(3) The premature fracture in steel Billet 2 (inclined to central cracking) could be attributed to the inclusions introduced grain boundary embrittlement, as they tend to aggregate along the grain boundary during the re-crystallisation at elevated temperature.

(4) Compared to other conventional forging processes, a stricter standard on inclusions should be specified for the CWR billets to produce qualified products due to the specific loading conditions.

Chapter 8 Conclusions

This work aimed to build fundamental understandings of the central crack mechanism and establish a robust fracture criterion for predicting central cracking in CWR. The fracture mechanism was investigated at the macroscopic and microscopic scales by means of the innovative physical model, FE model and advanced microscopic characterisation techniques. Plasticine was applied as the CWR workpiece in the physical model, enabling the reproduction of the industrial CWR process in the lab environment and allowing the dies to be efficiently 3D printed with a low cost and time. Specific stress states were achieved by varying the die geometries, and specific mechanical properties were achieved by varying the flour weight ratios within the plasticine/flour composites. A unified damage model set was developed based on the multiple central crack mechanisms, capable of predicting the central cracking in a full range of materials. The micro-fracture mechanism was revealed by systematically comparing the chemical/phase compositions, grain size and inclusions at both room and elevated temperature.

8.1 Methodology

The following conclusions can be drawn on the novel physical model and the material constants calibration method.

8.1.1 Innovative physical model

The physical model with the plasticine workpiece effectively addressed the long-lasting problem in CWR research, i.e. the high cost and long lead time in die manufacturing. A lab-scale CWR prototype enabled the reproduction of the industrial CWR process in a lab environment. A new material, i.e. plasticine/flour composite, was designed, which allowed the central crack

occurrence in relatively soft materials. By varying the flour content, specific mechanical properties were achieved, which allowed investigating the effects of ductility on fracture mechanisms. Due to the softness of the plasticine, the CWR dies were able to be 3D printed with polymer materials, which allowed to produce a large number of dies with various geometries in a short lead-time at a low cost.

8.1.2 Novel material constant calibration method

A novel material constant calibration method was proposed, which involves a limited number of interrupted CWR tests with a single pair of plates and FE process simulations. By rising the plate end, various feed angles can be achieved, generating different stress states. The material constants can be determined by comparing the cracked and non-cracked situations with the stress states obtained through FE modelling. It results in high accuracy due to the reproduction of CWR stress states and high efficiency due to the extremely simplified die geometry.

8.2 Fracture mechanism

8.2.1 Macroscopic understanding

The macroscopic fracture mechanism was investigated by the physical model and FE model, considering the effects of stress states and initial material properties.

A range of mechanistic factors was considered for central crack formation. In order to clarify their separated roles, nine pairs of dies with specific geometries were manufactured for achieving the specific stress states. By the comparison of the stress evolution in the FE model to the experimentally observed cracking status, it is found that the maximum shear stress was the

dominant factor, while the effects of the axial and secondary tensile stresses and the cyclic loadings are not significant.

The effects of initial mechanical property (i.e. ductility) on multiple fracture mechanisms were revealed by varying the flour contents in the plasticine/flour composites. It is experimentally noticed that the fracture mode transits from brittle fracture to ductile fracture. Multiple fracture mechanisms were discussed. For low ductility materials, the fracture is brittle, the fracture mechanism of which is crack nucleation, as multiple longitudinal cracking bands were observed in both highly strained pure aluminium and green plasticine mixed with 7.5 wt% of flour. For high ductility materials, severe plastic deformation occurred before the final fracture, leading to numerous voids formed before the final fracture, when the void distortion and growth were the dominating fracture mechanisms. Therefore, the plastic strain is critical for ductile central crack formation.

8.2.2 Microscopic understanding

The micro central crack mechanism was investigated with two high-strength steel billets (with and without a high potential to crack). The microstructure of two billets, including the chemical/phase compositions, grain size and inclusions before and after the heat treatment (simulating the preheating process in industrial CWR), were characterised. The inclusions contents were found to be very different between these two types of billets. The inclusions provide nucleation sites for central cracking. At high temperature, the inclusions tend to gather at the grain boundary, accelerating the intergranular fracture as well as the cracking propagation. With complex loading conditions (ostensible compression), the materials in CWR are more sensitive to inclusions. It is concluded that the inclusions are the critical microstructural factor leading to the formation of central cracks, and improved standard should be made to specify inclusion content within the initial billets.

8.3 Fracture criterion

A unified damage model set was established based on the multiple fracture mechanisms in the low and high ductility materials, validated by 60 groups of CWR cases under various die geometries and materials.

A strength-based fracture criterion was proposed for less ductile material considering the brittle fracture nature, as presented in Equation 5.1. The criterion combines the contributions of the maximum shear stress and the first principal stress, corresponding to the classic Tresca criterion and the maximum principal stress theory. A linear relationship between the maximum shear stress and the first principal stress is defined to present two kinds of competitive fracture mechanisms.

For high ductility material, severe plastic deformation occurs before fracture. An energy-based damage model was applied to predict the central cracking, as presented in Equation 6.1. The shear fracture and void formation are considered to be the dominant fracture mechanisms.

8.4 Future work

Some fundamental understandings of the central crack mechanisms and criterion have been achieved, but some areas deserve further investigations to enrich the understanding. The following topics are suggested for further study:

8.4.1 Research methodology

Materials

The current fundamental understanding of the central crack mechanism was mainly achieved by using plasticine materials and comparing them with the

limited fracture morphologies of metals such as pure aluminium and hot steels in literature. It is suggested that systematic comparison be conducted to further confirm the multiple fracture mechanisms in different materials such as steels and titanium. For the multiple fracture mechanisms in metals, the different mechanical property can be controlled by adjusting the rolling temperature.

Measurement technique

The internal voids/cracks in the current study were quantitatively analysed by sectioning the rolled samples and observing the voids/cracks on the cross-section. It affects the result accuracy due to the 3D distributions of the voids and cracks, especially when determining the void nucleation moment by conducting the interrupted tests. Advanced techniques such as computed tomography scan or 3D ultrasonic flawless test with high resolutions are suggested to be applied to achieve more accurate void nucleation position and moment and get the material constants accurately.

In addition, the strain values of the plasticine in the uniaxial tensile tests were obtained from the machine reading. To achieve higher accuracy, it is suggested that high technique measure such as Digital Image Correlation (DIC) applied.

8.4.2 Central crack mechanism

Macroscopic understanding

The dominant effect of the maximum shear stress was clarified in this study. However, currently, the triaxiality and the Lode angle parameter are intensively studied in damage mechanics areas. For example, the effects of the triaxiality and Lode angle parameter on the plasticity and the ductile fracture were investigated by Bai and Wierzbicki [136] through a wide range of lab tests in different stress states. It is known that the positive stress

triaxiality promotes void growth, while the negative value represents the void shrinkage. The Lode angle parameter involves the second and third invariants of the deviatoric stress tensor, capable of presenting the void distortion. Their combination is capable of presenting a full range of stress states [66]. The stress states in the CWR were presented in terms of the stress triaxiality and the Lode parameter plane by Pater et al. for the first time [7]. However, no research has been conducted on how the triaxiality and the Lode angle parameter affect the central crack formation. Thus, it is interesting to know if they can better present the stress states in CWR accurately and how these values affect the central cracking.

As mentioned above, the effect of the initial mechanical property (ductility) was studied with plasticine, but it is necessary to further confirm the fundamental understanding by carefully analysing the central crack morphologies in different metals, i.e., how the void/crack nucleates, grows, coalesces and propagates.

Microscopic understanding

The microstructural study on CWR in general is limited. The previous research paid more attention to the effects of process-related parameters such as die geometry, temperature and friction rather than the microstructural evolution. A quantitative study has been taken in this study to confirm the dominant effect of the inclusions. However, other microstructural parameters on the central crack formation were not thoroughly investigated. For example, the grain size inhomogeneity is noticeable across the rolled sample, but its effect is not considered in the damage model.

Meanwhile, the dominating fracture mechanisms, including the cracking nucleation in brittle fracture or the void growth and distortion in ductile fracture, have not been investigated at the microscopic scale such as how

the void/crack nucleates, grows, distorts, coalesce and propagates. The microscopic understanding is beneficial to build more accurate damage models.

8.4.3 Damage model

The proposed damage model set only considers the multiple fracture mechanisms in brittle and ductile fracture mechanism on a macro scale due to the limited project duration. The following future work is suggested to improve the damage model.

Clarifying the relationship between the competitive fracture mechanisms

A linear relationship was defined between the two competitive fracture mechanisms in both the fracture criteria for the low and high ductility materials. In practice, it may be more complicated. For example, their relationship may be related to the triaxiality, Lode angle parameters, temperature, or strain rate. Thus, the modification of their relationship is expected.

Determining the critical fracture strain

The critical fracture strain to differentiate the low and high ductility materials is vague. More experiments with different materials are required to identify the critical fracture strain quantitatively more accurately.

Microstructural concern

In this study, it is believed that crack nucleation is the dominating fracture mechanism in low ductility materials and void growth and distortion are the dominating mechanisms for the high ductility materials based on the fracture morphologies and the previous understandings. In Chapter 7, it is proved that the inclusions play a key role in the central crack formation, specifically, in the

void/crack nucleation and propagation; however, the effect of inclusion is not included in the proposed damage model. Thus, it is necessary to improve the current damage model with the consideration of the microstructural effects.

8.4.4 Applications to broader rotary manufacturing processes

The fundamental understandings of the fracture mechanism and criterion achieved in this study can be applied to other rotary compression processes, such as the rotary piercing process. Physical and numerical work has been taken by ME4 student Wei Chen in her final year project. It is experimentally validated that the proposed fracture criterion is applicable in the rotary piercing process. In her research, four groups of piercing process under different process parameters (roll gap) were conducted, and the damage evolution was extracted in the corresponding FE model by using three damage models (the proposed one, C&L and Oyane damage model). In the end, only the damage predicted by the proposed fracture criterion shows a high consistency with the cracks observed in experiments. It means that the achieved fracture mechanisms in this study enable us to address the classic Mannesmann effect. However, these findings have not been experimentally validated by the metals in piercing practice due to the time limitation. Thus, it is necessary to extend the central crack mechanism and criterion to more related manufacturing processes.

References

1. Fu XP, Dean TA (1993) Past developments, current applications and trends in the cross wedge rolling process. Int J Mach Tools Manuf 33:367–400. https://doi.org/10.1016/0890-6955(93)90047-X

2. Hu Z, Wang B, Zheng Z (2018) Research and industrialization of near-net rolling technology used in shaft parts. Front Mech Eng 13:17–24. https://doi.org/10.1007/s11465-018-0480-3

3. Pater Z (2014) Cross-Wedge Rolling. Elsevier

4. Li Q (2003) Characterization of failure mechanisms in cross wedge rolling. University of Pittsburgh

5. Huo Y, Bai Q, Wang B, et al (2015) A new application of unified constitutive equations for cross wedge rolling of a high-speed railway axle steel. J Mater Process Technol 223:274–283. https://doi.org/10.1016/j.jmatprotec.2015.04.011

6. Sun SH, Xiong Y, Zhao J, et al (2005) Microstructure characteristics in high carbon steel rod after warm cross-wedge rolling. Scr Mater 53:137–140. https://doi.org/10.1016/j.scriptamat.2005.01.011

7. Pater Z, Tomczak J, Bulzak T (2020) Establishment of a new hybrid fracture criterion for cross wedge rolling. Int J Mech Sci 167:105274. https://doi.org/10.1016/j.ijmecsci.2019.105274

8. Huo Y, Lin J, Bai Q, et al (2017) Prediction of microstructure and ductile damage of a high-speed railway axle steel during cross wedge rolling. J Mater Process Technol 239:359–369. https://doi.org/10.1016/j.jmatprotec.2016.09.001

9. Zhang N, Wang BY, Lin JG (2012) Effect of cross wedge rolling on the microstructure of GH4169 alloy. Int J Miner Metall Mater 19:836–842. https://doi.org/10.1007/s12613-012-0636-9

10. Mirahmadi SJ, Hamedi M, Ajami S (2014) Investigating the effects of cross wedge rolling tool parameters on formability of Nimonic® 80A and Nimonic® 115 superalloys. Int J Adv Manuf Technol 74:995–1004. https://doi.org/10.1007/s00170-014-6047-5

11. Sedighi M, Mahmoodi M (2009) An approach to simulate cold roll-

forging of turbo-engine thin compressor blade. Aircr Eng Aerosp Technol. https://doi.org/10.1108/00022660910954682

12. Li J, Wang B, Ji H, et al (2018) Numerical and experimental investigation on the cross-wedge rolling of powder sintering TC4 alloy. Int J Adv Manuf Technol 94:2149–2162. https://doi.org/10.1007/s00170-017-0992-8

13. GrandViewResearch (2019) Global Automotive Axle Market Size & Share Report, 2020-2027

14. Huang X, Wang B, Mu Y, et al (2019) Investigation on the effect of mandrels on hollow shafts in cross-wedge rolling. Int J Adv Manuf Technol. https://doi.org/10.1007/s00170-018-3093-4

15. Pater Z (2020) Numerical analysis of the cross rolling process of a hollow railway axle. Mechanik 48–52. https://doi.org/10.17814/mechanik.2020.8-9.15

16. Pater Z, Gontarz A, Tofil A (2011) Analysis of the cross-wedge rolling process of toothed shafts made from 2618 aluminium alloy. J Shanghai Jiaotong Univ. https://doi.org/10.1007/s12204-011-1119-2

17. Shao YY, Peng WF, Yu X, et al (2020) Effect of rolling parameters on forming quality of flat cross wedge rolling thread shafts. Proc Inst Mech Eng Part E J Process Mech Eng. https://doi.org/10.1177/0954408920952597

18. Kruse J, Jagodzinski A, Langner J, et al (2020) Investigation of the joining zone displacement of cross-wedge rolled serially arranged hybrid parts. Int J Mater Form. https://doi.org/10.1007/s12289-019-01494-3

19. Böhm C, Kruse J, Stonis M, et al (2020) Virtual element method for cross-wedge rolling during tailored forming processes. In: Procedia Manufacturing

20. Li J, Wang B, Ji H, et al (2017) Effects of the cross-wedge rolling parameters on the formability of Ti–6Al–4V alloy. Int J Adv Manuf Technol 92:2217–2229. https://doi.org/10.1007/s00170-017-0263-8

21. Pater Z (2000) Theoretical and experimental analysis of cross wedge rolling process. Int J Mach Tools Manuf 40:49–63. https://doi.org/10.1016/S0890-6955(99)00047-4

22. Pater Z, Tofil A (2017) Overview of the Research on Roll Forging Processes. Adv Sci Technol Res J 11:72–86. https://doi.org/10.12913/22998624/70645

23. Pater Z, Tomczak J, Bulzak T (2020) Rapid estimation of ductile crack formation in cross-wedge rolling. J Mater Res Technol 9:14360–14371. https://doi.org/10.1016/j.jmrt.2020.10.046

24. Hu Z, Yang C, Wang B (2012) Development of part rolling technology in China. Jixie Gongcheng Xuebao/Journal Mech Eng 48:7–12. https://doi.org/10.3901/JME.2012.18.007

25. Hu Z, Zhang K, Wang B (1995) Forming technology and simulation of cross wedge rolling

26. Li Q, Lovell M (2004) The establishment of a failure criterion in cross wedge rolling. Int J Adv Manuf Technol 24:. https://doi.org/10.1007/s00170-003-1607-0

27. Yang C, Dong H, Hu Z (2018) Micro-mechanism of central damage formation during cross wedge rolling. J Mater Process Technol 252:322–332. https://doi.org/10.1016/j.jmatprotec.2017.09.041

28. Piedrahita F (2005) Three Dimensional Numerical Simulation of Cross Wedge Rolling of Bars. Adv Technol Plast 1:257–258

29. Meyer M, Stonis M, Behrens B-A (2015) Cross wedge rolling and bi-directional forging of preforms for crankshafts. Prod Eng 9:61–71. https://doi.org/10.1007/s11740-014-0581-8

30. Zhu C, Zhang H (2018) Personal communication

31. Li Q, Lovell MR, Slaughter W, Tagavi K (2002) Investigation of the morphology of internal defects in cross wedge rolling. J Mater Process Technol 125–126:248–257. https://doi.org/10.1016/S0924-0136(02)00303-5

32. Smirnov VS (1947) The deformation process in cross rolling. stal 7:511

33. Tselikov AI, Lugovsko VM, Tretiyakov EM (1961) The theory of cross cold rolling on three-roll machine. Vestn Mashinostroeniya 7:49–54

34. Sukharev I, Ushakov B (1969) Investigation of Deformations and Stresses by the Method of Moiré Fringes. Mashinostroenie, Moscow

35. Poluchin PI, Voronov VK, Kudmn AB, et al. (1974) Deformation and Stress in Metal Forming. Metallurgiya, Moscow

36. Smirnov VS, V. A. Lunvev (1965) Supplementary stress in cross rolling under small reduction ratio. Izv AN SSSR 96–106

37. Smirnov VS, V. A. Lunvev (1965) Stress state in cross rolling. Izv Chem Metall 3:94–100

38. Higashino T, Saito Y, Toyama M, Kato K (1977) Stress analysis in plane-strain rotary compression of cylindrical billet. J Jpn Soc Technol Plast 18:605–612

39. Menson S (1974) Temperature Stress and Low Circular Fatigue. Moscow

40. Kolmogorov VL (1963) Defects in cross rolling and forgings. Izv Chem Metall 11:123–135

41. Kolmogorov VL (1970) Stresses, strains, fracture. Metallurgy, Moscow

42. Makushok E, Shukin V (1978) Axial damage of metal in cross rolling. Izv AN BSSR Set Fiz Tech Nauk 11:127

43. Shukin V (1972) Study of Deformation Stress State and Technical Possibility of Wedge Rolling. Avtoref. dis. kand. techn. nauk., Minsk

44. Shukin V (1980) Study method of deformation stress state based on sticky damage of metal. Izv AN BSSR Ser Fiz Tech Nauk 1:130

45. Shukin V (1978) Investigation of central cavity possibility in cross rolling. Izv AN BSSR Ser Fiz Tech Nauk 2:129

46. Guzavichus LV, Dubeni AS, Krasnevskij SM (1976) Cylindrical pattern to define plastic features of material in rolling process. Sov Pat A S 538272

47. Teterin P, Liuzin J (1960) The mechanism of metal rupture in cross rolling. stal 10:930–933

48. Lee HW, Lee GA, Yoon DJ, et al (2008) Optimization of design parameters using a response surface method in a cold cross-wedge rolling. J Mater Process Technol 201:112–117. https://doi.org/10.1016/j.jmatprotec.2007.11.287

49. Li Q, Lovell MR (2004) The establishment of a failure criterion in cross wedge rolling. Int J Adv Manuf Technol 24:180–189. https://doi.org/10.1007/s00170-003-1607-0

50. Bao Y, Wierzbicki T (2005) On the cut-off value of negative triaxiality for fracture. Eng Fract Mech 72:1049–1069. https://doi.org/10.1016/j.engfracmech.2004.07.011

51. Krasnievskin SM, Makusok EM, Scukin VJ (1983) Metal Cracking at Plastic Forming. Nauka i Technika, Minsk

52. Kolmogorov VL (1970) Stresses, Deformations, Cracks. Metallurgija, Moskva

53. Li Q, Lovell MR, Slaughter W, Tagavi K (2002) Investigation of the morphology of internal defects in cross wedge rolling. J Mater Process Technol 125–126:248–257. https://doi.org/10.1016/S0924-0136(02)00303-5

54. Pater Z, Tomczak J, Bulzak T (2017) Fem Simulation of the Cross-Wedge Rolling Process for a Stepped Shaft. Strength Mater 49:521–530. https://doi.org/10.1007/s11223-017-9895-z

55. Pater Z, Tomczak J, Bulzak T, Zniszczyński A (2018) The Problem of Material Fracture Prediction in Cross Rolling Processes. Adv Sci Technol Res J 12:184–189. https://doi.org/10.12913/22998624/100398

56. Liu G, Zhong Z, Shen Z (2014) Influence of reduction distribution on internal defects during crosswedge-rolling process. Procedia Eng 81:263–267. https://doi.org/10.1016/j.proeng.2014.09.161

57. Silva MLN, Pires GH, Button ST (2011) Damage evolution during cross wedge rolling of steel DIN 38MnSiVS5. Procedia Eng 10:752–757. https://doi.org/10.1016/j.proeng.2011.04.125

58. Huang X, Wang B, Zhou J, et al (2017) Comparative study of warm and hot cross-wedge rolling:numerical simulation and experimental trial. Int J Adv Manuf Technol 92:3541–3551. https://doi.org/10.1007/s00170-017-0399-6

59. Bulzak T, Pater Z, Tomczak J (2017) Numerical and experimental analysis of a cross wedge rolling process for producing ball studs. Arch Civ Mech Eng 17:729–737.

https://doi.org/10.1016/j.acme.2017.02.002

60. Novella MF, Ghiotti A, Bruschi S, Bariani PF (2015) Ductile damage modeling at elevated temperature applied to the cross wedge rolling of AA6082-T6 bars. J Mater Process Technol 222:259–267. https://doi.org/10.1016/j.jmatprotec.2015.01.030

61. Oyane M, Sato T, Okimoto K, Shima S (1980) Criteria for ductile fracture and their applications. J Mech Work Technol 4:65–81. https://doi.org/10.1016/0378-3804(80)90006-6

62. Cockcroft MG, Latham DJ (1968) Ductility and the workability of Metals. J. Inst. Met. 96:33–39

63. Cockcroft MG, Latham DJ (1966) A Simple Criterion of Fracture for Ductile Metals. National Engineering Laboratory, Glasgow

64. Oh SI, Chen CC, Kobayashi S (1979) Ductile Fracture in Axisymmetric Extrusion and Drawing-Part2: Workability in Extrusoin and Drawing. J Eng Ind 101:36–44. https://doi.org/10.1115/1.3439471

65. Pater Z, Tomczak J, Bulzak T, et al (2019) Prediction of crack formation for cross wedge rolling of harrow tooth preform. Materials (Basel) 12:. https://doi.org/10.3390/ma12142287

66. Wierzbicki T, Bao Y, Lee YW, Bai Y (2005) Calibration and evaluation of seven fracture models. Int J Mech Sci 47:719–743. https://doi.org/10.1016/j.ijmecsci.2005.03.003

67. Bao Y (2003) Prediction of Ductile Crack Formation in Uncracked Bodies. PhD Thesis 252

68. Freudenthal A (1950) The inelastic behavior of engineering materials and structures. JohnWiley & Sons: New York, New York

69. Rice JR, Tracey DM (1969) On the ductile enlargement of voids in triaxial stress fields ∗ . J Mech Phys Solids 17:201–217. https://doi.org/10.1016/0022-5096(69)90033-7

70. P.Brozzo, B.Delue (1972) a new method for the prediction of formability limits in metal sheets. In: proeeeding of the 7th Biennial Conference of the International Deep Drawing Research

71. Beremin FM (1981) Cavity formation from inclusions in ductile fracture

of A508 steel. Metall Trans A 12:723–731. https://doi.org/10.1007/BF02648336

72. Ayada M, Higashino T, Mori K (1987) Central bursting in extrusion of inhomogeneous materials. In: In Proceedings of the 2nd International Conference on Technology of Plasticity. Stuttgart, pp 553–558

73. Zhan M, Gu C, Jiang Z, et al (2009) Application of ductile fracture criteria in spin-forming and tube-bending processes. Comput Mater Sci. https://doi.org/10.1016/j.commatsci.2009.08.011

74. Zhu Y, Engelhardt MD (2018) Prediction of ductile fracture for metal alloys using a shear modified void growth model. Eng Fract Mech 190:491–513. https://doi.org/10.1016/j.engfracmech.2017.12.042

75. Smith C, Kanvinde A, Deierlein G (2017) A local criterion for ductile fracture under low-triaxiality axisymmetric stress states. Eng Fract Mech 169:321–335. https://doi.org/10.1016/j.engfracmech.2016.10.011

76. Bai Y, Wierzbicki T (2010) Application of extended Mohr-Coulomb criterion to ductile fracture. Int J Fract 161:1–20. https://doi.org/10.1007/s10704-009-9422-8

77. Wierzbicki T, Xue L (2005) On the Effect of the Third Invariant of the Stress Deviator on Ductile Fracture. Tech report, Impact amd Crashworthiness Lab Massachusetts Inst Technol Cambridge, MA

78. Xue L, Xue Liang (2007) Ductile fracture modeling: theory, experimental investigation and numerical verification. PhD Thesis

79. Bai Y (2008) Effect of Loading History on Necking and Fracture. Technology 1–262

80. Tichauer P (1965) Study of wedge pass of cross wedge rolling. Tr LPI 243:146–153

81. Awano T, Danno A (1968) Rolling force and rolling torque - a study of hot rolling of stepped shaft II. Sosei to Kako 88:296–303

82. Pater Z, Weroński W (1994) Determination of the contact area between the rolling tools and the workpiece in cross rolling process. J Mater Process Tech. https://doi.org/10.1016/0924-0136(94)90326-3

83. Avitzur B (1968) Metal forming: processes and analysis

84. Pater Z (1997) Theoretical method for estimation of mean pressure on contact area between rolling tools and workpiece in cross wedge rolling processes. Int J Mech Sci 39:233–243

85. Pater Z (1998) A study of cross wedge rolling process. J Mater Process Technol 80–81:370–375. https://doi.org/10.1016/S0924-0136(03)00212-7

86. Pater Z (1999) Numerical simulation of the cross wedge rolling process including upsetting. J Mater Process Technol. https://doi.org/10.1016/S0924-0136(99)00231-9

87. Pater Z (1998) Simulation of cross-wedge rolling process using the upper-bound method. Scand J Metall 27:120–127

88. R. Hill (1950) Mathematic Theory of Plasticity. Oxford

89. Gong W, Shu X, Peng W, Sun B (2012) The research on the microstructure evolution law of cross wedge rolling asymmetric shaft-parts based on parity wedge. In: Applied Mechanics and Materials

90. Ji H, Liu J, Wang B, et al (2017) A new method for manufacturing hollow valves via cross wedge rolling and forging: Numerical analysis and experiment validation. J Mater Process Technol. https://doi.org/10.1016/j.jmatprotec.2016.09.004

91. Regone W, da Silva MLN, Button ST (2009) Numerical and experimental analysis of the microstructural evolution during cross wedge rolling of V-Ti microalloyed steel. Rev Esc Minas. https://doi.org/10.1590/S0370-44672009000400013

92. Zhou J, Jia Z, Liu H, Wang M (2013) A study on simulation of deformation during roll-forging process using system of special shaped and hat groove. Rev Adv Mater Sci

93. Dong Y, Lovell M, Tagavi K (1998) Analysis of interfacial slip in cross-wedge rolling: An experimentally verified finite-element model. J Mater Process Technol. https://doi.org/10.1016/S0924-0136(98)00111-3

94. Lee HW, Lee GA, Yoon DJ, et al (2008) Optimization of design parameters using a response surface method in a cold cross-wedge rolling. J Mater Process Technol 201:112–117.

https://doi.org/10.1016/j.jmatprotec.2007.11.287

95. Hai D Van, Thi Hong Hue D (2015) Finite element simulation and experimental study on internal fracture of railway sleeper screw during cross wedge rolling process. In: Materials Science Forum

96. Kpodzo K, Fourment L, Lasne P, Montmitonnet P (2016) An accurate time integration scheme for arbitrary rotation motion: application to metal forming simulation. Int J Mater Form. https://doi.org/10.1007/s12289-014-1208-5

97. Bartnicki J, Pater Z (2005) Numerical simulation of three-rolls cross-wedge rolling of hollowed shaft. J Mater Process Technol 164–165:1154–1159. https://doi.org/10.1016/j.jmatprotec.2005.02.120

98. Bartnicki J, Pater Z (2004) The aspects of stability in cross-wedge rolling processes of hollowed shafts. J Mater Process Technol 155–156:1867–1873. https://doi.org/10.1016/j.jmatprotec.2004.04.278

99. Huang H, Chen X, Fan B, et al (2015) Initial billet temperature influence and location investigation on tool wear in cross wedge rolling. Int J Adv Manuf Technol. https://doi.org/10.1007/s00170-015-6882-z

100. Ying FQ, Pan BS (2007) Analysis on temperature distribution in cross wedge rolling process with finite element method. J Mater Process Technol 187–188:392–396. https://doi.org/10.1016/j.jmatprotec.2006.11.193

101. Romantsev BA, Huy TB, Skripalenko MM, et al (2018) Investigation of the Process of Screw Rolling in a Four-Roll Stand by Simulation. Metallurgist 62:618–626. https://doi.org/10.1007/s11015-018-0700-4

102. Dong Y, Tagavi KA, Lovell MR, Deng Z (2000) Analysis of stress in cross wedge rolling with application to failure. Int J Mech Sci 42:1233–1253. https://doi.org/10.1016/S0020-7403(99)00035-1

103. Tofil A, Tomczak J, Pater Z (2013) Cross wedge rolling with upsetting. Arch Metall Mater 58:. https://doi.org/10.2478/amm-2013-0150

104. Ying FQ, Pan BS (2007) Analysis on temperature distribution in cross wedge rolling process with finite element method. J Mater Process Technol 187–188:392–396. https://doi.org/10.1016/j.jmatprotec.2006.11.193

105. Chijiiwa K, Hatamura Y, Hasegawa N (1981) Characteristics of Plasticine Used in the Simulation of Slab in Rolling and Continuous Casting. Trans Iron Steel Inst Japan 21:178–186. https://doi.org/10.2355/isijinternational1966.21.178

106. Danno A, Tanaka T (1984) Hot forming of stepped steel shafts by wedge rolling with three rolls. J Mech Work Technol 9:21–35. https://doi.org/10.1016/0378-3804(84)90091-3

107. Fu X, Dean T (1991) A study of defects in cross wedge rolling. Tech Rep 4

108. Wójcik L, Pater Z, Bulzak T, Tomczak J (2020) Physical modeling of cross wedge rolling limitations. Materials (Basel) 13:. https://doi.org/10.3390/ma13040867

109. Wójcik Ł, Pater Z (2018) Comparison analysis of cockroft - Latham criterion values of commercial plasticine and C45 steel. Acta Mech Autom 12:286–293. https://doi.org/10.2478/ama-2018-0044

110. Saito Y, Higashino T, Kato K (1977) Strain analysis in plane-strain rotary compression of cylindrical billet. J JSTP 18:120–127

111. K.H. Na, N.S. Cho (1989) Analysis of plane-strain rotational compression using the upper-bound method. J Mech Work Technol 19:211–222

112. Cho NS, Na KH, Kim JH (1990) Analysis of the rotational compression of a cylindrical billet in the transverse rolling process. J Mater Process Tech. https://doi.org/10.1016/0924-0136(90)90041-R

113. Pater Z (1996) Analysis of plane-strain rotational compression of rod by FEM. J Mater Process Technol. https://doi.org/10.1016/0924-0136(96)02385-0

114. Pater Z, Walczuk P, Lis K, Wójcik Ł (2018) Preliminary Analysis of a Rotary Compression Test. Adv Sci Technol Res J 12:77–82. https://doi.org/10.12913/22998624/86812

115. Pater Z, Tomczak J, Bulzak T, et al (2020) Rotary compression in tool cavity—a new ductile fracture calibration test. Int J Adv Manuf Technol. https://doi.org/10.1007/s00170-020-04943-5

116. Pater Z, Tomczak J, Bulzak T, et al (2020) Assessment of ductile

fracture criteria with respect to their application in the modeling of cross wedge rolling. J Mater Process Technol 278:. https://doi.org/10.1016/j.jmatprotec.2019.116501

117. QForm VX8.2 Manual

118. Newclay products. In: Newclay Prod. http://www.newclay.co.uk/

119. Hasbro playdoh. In: Hasbro. https://playdoh.hasbro.com/en-gb

120. Flair plasticine. In: Flair Leis. Prod. PLC. https://www.flairgp.co.uk/plasticine

121. Techniques C (2018) Standard Test Methods for Elevated Temperature Tension Tests of Metallic Materials 1. 1–8. https://doi.org/10.1520/E0021-17.2

122. Khlystov N, Lizardo D, Matsushita K, Zheng J (2013) Uniaxial Tension and Compression Testing of Materials

123. Wang M, Li X, Du F, Zheng Y (2004) Hot deformation of austenite and prediction of microstructure evolution of cross-wedge rolling. Mater Sci Eng A 379:133–140. https://doi.org/10.1016/j.msea.2004.01.055

124. Dong Y, Tagavi KA, Lovell MR, Deng Z (2000) Analysis of stress in cross wedge rolling with application to failure. Int J Mech Sci 42:1233–1253. https://doi.org/10.1016/S0020-7403(99)00035-1

125. (2017) Theoretical basis of QForm

126. Rasband WS (2011) ImageJ, U.S. National Institutes of Health, Bethesda, Maryland, USA. http://imagej.nih.gov/ij/

127. Beausir B, Fundenberger JJ (2017) Analysis Tools for Electron and X-Ray Diffraction. ATEX software, Metz

128. Yu MH (2002) Advances in strength theories for materials under complex stress state in the 20th century. Appl Mech Rev 55:169–218. https://doi.org/10.1115/1.1472455

129. Li Z, Shi J, Tang A (2014) Investigation on fracture mechanisms of metals under various stress states. Acta Mech 225:1867–1881. https://doi.org/10.1007/s00707-013-1024-x

130. Yamane K, Shimoda K, Kuroda K (2019) New Ductile Fracture Criterion for Prediction of Internal Fracture in Skew Rolling. In: XV International Conference on Computational Plasticity. Fundamentals and Applications

131. Anderson TL (2012) Fracture Mechanics: Fundamentals and Applications

132. Mott PH, Roland CM (2009) Limits to Poisson's ratio in isotropic materials. Phys Rev B - Condens Matter Mater Phys. https://doi.org/10.1103/PhysRevB.80.132104

133. Buchely MF, Maranon A, Silberschmidt V V. (2016) Material model for modeling clay at high strain rates. Int J Impact Eng 90:1–11. https://doi.org/10.1016/j.ijimpeng.2015.11.005

134. Ren XJ, Smith CW, Evans KE, et al (2006) Experimental and numerical investigations of the deformation of soft materials under tangential loading. Int J Solids Struct. https://doi.org/10.1016/j.ijsolstr.2005.07.013

135. Wong SF, Hodgson PD, Chong CJ, Thomson PF (1996) Physical modelling with application to metal working, especially to hot rolling. J Mater Process Technol 62:260–274. https://doi.org/10.1016/0924-0136(95)02219-8

136. Bai Y, Wierzbicki T (2008) A new model of metal plasticity and fracture with pressure and Lode dependence. Int J Plast 24:1071–1096. https://doi.org/10.1016/j.ijplas.2007.09.004

137. Tao X (2011) Research of Damage and Fracture for Cross Wedge Rolling Based on Damage Mechanics. China Academy of Machinery Science and Technology Group Co., Ltd.

138. (2014) GB/T 5216-2014 Structual steels with specific hardenability bands. Standardization Administration of China

139. Pickering FB (1978) Physical Metallurgy and the Design of Steels: Austenitic Stainless Steels. Applied Science Publishers, Michigan

140. Holappa LEK, Helle AS (1995) Inclusion Control in High-Performance Steels. J Mater Process Tech. https://doi.org/10.1016/0924-0136(95)01974-J

141. Bhadeshia H, Honeycombe R (2017) Steels: Microstructure and Properties 4th Edition. Elsevier, Amsterdam

142. Mintz B, Yue S, Jonas JJ (1991) Hot ductility of steels and its relationship to the problem of transverse cracking during continuous casting. Int Mater Rev 36:187–220. https://doi.org/10.1179/imr.1991.36.1.187

143. Crowther DN, Mintz B (1986) Influence of grain size and precipitation on hot ductility of microalloyed steels. Mater Sci Technol 2:1099–1105. https://doi.org/10.1179/mst.1986.2.11.1099

144. Hu J, Zhang JM, Sun GS, et al (2019) High strength and ductility combination in nano-/ultrafine-grained medium-Mn steel by tuning the stability of reverted austenite involving intercritical annealing. J Mater Sci 54:6565–6578. https://doi.org/10.1007/s10853-018-03291-w

145. Li J, Cao Y, Gao B, et al (2018) Superior strength and ductility of 316L stainless steel with heterogeneous lamella structure. J Mater Sci 53:10442–10456. https://doi.org/10.1007/s10853-018-2322-4

146. Tervo H, Kaijalainen A, Pikkarainen T, et al (2017) Effect of impurity level and inclusions on the ductility and toughness of an ultra-high-strength steel. Mater Sci Eng A 697:184–193. https://doi.org/10.1016/j.msea.2017.05.013

147. Luiz A (2018) Non-metallic inclusions in steels – origin and control. J Mater Res Technol 7:283–299

148. Zhang L, Thomas BG (2003) Inclusions in continuous casting of steel. XXIV Natl Steelmak Symp 138–183

149. Raghupathy VP, Srinivasan V, Krishnan H, Chandrasekharaiah MN (1982) The effect of sulphide inclusions on fracture toughness and fatigue crack growth in 12 wt% Cr steels. J Mater Sci 17:2112–2126. https://doi.org/10.1007/BF00540430

150. Salas-Reyes AE, Mejía I, Bedolla-Jacuinde A, et al (2014) Hot ductility behavior of high-Mn austenitic Fe-22Mn-1.5Al-1.5Si-0.45C TWIP steels microalloyed with Ti and V. Mater Sci Eng A 611:77–89. https://doi.org/10.1016/j.msea.2014.05.072

151. Mejía I, Bedolla-Jacuinde A, Maldonado C, Cabrera JM (2011) Hot ductility behavior of a low carbon advanced high strength steel (AHSS)

microalloyed with boron. Mater Sci Eng A 528:4468–4474. https://doi.org/10.1016/j.msea.2011.02.040

152. Zheng C, Raabe D (2013) Interaction between recrystallization and phase transformation during intercritical annealing in a cold-rolled dual-phase steel: A cellular automaton model. Acta Mater. https://doi.org/10.1016/j.actamat.2013.05.040

153. Park JH, Kang Y (2017) Inclusions in Stainless Steels − A Review. Steel Res Int 88:1–26. https://doi.org/10.1002/srin.201700130

154. Suzuki HG, Nishimura S, Yamaguchi S (1982) Characteristics of Hot Ductility in Steels Subjected To the Melting and Solidification. Trans Iron Steel Inst Japan 22:48–56. https://doi.org/10.2355/isijinternational1966.22.48

155. Zhang X, Yang S, Li J, Wu J (2019) Transformation of oxide inclusions in stainless steel containing yttrium during isothermal heating at 1473 K. Metals (Basel) 9:. https://doi.org/10.3390/met9090961

156. Shibata H, Tanaka T, Kimura K, Kitamura SY (2010) Composition change in oxide inclusions of stainless steel by heat treatment. Ironmak Steelmak 37:522–528. https://doi.org/10.1179/030192310X12700328925903

157. Chu Y, Li W, Ren Y, Zhang L (2019) Transformation of Inclusions in Linepipe Steels During Heat Treatment. Metall Mater Trans B Process Metall Mater Process Sci 50:2047–2062. https://doi.org/10.1007/s11663-019-01593-1

Appendix A

Code for QForm subroutines

Damage model subroutine

```
set_target_workpiece()

Damage_1 = result("Damage_1", 0) –C&L damage

Damage_2 = result("Damage_2", 0) –R&T damage

Damage_3 = result("Damage_3", 0) –Oyane damage

Damage_4 = result("Damage_4", 0) –Proposed damage

Strain_increment = result("Strain_increment")

Triaxiality = result("Triaxiality")

function UserFields(stress_mean, stress_flow, stress_1,stress_3, strain,
prev_strain, prev_Damage_1, prev_Damage_2, prev_Damage_3,
prev_Damage_4)


Strain_Inc = strain - prev_strain -- plastic effective strain increment

if stress_1>0 then

    Damage_1_Local = (stress_1*Strain_Inc)*1e-6 + prev_Damage_1

    else Damage_1_Local = prev_Damage_1

end

if stress_flow>0 then

      Tri = stress_mean/stress_flow;

Damage_2_Local = math.exp(1.5*stress_mean/stress_flow)*Strain_Inc +
prev_Damage_2

Damage_3_Local = (1+0.5*stress_mean/stress_flow)*Strain_Inc +
prev_Damage_3

else Damage_2_Local = prev_Damage_2

      Damage_3_Local = prev_Damage_3

end

Damage_4_Local = (0.72*stress_1-0.5*stress_3)*1e-6
```

163

```
store(Damage_1, Damage_1_Local)
store(Damage_2, Damage_2_Local)
store(Damage_3, Damage_3_Local)
store(Damage_4, Damage_4_Local)
store(Strain_increment, Strain_Inc)
store(Triaxiality, Tri)
end
```

Code for Abaqus subroutines vusdfld

```
      subroutine vusdfld(
c Read only -
     *   nblock, nstatev, nfieldv, nprops, ndir, nshr,
     *   jElem, kIntPt, kLayer, kSecPt,
     *   stepTime, totalTime, dt, cmname,
     *   coordMp, direct, T, charLength, props,
     *   stateOld,
c Write only -
     *   stateNew, field )
c
      include 'vaba_param.inc'
c
      dimension jElem(nblock), coordMp(nblock,*),
     *       direct(nblock,3,3), T(nblock,3,3),
     *       charLength(nblock), props(nprops),
     *       stateOld(nblock,nstatev),
     *       stateNew(nblock,nstatev),
     *       field(nblock,nfieldv)
      character*80 cmname
c
```

```
c    Local arrays from vgetvrm are dimensioned to
c     maximum block size (maxblk)
c
      parameter( nrData=6 )
      character*3 cData(maxblk*nrData)
      dimension peeq(maxblk), stress(maxblk*nrData)
      dimension jData(maxblk*nrData)
c
      jStatus = 1
      call vgetvrm( 'S', stress, jData, cData, jStatus )
c
      jStatus = 1
      call vgetvrm( 'PEEQ', peeq, jData, cData, jStatus )
c
      if( jStatus .ne. 0 ) then
         call xplb_abqerr(-2,'Utility routine VGETVRM '//
     *      'failed to get variable.',0,zero,' ')
         call xplb_exit
      end if
c
      call setField( nblock, nstatev, nfieldv, nrData,
     *   stepTime, totalTime, dt,
     *   peeq, stress, stateOld, stateNew, field)
c
      return
      end
      subroutine setField( nblock, nstatev, nfieldv, nrData,
     *   stepTime, totalTime, dt,
     *   peeq, stress, stateOld, stateNew, field )
c
      include 'vaba_param.inc'
```

```
c
      dimension stateOld(nblock,nstatev),
     *   stateNew(nblock,nstatev),
     *   field(nblock,nfieldv),
     *   peeq(nblock), stress(nblock,nrData)
c
      do k = 1, nblock
c
         DamageOld = stateOld(k, 1)
         PeeqOld = stateOld(k, 2)
         ESOld = stateOld(k, 3)
         TriOld = stateOld(k, 4)
         Damage = DamageOld
c
         S11 = stress(k, 1)
         S22 = stress(k, 2)
         S33 = stress(k, 3)
         S12 = stress(k, 4)
         S23 = stress(k, 5)
         S31 = stress(k, 6)
         Smean = (S11+S22+S33)/3
         ES = sqrt((((S22-S11)**2+(S33-S22)**2+(S11-S33)**2)/2
     *        + 3 * (S12**2 + S23**2 + S31**2))
         if ( ES .gt. 1.0e-6) then
            Tri = Smean/ES
         else Tri = 10000
         end if
c
         dpeeq = peeq(k) - stateOld(k, 2)
         if ( Tri .lt. 3.0) then
            Damage = DamageOld + exp(1.5 * Tri) * dpeeq
```

```
      else Damage = DamageOld
      end if
c
      stateNew(k,1) = Damage
      stateNew(k,2) = peeq(k)
      stateNew(k,3) = ES
      stateNew(k,4) = Tri
      field(k,1) = stateNew(k,1)
      field(k,2) = stateNew(k,2)
      field(k,3) = stateNew(k,3)
      field(k,4) = stateNew(k,4)
c
    end do
c
    return
    end
```

Appendix B

Three methods to calculate the material constants in the proposed fracture criterion (in Equation 6.2)

To apply the proposed fracture criterion, it is important to get the associated material constants *A*, *B*, *C* and *Dc*. Therefore, three methods are introduced in this study.

Method 1: Conducting interrupted tests with simplified CWR dies as introduced in section 5.3.

It involves (i) conducting the interruptive tests with the simplified CWR dies under two feed angles and determining the void nucleation moments; (ii) conducting the corresponding FE model and achieving the stress/strain states at the void nucleation moments; and (iii) solving the material constants by inputting the achieved stress/strain states/history to the corresponding fracture criterion.

This method is advantageous in two aspects: (1) it gives highly accurate results as it simulates the CWR states, which enables the formation of central cracking; and (2) the process can be completed with only one pair of flats, which significantly benefits the industry by saving time and cost.

Method 2: Conducting simple uniaxial tensile and pure shear tests

It involves (i) conducting the uniaxial tensile and pure shear tests with the mechanical test machine such as Instron and calculating the fracture stress/strain; (ii) running the corresponding FE model and achieving the accurate stress/strain states until the sample fractures; and (iii) solving the material constants by inputting the achieved stress/strain states/history the corresponding fracture criterion.

This method can be completed in the lab environment without using CWR machine. However, as only the uniaxial and the pure shear stress states are simulated, the accuracy of the material values is not as high as that in Method 1.

Method 3: Industrial experimental data fitting
This method is recommended if sufficient experimental data under different die geometries are available.

It involves: (i) recording the cracking conditions of the CWRed samples under different die geometries; (ii) running the FE models and extracting the stress/strain states at the end of the CWR in each condition; and (iii) solving the material constant by data fitting under the condition that the damage value in all the cracked cases is higher than the damage value in all the non-cracked cases. The results' accuracy can be improved by adding the experimental data under different die geometries.

This method is only recommended if a high amount of available CWR data under different die geometries are available. If not, the other two methods are recommended as it requires a high number of different CWR dies. However, this method is advantageous as it is built based on the existing experimental data, and no extra experimental data is required. In addition, these data are yielded in the CWR practices, so the accuracy of the calculated material constants are relatively accurate if the experimental data is rich enough.